

A shock compression investigation of failure waves and phase transition in soda-lime glass

Thesis by
Akshay Joshi

In Partial Fulfillment of the Requirements for the
Degree of
Doctor of Philosophy

The logo for the California Institute of Technology (Caltech), featuring the word "Caltech" in a bold, orange, sans-serif font.

CALIFORNIA INSTITUTE OF TECHNOLOGY
Pasadena, California

2021
Defended May 12, 2021

© 2021

Akshay Joshi

ORCID: 0000-0001-8347-8357

All rights reserved

ACKNOWLEDGEMENTS

I would like to express my sincere gratitude to my Ph.D. advisor, prof. Guruswami Ravichandran (Ravi). His insights, guidance, encouragement, patience and support made my graduate school experience a very rewarding one. He patiently allowed me to explore new ideas and approaches, offering his valuable guidance and inputs where needed. I am very grateful to him for all that he has taught me. I would also like to thank my committee members: profs. Meiron, Mello and Kaushik, for taking their valuable time to evaluate, and help improve, my thesis.

I also owe a special thanks to Dr. Suraj Ravindran and my friend Vatsa Gandhi, for all their kind help and valuable guidance. They are brilliant experimentalists, great friends, and very inspiring individuals with a strong zeal for research. I consider myself fortunate to have worked with them over the course of my Ph.D. I would also like to thank my friends and colleagues - Jack Weeks and Andrew Akerson for helping me prepare for my thesis defense. I also express my sincere gratitude to all my other friends and colleagues from Ravi's lab and Caltech. Without them, my Caltech experience would not have been the same. I am also grateful to the staff at GALCIT including Christine Ramirez, Peggy Blue, Lydia Suarez and Donna Mojahedi for all their help. I am also greatly indebted to Ali Kiani from the GALCIT machine shop, for keeping up with our routinely overwhelming orders for machining parts.

I am very grateful to my dear family, friends and teachers from India, for all their support and affection. Their efforts and sacrifice have played a foundational role for all my achievements in life. I also remain eternally indebted to my spiritual teachers - His Holiness Radhanath Swami and Srila Prabhupada for their teachings of Krishna Consciousness, which made me a better person, and has helped me cope with many inevitable adversities in life.

I am truly grateful for all that I have received and seek to use my skills and energy in service, and betterment of the world.

ABSTRACT

Soda-lime glass (SLG) and other silica glasses find use in many technological applications involving high pressures and strain rates, such as systems with laser-matter interactions, transparent armor, etc. An experimentally validated constitutive model for these glasses is required for modeling their mechanical behavior at high pressures and strain rates. Also, due to the abundance of silica in the earth's crust, understanding the behavior of these glasses at high pressures can provide significant insights into many geophysical processes. To this end, shock compression experiments are carried out on SLG to study the material's behavior under impact stresses of 5-10 GPa. These experiments are accompanied by numerical simulations and constitutive modeling of SLG to gain further insights into the reported failure-wave phenomenon and phase transitions associated with the material.

The significant findings of this study in relation to the failure-wave phenomenon were the sudden densification/compaction of SLG associated with the failure-wave and the disappearance of the failure-wave phenomenon for impact stresses above 10 GPa. When viewed in the context of the findings from past experiments, these results seem to suggest that localized densification/compaction of SLG causes nucleation of cracks and subsequent comminution in the material under shock compression. These results and observations offer a potential explanation of the mechanism underlying the failure-wave phenomenon.

Further, the shock compression and release experiments performed in this work provided significant insights into the onset of possible phase-transition in SLG under shock compression. A loading-unloading hysteresis is observed in the material's stress-strain curve for impact stresses higher than 5.8 GPa, with the permanent/residual strain increasing with impact stress. Further analysis of these results strongly indicates that the hysteresis is more likely due to a gradual, irreversible phase transition of SLG than due to regular inelastic behavior. Thus, the results suggest that the SLG undergoes a gradual phase transition to a stiffer phase, although other properties of this phase remain unclear. It can also be noted that this phase transition is postulated to start occurring under shock compression of SLG to stresses above 5 GPa, which is also the threshold stress for the onset of the failure-wave phenomenon. It is, therefore, possible that the two phenomena are interrelated. The experimental results from this study are further used to construct a constitutive model to capture the unloading behavior of SLG.

PUBLISHED CONTENT AND CONTRIBUTIONS

¹A. Joshi, S. Ravindran, V. Gandhi, and G. Ravichandran, “Shock compression and release study to probe phase transition in soda lime glass,” *To be submitted* (2021),

A.J. participated in originating the project, performing the experiments, analyzing the data, and writing the manuscript.

²A. Joshi, S. Ravindran, V. Gandhi, and G. Ravichandran, “Probing the properties and mechanisms of failure waves in soda-lime glass,” *Journal of Applied Physics* **129**, 185902 (2021), <https://doi.org/10.1063/5.0047950>,

A.J. participated in originating the project, performing the experiments, analyzing the data, and writing the manuscript.

TABLE OF CONTENTS

| | |
|---|------|
| Acknowledgements | iii |
| Abstract | iv |
| Published Content and Contributions | v |
| Table of Contents | v |
| List of Illustrations | vii |
| List of Tables | xiii |
| Chapter I: INTRODUCTION | 1 |
| 1.1 Motivation and Organization of Thesis | 1 |
| 1.2 Background | 2 |
| Chapter II: PROBING THE PROPERTIES AND MECHANISMS OF FAIL- URE WAVES IN SODA-LIME GLASS | 8 |
| 2.1 Introduction | 8 |
| 2.2 Materials and methods | 13 |
| 2.3 Results and discussion | 21 |
| 2.4 Conclusions | 36 |
| Chapter III: SHOCK COMPRESSION AND RELEASE STUDY TO PROBE PHASE TRANSITION IN SODA-LIME GLASS | 44 |
| 3.1 Introduction | 44 |
| 3.2 Materials and methods | 46 |
| 3.3 Results and discussion | 47 |
| 3.4 Modeling | 59 |
| 3.5 Conclusion | 65 |
| Chapter IV: PRESSURE-SHEAR PLATE IMPACT EXPERIMENTS ON SODA-LIME GLASS | 69 |
| 4.1 Background | 69 |
| 4.2 Experiments to determine the shear-strength of SLG at various pres- sures. | 70 |
| 4.3 Alumina AD995 as an anvil for PSPI experiments | 75 |
| Chapter V: SUMMARY AND FUTURE WORK | 79 |
| 5.1 Summary | 79 |
| 5.2 Sandwiched PSPI experiments on SLG at 4-6 GPa normal stresses | 79 |
| 5.3 Normal plate impact experiments on SLG and other silica glasses | 80 |
| 5.4 Imaging the SLG under impact at 3 GPa and 6 GPa | 80 |
| 5.5 Determining shear modulus of SLG as a function of impact stress using oblique impact experiments | 81 |
| Appendix A: EQUATION OF STATE FOR SODA-LIME GLASS | 84 |
| Appendix B: WINDOW CORRECTIONS: OPTICAL AND IMPEDANCE MISMATCH | 89 |

LIST OF ILLUSTRATIONS

| <i>Number</i> | <i>Page</i> |
|--|-------------|
| 1.1 Schematic of a 1-D shock. U_S denotes Lagrangian shock wave-speed and u_S denotes the same in Eulerian frame. All compressive stresses and strains are considered positive. | 3 |
| 1.2 Schematic stress-strain curve of material subject to shock compression and release/unloading. | 4 |
| 1.3 Schematic of a Lagrangian wave-velocity vs. particle velocity plot typically observed in metals. | 5 |
| 2.1 Schematics of normal impact experiments on SLG and the velocity measurement using Photonic Doppler Velocimetry (PDV). The Down-Barrel Probe (DBP) measures the velocity of the WC impactor. The cavity in the projectile behind the WC flyer plate ensures release to zero stress at the WC rear surface. (a) Regular configuration used for most experiments. (b) Layered glass impact configuration used for experiment #AJ-3. | 14 |
| 2.2 Schematic stress-particle velocities (a) for experiments with impact stress less than 7.5 GPa. SLG can be assumed to be elastic at these stresses [35], making the loading and release paths identical. (b) for experiments with impact stresses higher than 7.5 GPa, which exceeds the Hugoniot elastic limit of WC. | 15 |
| 2.3 Summary of the free rear surface velocity recordings for all experiments. The horizontal axis representing time is scaled by sample thickness to match wave-arrival timings for all experiments. | 16 |
| 2.4 Schematic of the simulation domain used in the modeling of experiments on soda-lime glass. | 17 |
| 2.5 Pressure and stress vs. volumetric strain Equations of State (EOS) used to model behavior of SLG. (a) EOS-1 was used to model SLG for impact stresses higher than 7 GPa. (b) EOS-2 was used for SLG at impact stresses below 7 GPa, which incorporates densification in order to capture the slower second compression wave. The details of the construction of the two equations of state are presented in Appendix A. | 20 |

| | | |
|------|--|----|
| 2.6 | Free surface velocity vs. time alongside a schematic X-t characteristic diagram for experiment #AJ-1. The spall plane was designed to be behind the failure front. Impact occurs at $t=0$ | 22 |
| 2.7 | Schematic X-t characteristic diagram and free surface velocity vs. time plots for experiment #AJ-2. The apparent velocity of the impact surface obtained using the DBP is also shown. The tensile wave is formed ahead of the failure front. | 26 |
| 2.8 | Schematic showing the interaction of tensile wave from the rear free surface with failure wave in experiment #AJ-2 (Fig. 2.7). The tensile wave is expected to further aid in propagating the axial cracks | 27 |
| 2.9 | Free surface velocity vs. time plots and a schematic of the X-t characteristic diagram for experiment #AJ-3. The material-speed of the failure wave observed in the second glass layer is 0.477 km/s, as compared to 1.3 km/s observed in the first glass layer | 28 |
| 2.10 | Free surface velocity vs. time plots and a schematic of the X-t characteristic diagram for experiment #AJ-4. Owing to high rise time of shocks in SLG and the use of a thin WC impactor, the stress-wave is attenuated as it propagates through the SLG. Simulations predict two additional tensile unloading which are not observed in the experiment. | 31 |
| 2.11 | Free surface velocity vs. time and a schematic X-t characteristic diagram for the experiment #AJ-5. The formation of tensile wave is ahead of the failure wave. The reverberations indicate that the failure wave continues to propagate at 1.3 km/s after interacting with the tensile wave. | 32 |
| 2.12 | Free surface velocity vs. time and a schematic X-t characteristic diagram for the experiment #AJ-6. The high speed of initial-release waves [35] were accounted for in the X-t diagram. The speed of the tensile waves was inferred from the velocity profile. Failure waves are absent in this experiment and no failed section was used in the simulation. | 34 |
| 2.13 | Stress vs. volumetric strain for SLG from the current work plotted alongside previous works by Dandekar et al. [13, 52, 53], Alexander et Al. [47] and Grady et al. [48]. The data for the works of the other authors is adapted from the compilation provided by Gorfain et al. [28]. | 36 |

| | | |
|------|--|----|
| 2.14 | Schematics of two possible mechanisms to explain the cause of the failure wave phenomenon. (a) The microcrack hypothesis suggests that the failure wave is due to microcracks propagating into the SLG from the impact surface. (b) The densification hypothesis suggests that a slower phase transition-like densification causes cracking and comminution of the SLG material behind it. | 37 |
| 3.1 | Schematic of plate impact experiment used to observe the shock compression and release behavior of SLG using Photon Doppler Velocimetry (PDV). The Down-Barrel Probe (DBP) measures the velocity of the impactor. The presence of the LiF[100] window ensures that the SLG material remains under compression as the PDV probe records the SLG-LiF interface velocity. A 0.5 μm thick aluminum (Al) coating provides a reflective surface for PDV measurement. The cavity behind the impactor ensures that the stress releases to zero at the rear-surface of the impactor. | 47 |
| 3.2 | Schematic of procedure to evaluate the wave speed in material frame, $C_h(u)$. 48 | |
| 3.3 | Velocimetry data from experiment WSL-1 for SLG-LiF interface and LiF free surface. A failure wave velocity of 1.3 km/s was assumed in the (X-t) diagram. | 50 |
| 3.4 | Stress-strain curve for SLG material in experiment WSL-1. The dashed lines indicate the bounds in uncertainty of stress-strain curve due to uncertainty in trigger timing. The pressure curve is inferred from the stress curve by subtracting the elastic deviatoric stress. . . . | 51 |
| 3.5 | Velocimetry data of experiment #SSL-2 for SLG-LiF interface and LiF free surface. A failure wave velocity of 1.3 km/s was assumed in the (X-t) diagram. | 52 |
| 3.6 | Stress-strain curve for SLG material inferred from experiment #SSL-2 (a) not accounting for additional compression due to the failure wave. (b) accounting for additional compression due to the failure wave. The dashed-lines indicate the bounds in uncertainty of stress-strain curve due to uncertainty in trigger timing (40 ns). The pressure curve is inferred from the stress curve by subtracting the elastic deviatoric stress. | 53 |

- 3.7 Schematic stress-strain diagrams of shock-loading and release for materials with (a) Regular inelastic response and (b) Phase transition. For material with phase transition the mismatch in pressure loading and unloading paths can be observed. Additionally, materials with phase transition can be expected to undergo higher permanent strains for higher impact stresses. Both materials considered here are assumed to lack strain-hardening. 54
- 3.8 Plot of Lagrangian wave speeds of compression and release waves in SLG. The data for experiments AT-3 and AT-4 are taken from [16]. The compression and release wave speeds for SLG provided as a function of peak particle velocity in [2] was modified by converting particle velocity to strains (Eq. A.2 in Appendix A). The onset of hysteresis is the strain at which the release and compression wave-speeds start to differ significantly. 56
- 3.9 Estimates of shear modulus (a) Plot of computed shear modulus vs. volumetric strain for SLG as computed using Eq. 3.9. (b) Plot of shear modulus vs. pressure for SLG, by converting strains in previous plot to corresponding pressure in SLG (using EOS-1 described in Chapter 2). Data for SLG is plotted alongside data for fused quartz from [23] and MD simulations results from [24]. 58
- 3.10 Stress-strain response of SLG and other polymorphs of SiO₂. (a) Stress-strain plots of symmetric shock-release experiments on SLG. (b) Alongside data in (a), stress or pressure vs. strain curves for high pressure polymorphs of SiO₂: Pressure vs. strain isotherm for α -quartz, pressure vs. strain isotherm for coesite, Stress vs. strain Hugoniot for stishovite. SLG- LiF interface data for experiments AT-3 and AT-4 were taken from [16] and then processed to obtain the shown stress-strain plots for these experiments. EOS-1 is the equation of state for SLG used in chapter 2. Equations of state for α -quartz, coesite, and stishovite were taken from [26], [9] and [27], respectively. 60

| | | |
|------|--|----|
| 3.11 | Plots of experimentally observed evolution of release wave-speeds under release compared with approximate linear estimates of the same used in modelling. (a) Plot of Lagrangian release wave speed evolution with strain observed in experiments. The initial release wave speed plot is the same as in Fig. 3.8 and is taken from [2]. The data for release paths for experiments AT-3 and AT-4 are taken from [16]. (b) Plot of approximate estimations of the release path for different peak compressive strains. This is used to model the evolution of release wave speed with strain in SLG. The δ in the equation for the high-slope release path denotes a variable intercept depending on the peak/initial-release strain. | 63 |
| 3.12 | Comparison of experimentally measured interface velocity (optically corrected) and simulation results. Data for experiments AT-3 and AT-4 were taken from [16], and were digitized using [34]. Results from two types of simulations are shown for each experiment. One set of simulations assume a regular elastic unloading, and the other set of simulations involve a release path prescribed using Eq. 3.11. | 64 |
| 4.1 | Schematic of pressure shear plate impact (PSPI) experiments. (a) Symmetric PSPI experiment, (b) Sandwiched PSPI experiment. | 70 |
| 4.2 | Time-material position ($t - X$) schematic of a sandwiched PSPI experiment. C_L and C_S denote the anvil material's longitudinal wave speed and shear wave speed, respectively, in Lagrangian coordinates. | 71 |
| 4.3 | A schematic of (a) longitudinal stress vs. particle velocity and (b) shear stress vs. particle velocity Hugoniot in sandwiched PSPI experiments. The dotted lines represent the sandwiched material's 'ring-up' response. The solid lines are the anvil materials stress Hugoniot, which for linearly elastic materials are straight lines in stress-particle velocity space. | 72 |
| 4.4 | Free surface normal and transverse velocities for experiments shown in Table 4.1. The curves in black are normal free-surface velocities and curves in red are the transverse free-surface velocities for the PSPI experiments. The abrupt drop in normal free-surface velocity after the first normal stress ring-up is highlighted. | 73 |
| 4.5 | Plot of normal free surface velocity vs. time for Expt. CK-1807 and simulations using EOS-1 and EOS-2 equations of state for SLG (discussed in Chapter 2). | 74 |

| | | |
|-----|---|----|
| 4.6 | Free surface velocities for symmetric PSPI of alumina AD 995 (Expt. AJ-2001). The free surface velocities are plotted alongside a X-t characteristic diagram. Stress states prevalent in relevant regions of the X-t diagram is shown. The pure shear state is postulated to have caused a failure in the Alumina material. | 76 |
| 5.1 | Schematic of a plate impact experiment involving imaging of failure waves in SLG. | 81 |
| 5.2 | Schematic of a suggested experimental configuration to measure shear modulus of SLG as a function of pressure. The PDV arrangement can alternatively be replaced by a camera to detect the arrival of shear waves at the SLG rear surface. | 82 |
| A.1 | Lagrangian wave speed vs. particle velocity diagram for soda-lime glass (SLG). Adapted from Alexander et al. [3] | 85 |
| A.2 | The stress-particle velocity (σ - u_p) Hugoniot diagram used to construct the densification region A-B using results from experiments #AJ-1, #AJ-2, and #AJ-3. | 87 |
| B.1 | Schematic of window-correction for shock-wave in window. | 89 |
| B.2 | Schematic of window-correction for release fan in window. | 91 |
| B.3 | t-X diagram for release fan. | 93 |
| B.4 | Comparison of z-cut quartz data from [4] and release fan correction (Eq. B.14) for 532 nm wavelength light. | 96 |
| B.5 | Observed particle velocity vs. actual particle velocity for shock-waves and release fan in LiF[100] for 1550 nm light. | 96 |
| B.6 | Stress-particle velocity of LiF and SLG used to obtain the in-material particle velocity in SLG. | 97 |
| B.7 | Impedance mismatch correction for optically corrected data from Expt. SSL-2 of this work. | 97 |

LIST OF TABLES

| <i>Number</i> | <i>Page</i> |
|--|-------------|
| 2.1 Summary of experimental conditions and results. ^a Failure wave speed in material frame. ^b Thickness of the first/second SLG disk in this experiment. ^c Speed of the failure wave in the first/second SLG disk in this experiment. ^d No failure wave was observed in this experiment. | 17 |
| 2.2 Properties of soda-lime glass used in the simulations. | 20 |
| 2.3 Material properties of tungsten carbide (WC) used in the simulations [42, 49]. | 21 |
| 3.1 Summary of experimental results | 47 |
| 3.2 Properties of LiF[100] used in the simulation. Equation of state properties were obtained from [31], where Grüneisen parameter (Γ_0) is assumed to be $(2S - 1)$ | 61 |
| 4.1 Summary of experiments with SLG wafers sandwiched between WC anvils. Experiments CK-1807 and CK-1808 are taken from [9]. Experiments AJ-1909 and AJ-2007 are normal impact experiments. | 71 |
| 4.2 Summary of symmetric PSPI experiment on alumina AD995. | 75 |

Chapter 1

INTRODUCTION

1.1 Motivation and Organization of Thesis

Knowledge of the properties of silica and its oxide is vital to understanding many geological processes. This is because silica, after oxygen, is the most abundant element in the earth's crust. Study of the behavior of SiO_2 and its high pressure polymorphs, which form a good representative of silicate crystals and melts of the deep Earth [1], can significantly aid modelling and understanding geological processes that often involve extremely high pressures and temperatures. Soda-lime glass (SLG) and other silicate glasses also play an important role in many engineering applications such as optical elements (windows, lenses, optic fibers), structural components, transparent armor and micro-electromechanical systems (MEMS). In many such engineering applications, glass experiences/interacts with high structural loads, high pressures and loading rates, high-intensity lasers, etc. Thus, it is essential to understand its behavior under high pressures for successfully incorporating it into computational models.

Shock compression experiments and associated diagnostics like velocity interferometry (VISAR, [2]) and Photon Doppler Velocimetry (PDV, [3]) provide a convenient method of studying the response of materials subject to extremely high pressures, temperatures and strain-rates. The pulse duration of the shock can be varied to a certain extent to match the time-scale of the phenomenon under study. Shock compression can be laser-driven or, as done in the current work, achieved by plate impact. Previous shock compression studies of SLG [4–9] observed that for stresses around 4–8 GPa, a peculiar ‘failure wave’ travelled behind the shock-wave at a speed of around 1.4–2.6 km/s [10]. Behind this failure wave, it was observed that the SLG material had half the original shear strength and zero tensile strength, thus indicating fracture/comminution of the SLG material. Although various theories and models have been proposed to explain this phenomenon [11–14], the mechanism and cause underlying it is still a topic of considerable debate. It is also postulated that the mechanism responsible for failure waves in glasses might also provide answers to the century old mystery in geophysics of ‘Deep-focus Earthquakes’ [15, 16]. As quoted in [16], “how fractures initiate, nucleate, and propagate at these depths

remains one of the greatest puzzles in earth science.”

This prevalence of fracture/cracking in glasses subject to high near-hydrostatic compression appears counter-intuitive. This is because high compressive stresses are known to impart high strength and crack-resistance to glasses, as seen in the example of Prince Rupert’s Drops (PRDs) [17]. However, the same PRDs are also seen to undergo complete comminution when the internal tensile regions are exposed by snapping the tail-end of the drop. Surprisingly, these comminution waves also travel at around 1.7 km/s (similar to the failure wave) through the PRD [18]. Similar to what is observed in PRD, internal residual strains in SLG also seem to play a role in the failure wave phenomenon [19]. However, other properties of failure waves such as the threshold stresses for their existence and their nucleation remain largely unaddressed.

A more comprehensive background of the failure wave phenomenon along with experiments and modeling undertaken as a part of this work are discussed in Chapter 2. Chapter 3 discusses the experiments undertaken to probe the shock loading and unloading behavior of SLG, and the insights derived from those experiments regarding phase-transition in SLG to a high-density phase. Chapter 4 provides an overview of pressure-shear plate impact experiments on SLG, performed as a part of this work and previous works. Chapter 5 provides a summary of the important findings of this work and suggests future works to capture the properties of SLG and other silica glasses. Appendix A provides details of calculating the equation of state of SLG used in the current work, and Appendix B discusses the window correction factors used to process the data provided in Chapter 3.

1.2 Background

Normal Shock relations

Longitudinal one dimensional shocks accelerate particles only along the direction of its propagation. This implies that the strain caused by the shock is only along its direction of propagation. This uniaxial strain condition is accompanied by lateral confinement of the bulk material. The resultant hydrostatic stresses in the shocked material can be used to probe the compressibility of materials at high pressures. Figure 1.1 depicts the state variables $\sigma, \epsilon, \rho, u_p, E$ on either side of the shock propagating at a Lagrangian speed of U_S . The ‘jump-conditions’ relating the state variables ahead of the shock (-) to the state variables behind the shock (+) are derived by applying the conservation laws for mass, momentum, and energy for a control

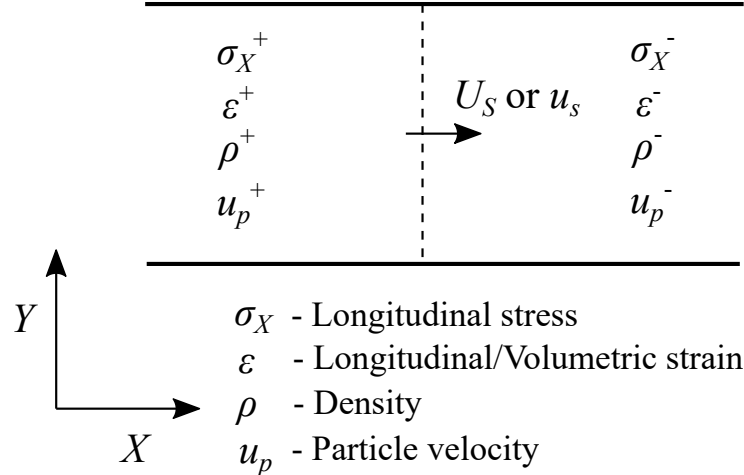


Figure 1.1: Schematic of a 1-D shock. U_S denotes Lagrangian shock wave-speed and u_s denotes the same in Eulerian frame. All compressive stresses and strains are considered positive.

volume enclosing the shock [20]. The resulting Rankine-Hugoniot jump conditions are:

$$\begin{aligned} \rho_0 U_S \left(\frac{1}{\rho^-} - \frac{1}{\rho^+} \right) &= (u_p^+ - u_p^-) \\ \rho_0 U_S (u_p^+ - u_p^-) &= (\sigma_X^+ - \sigma_X^-) \\ \rho_0 U_S \left(\left(E + \frac{1}{2} u_p^2 \right)^+ - \left(E + \frac{1}{2} u_p^2 \right)^- \right) &= ((\sigma_X u_p)^+ - (\sigma_X u_p)^-) \end{aligned}$$

where, ρ_0 is the reference/ambient density of the material.

The transverse stress (σ_Y) is then determined using elasticity relations for $\sigma_X < \sigma_{HEL}$, and using relevant plasticity flow rules for $\sigma_X > \sigma_{HEL}$. Here, σ_{HEL} is the Hugoniot Elastic Limit (HEL) or initial yield point of the material (see Fig. 1.2). The pressure (p) experienced by the material is then given by : $p = \frac{\sigma_X + 2\sigma_Y}{3}$.

Further, the constitutive relation for the material is usually specified in terms of a linear relationship between U_S and u_p :

$$U_S = C_0 + S (u_p - u_{pHEL})$$

where C_0 and S are material parameters that are determined by experiments. Usually C_0 corresponds to the bulk sound speed $\left(\sqrt{\frac{K}{\rho_0}} \right)$ of the material. u_{pHEL} is the particle velocity corresponding to the material's HEL, for a shock traversing into a quiescent material. K is the bulk modulus of the material.

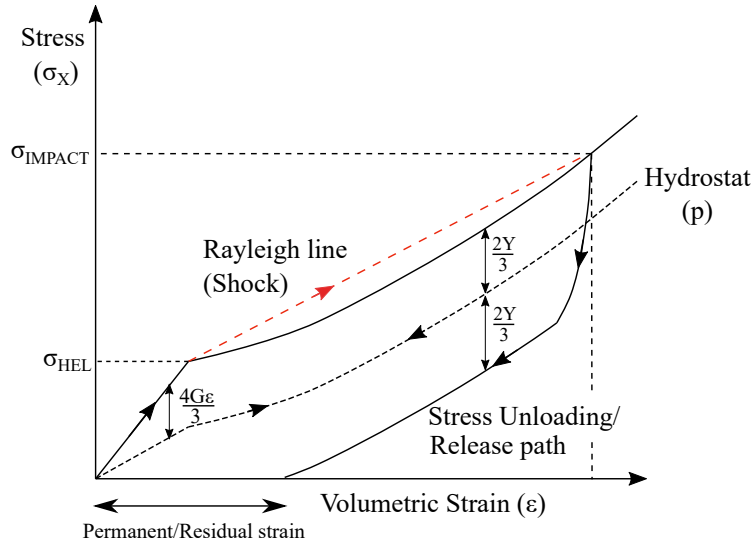


Figure 1.2: Schematic stress-strain curve of material subject to shock compression and release/unloading.

It is more common to use the Lagrangian shock speed (U_S) in constitutive laws to describe materials as opposed to the Eulerian shock speed (u_S). This is because the former is a material property while the latter depends on the speed of movement of the body experiencing the shock-wave. The conversion from U_S to u_S is given as:

$$u_s = \frac{\rho_0}{\rho^-} U_S + u_p^- .$$

Shock and release experiments

Certain shock compression studies involve subjecting the material specimen to sequential shock-loading steps or unloading (usually more gradual). Such experiments provide insight into the material's Grüneisen parameter [21] and its yield strength. Material strength is also determined using the compression and release technique, referred to as the self-consistent method [22–25]. The principle underlying the shock and release technique is depicted by a typical metal's stress-strain curve shown in Fig. 1.2.

A material's stress-strain history of the material depicted in Fig. 1.2 is determined using data acquired using velocimetry techniques, such as VISAR or PDV, or embedded stress and strain gauges. The material's yield strength (Y) at the impact stress is inferred from the difference between the loading and unloading curves, as shown in the figure.

The transition from elastic unloading to a plastic unloading (reverse-yielding) can also be observed in a plot of Lagrangian wave-speeds as a function of particle velocity

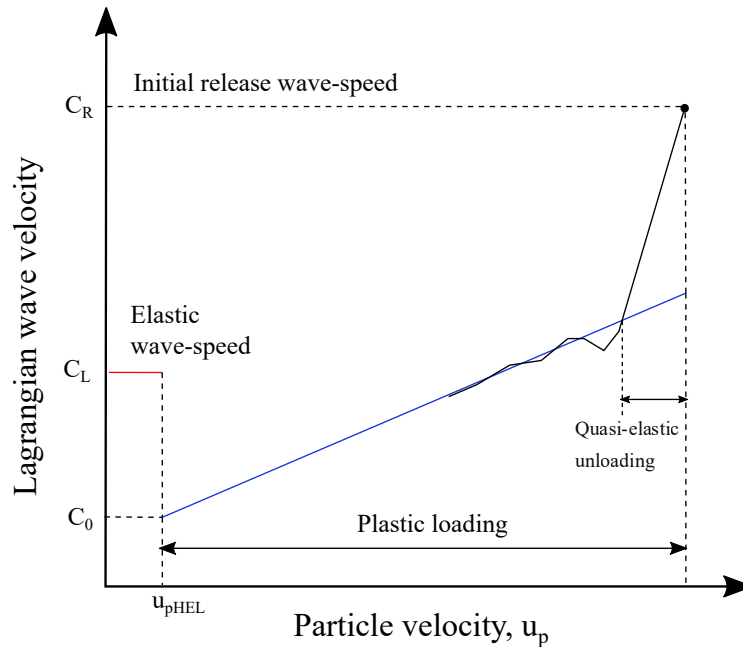


Figure 1.3: Schematic of a Lagrangian wave-velocity vs. particle velocity plot typically observed in metals.

[23–25]. A schematic plot of these wave-speeds corresponding to the stress-strain curve shown in Fig. 1.2 is shown in Fig. 1.3. The Lagrangian wave-speeds (C) are directly related to the slopes of the stress-strain curve as $C = \left(\sqrt{\frac{1}{\rho_0} \frac{d\sigma}{d\varepsilon}} \right)$. It can thus be seen that the initial loading wave-speeds are C_L (elastic longitudinal wave-speeds), followed by a region of plastic loading. The initial unloading wave-speed is significantly higher than the plastic loading wave-speed, due to a steep slope in the stress-strain curve when release begins. The quasi-elastic unloading region then follows this, wherein the unloading wave speed gradually reduces until it intersects with the plastic loading path. The strength of the material can be inferred from the size of the quasi-elastic region. A comparison between the typical Lagrangian wave-speed vs. particle velocity (or strain) plots observed in SLG is presented in Chapter 3.

Although the shock and release technique is a convenient way to measure the strength of materials at extremely high pressures, its reliance on measurement of peak loading and unloading stresses result in large relative uncertainties in the measured yield strength. An alternate technique of measuring the strength of materials more accurately at lower pressures is the Pressure Shear Plate Impact (PSPI) experiment. A brief discussion of this technique and its potential application to SLG is provided in Chapter 4.

References

- ¹S. J. Tracy, S. J. Turneure, and T. S. Duffy, “In situ x-ray diffraction of shock-compressed fused silica,” *Physical Review Letters* **120**, Publisher: American Physical Society, 135702 (2018).
- ²L. M. Barker and R. E. Hollenbach, “Laser interferometer for measuring high velocities of any reflecting surface,” *Journal of Applied Physics* **43**, Publisher: American Institute of Physics, 4669–4675 (1972).
- ³O. T. Strand, D. R. Goosman, C. Martinez, T. L. Whitworth, and W. W. Kuhlow, “Compact system for high-speed velocimetry using heterodyne techniques,” *Review of Scientific Instruments* **77**, Publisher: American Institute of Physics, 083108 (2006).
- ⁴G. I. Kanel, A. M. Molodets, and A. N. Dremin, “Investigation of singularities of glass strain under intense compression waves,” *Combustion, Explosion and Shock Waves* **13**, 772–777 (1977).
- ⁵G. I. Kanel, S. V. Rasorenov, and V. E. Fortov, “The failure waves and spallations in homogeneous brittle materials”, in *Shock Compression of Condensed Matter–1991*, edited by S. C. Schmidt, R. D. Dick, J. W. Forbes, and D. G. Tasker (Elsevier, Amsterdam, Jan. 1992), pp. 451–454.
- ⁶S. V. Rasorenov, G. I. Kanel, V. E. Fortov, and M. M. Abasehov, “The fracture of glass under high-pressure impulsive loading,” *International Journal of High Pressure Research* **6**, Publisher: Taylor & Francis, 225–232 (1991).
- ⁷R. J. Clifton, M. Mello, and N. S. Brar, “Effect of shear on failure waves in soda lime glass,” *AIP Conference Proceedings* **429**, Publisher: American Institute of PhysicsAIP, 521 (1998).
- ⁸N. S. Brar, Z. Rosenberg, and S. J. Bless, “Spall strength and failure waves in glass,” *Le Journal de Physique IV* **01**, Publisher: EDP Sciences, C3–639–C3–644 (1991).
- ⁹N. S. Brar, S. J. Bless, and Z. Rosenberg, “Impact-induced failure waves in glass bars and plates,” *Applied Physics Letters* **59**, Publisher: American Institute of Physics, 3396–3398 (1991).
- ¹⁰C. H. M. Simha and Y. M. Gupta, “Time-dependent inelastic deformation of shocked soda-lime glass,” *Journal of Applied Physics* **96**, Publisher: American Institute of Physics, 1880–1890 (2004).
- ¹¹G. I. Kanel, S. V. Rasorenov, and V. E. Fortov, *Shock-wave phenomena and the properties of condensed matter, Chapter 4*. (Springer Science & Business Media, Mar. 2004).
- ¹²D. Grady, “Shock compression of ceramics with microstructure,” in *Physics of Shock and Impact, Volume 2 Materials and shock response, Chapter 6* (IOP Publishing, 2017).

- ¹³R. J. Clifton, “Analysis of failure waves in glasses,” *Applied Mechanics Reviews* **46**, Publisher: American Society of Mechanical Engineers Digital Collection, 540–546 (1993).
- ¹⁴H. D. Espinosa, X. Yueping, and N. S. Brar, “Micromechanics of failure waves in glass: I. Experiments,” *Journal of the American Ceramic Society* **80**, Publisher: Wiley Online Library, 2061–2073 (1997).
- ¹⁵C. Frohlich, “Deep earthquakes”, Publisher: Cambridge University Press (2006).
- ¹⁶X. Markenscoff, “Volume collapse instabilities in deep-focus earthquakes: a shear source nucleated and driven by pressure,” *Journal of the Mechanics and Physics of Solids*, 104379 (2021).
- ¹⁷H. Aben, J. Anton, M. Öis, K. Viswanathan, S. Chandrasekar, and M. M. Chaudhri, “On the extraordinary strength of Prince Rupert’s drops,” *Applied Physics Letters* **109**, Publisher: American Institute of Physics, 231903 (2016).
- ¹⁸M. M. Chaudhri, “The role of residual stress in a Prince Rupert’s drop of soda-lime glass undergoing a self-sustained and stable destruction/fracture wave,” *Physica Status Solidi (a)* **206**, 1410–1413 (2009).
- ¹⁹J. C. F. Millett and N. K. Bourne, “Effect of internal strain on the propagation of failure in shock loaded soda-lime glass,” *Journal of Applied Physics* **95**, Publisher: American Institute of Physics, 4681–4686 (2004).
- ²⁰L. Davison, *Fundamentals of Shock Wave Propagation in Solids*, Shock Wave and High Pressure Phenomena (Springer-Verlag, Berlin Heidelberg, 2008).
- ²¹M. A. Meyers, “Shock Waves: Equations of State,” in *Dynamic Behavior of Materials*, Section: 5 (John Wiley & Sons, Ltd, 2007), pp. 124–151.
- ²²J. R. Asay and J. Lipkin, “A self-consistent technique for estimating the dynamic yield strength of a shock-loaded material,” *Journal of Applied Physics* **49**, Publisher: American Institute of Physics, 4242–4247 (1978).
- ²³J. R. Asay, T. Ao, J.-P. Davis, C. Hall, T. J. Vogler, and G. T. Gray, “Effect of initial properties on the flow strength of aluminum during quasi-isentropic compression,” *Journal of Applied Physics* **103**, Publisher: American Institute of Physics, 083514 (2008).
- ²⁴T. J. Vogler, T. Ao, and J. R. Asay, “High-pressure strength of aluminum under quasi-isentropic loading,” *International Journal of Plasticity*, Special Issue In Honor of Dattatraya (Datta) Dandekar **25**, 671–694 (2009).
- ²⁵T. Ao, M. D. Knudson, J. R. Asay, and J.-P. Davis, “Strength of lithium fluoride under shockless compression to 114 GPa,” *Journal of Applied Physics* **106**, Publisher: American Institute of Physics, 103507 (2009).

*Chapter 2***PROBING THE PROPERTIES AND MECHANISMS OF
FAILURE WAVES IN SODA-LIME GLASS****2.1 Introduction**

In the context of shock compression, soda-lime glass (SLG) and other silica glasses containing network modifiers such as aluminosilicate glass, K8 glass, lead-filled glass, and Corning glass have been attributed a feature commonly known as the 'failure wave' [1–4]. It is observed that behind this wave, the material has zero spall strength and reduced shear strength [4, 5]. The mechanism underlying these observed features concerning strength and their correlation to the failure wave is still a topic of considerable debate [6, 7].

Significant advances in understanding the properties of the failure wave phenomenon were made in the past decades. Failure waves were first observed in shock wave experiments on K-8 glass by Kanel et al [8]. In their work, the authors noticed that the tensile wave in the spall experiment was reflected off a failed section of glass near the impact surface. Later, shock-wave experiments [2] investigating failure waves in glass targets of different thicknesses observed that the propagation velocity of these waves decreased with distance. In general, experiments [2, 9] to determine the speed of the failure wave as a function of the impact-stress used embedded lateral stress gauges or rear free surface velocimetry recordings. Embedded manganin stress-gauges revealed a wave of increasing lateral stress behind the primary shockwave, indicating a significant decrease in the material's shear strength. This decrease in shear-strength was attributed to the failure wave, which was estimated to travel at a speed of 2.2-2.6 km/s. A similar decrease in shear-strength of SLG behind the failure wave was detected using pressure-shear plate impact experiments in [10].

Shock compression experiments conducted by [2, 11] used a velocimetry technique (VISAR) to probe the rear surface motion of impacted glass target specimens. The failure wave speed was estimated based on the arrival of a recompression bump in the velocity record [2] or the early arrival of a tensile wave pullback signal [11]. Failure wave speeds in the range 1.0 -1.5 km/s were reported based on these methods. Simha et al. [12] pointed out that the failure wave speed determined by the use of lateral stress-gauges differed from that determined by the use of rear-

surface velocimetry. They suggest this is possible because the reduction in shear strength and the observed recompression bump are due to two different underlying reasons. This indicates that the assumption of attributing the recompression wave to the failure wave needs to be examined using additional experiments. Another significant observation in their study is that the longitudinal stress record has a two-wave structure for impact stresses higher than 5 GPa. The second compression wave is seen to travel at a speed of 1.6 km/s, which is close to the failure wave speed suggested by free surface particle velocity measurements [2, 13]. It was therefore inferred that the recompression-bump observed in earlier experiments [2, 13] was due to this second wave. The two-wave structure for the longitudinal compression was not observed in SLG for impact stresses higher than 10 GPa, possibly indicating the disappearance of failure waves at these higher stresses. However, there are no experiments to conclusively verify the presence/absence of failure waves at these impact stresses.

Previous works using longitudinal and lateral stress gauges [9], normal plate impact [13] and pressure shear plate impact [10] on SLG ascertain the failure wave stress threshold to be around 5 GPa. In the normal plate impact experiments on SLG [13], the authors observed that the impact surface was rendered opaque with the onset of failure waves, thus precluding velocimetry on that surface. The significant inferences from this observation would be the instantaneous nucleation of failure and the comminution of SLG behind the failure waves. However, possibly due to the use of higher intensity laser for velocimetry, this opacity of the impact surface was not observed in recent experiments [14] on SLG at similar impact stresses. There have also been several works to investigate, hypothesize and infer the mechanism responsible for the failure wave phenomenon [6, 7, 15–17].

Bourne et al. [17] attempted to image failure waves in SLG by observing the SLG target laterally during impact using high-speed photography. However, those experiments observed the presence of ‘failure waves’ at impact-stresses as low as 2.5 GPa. Also, these failure waves were seen to travel as fast as 3.6 km/s, which is significantly different from observations made in other plate-impact studies on failure waves. More recently, Bauer et al. [18] performed similar experiments to image failure waves in SLG disks during impact, by observing the target laterally and from its rear surface using high-speed photography. In their experiments, two sets of failure fronts were observed to propagate in SLG: a ‘surface failure front’ and an ‘internal failure front.’ The surface failure front is observed to travel as fast as the

loading shock-wave (6 km/s). This surface failure is attributed to the fracturing of glass at the lateral surface of the disk, presumably due to lateral stress release. The internal failure front speed, as inferred from streak analysis of the laterally captured images, was seen to be ranging from 0.8-2.1 km/s in their experiments. The streak-photography also shows increased opacity of SLG behind the internal failure front, thus indicating significant damage accumulation and/or refractive index change in the SLG. It can be thus inferred that the ‘internal failure front,’ and not the ‘surface failure-front,’ corresponds to the ‘failure wave’ phenomenon under investigation in the current work. This ‘surface failure front’ could have resulted in the abnormally high failure wave speed observed in earlier imaging works [17].

There have been numerous attempts to model the failure wave and replicate the various features it introduces in shock compression experiments. Partom [19] used a phenomenological model, relating the rate of damage accumulation to the gradient of damage to successfully replicate the speed of the failure wave, loss of shear strength and increase in transverse-stress behind the failure wave. The same was also achieved in a model by Feng [20] and Chen et al. [21] who postulate that failure waves are caused due to shear induced micro-fissures (differing from microcracks by a length scale) and dilatation. They formulate a spatial diffusion of these micro-fissures and attendant damage to replicate the effects of the failure wave. Said and Glimm [22] support this diffusion-based approach for damage, comparing it to a deflagration wave, and provide a thermodynamics basis for the model. The thermodynamic basis also accommodates Clifton’s [6] phase transition postulate for the failure wave, which is discussed later in this section.

‘Failure wave-like’ phenomena are not restricted only to normal [23] silica glasses, but are seen in many other ceramics, such as borosilicate glass, quartz, ruby, and alumina. In their plate-impact experiments, Chocron et al. [24] observed that borosilicate glass experienced significant damage and had close to zero spall strength for impact stresses as small as 1 GPa. However, it was observed that there was no distinct ‘propagating front’ separating the damaged section from the intact material, i.e, a ‘failure wave’ was not observed in borosilicate glass at these stresses. Other features characteristic of failure waves, such as the ‘recompression-bump’ (discussed earlier), was also not observed in their velocimetry record. Kanel et al. [1, 25] observed that quartz and ruby experienced an almost complete loss of spall strength when shock-compressed to stresses above their Hugoniot Elastic Limit (HEL). Dandekar and Bartowski[26] observed similar loss of spall strength in alumina AD995

for impact-stresses higher than its HEL. Cooper et al.[27] also observed delayed failure in alumina AD995, similar to failure waves, with the use of lateral stress gauges. The speed and existence of failure-waves in the aforementioned materials have not been investigated. Furthermore, the mechanism underlying this behavior of ceramics is yet unknown, and might differ for normal glasses [23] and other brittle ceramics.

Although the mechanism underlying the failure wave phenomenon remains elusive, there seem to be roughly two categories of hypotheses which attempt to capture different features of the failure wave – the ‘local material hypotheses’ and ‘nonlocal material hypotheses’ (terminologies adapted from Kanel et al.[1]). The nonlocal hypotheses assert that the failure wave is essentially due to surface imperfections in the surface of the glass, which in turn leads to nucleation of defects, which then propagates into the glass as failure waves. A common feature of a nonlocal hypothesis is that it models glass material inside the bulk to have properties different from the glass material on the surface [28, 29], or the glass material’s property depends on the adjacent element’s property [19]. Examples of nonlocal hypotheses for the failure-wave phenomenon include Feng’s [20] work and that of Kanel [1] and Espinosa et al. [7, 30]. Feng [20] suggests that a tilt between the impactor and target nucleates micro-fissures at the impact surface, which then diffuse into the bulk of the glass as ‘failure waves.’ Similarly, Kanel [1] and Espinosa et al. [7, 30] suggest that the failure wave phenomenon is due to microcracks that nucleate at the impact surface and propagate into the glass. Recent work on dynamic fracture in SLG have shown cracks propagating at speeds of around 1.5 km/s under mode-I loading conditions [31]. This is consistent with the speed of failure waves observed in SLG. Additionally, past works by Chen and Ravichandran [32] and Kanel [1] suggest a ‘wing crack’ model that can explain the axial propagation of cracks under the near-hydrostatic stress states encountered by failure waves. The microcrack hypothesis would also assign a significant role to the surface roughness of the impact surface in the formation of failure waves. However, Raiser and Clifton [3] observed that varying the surface roughness of the alumino-silicate glass had no significant effect on the formation or speed of the failure waves. The microcrack hypothesis also fails to anticipate a secondary compression carried by the failure wave, giving rise to the recompression bump and the two-wave structure observed in experiments [2, 12, 33]. Additionally, there seems to be no clear consensus regarding mechanisms and features of the proposed crack nucleation and propagation, further complicating the evaluation of its veracity.

In contrast, the ‘local’ hypotheses consider the failure wave phenomenon to result solely from the glass’ material behavior, regardless of the material’s position. Examples of such hypotheses can be found in the works of Grady [34] and Clifton [6]. Grady [34] proposes a meso-kinetic theory that govern the strength of brittle solids to explain the delayed failure observed in SLG. They suggest that the failure wave phenomenon is a result of a probabilistic activation of defects and delayed fracture in the glass material. Further, the time span of the delay in fracture is postulated to depend on the loading-rate, critical stress intensity factor of the material, and a characteristic meso-scale correlation length. Notably, this theory involves nucleation of failure within the bulk of the material and does not require surface-imperfections to nucleate ‘failure waves.’ This theory also explains the relaxation of longitudinal stress observed behind the failure wave in some experiments [12, 34, 35]. Clifton [6] attributes the failure wave to a phase transition/atomic coordination change occurring within the SLG, resulting in densification and cracking of the material behind this wave. This would be consistent with the two-wave structure of the longitudinal stress observed by Simha et al. [12] and the nucleation of cracks seen behind the failure wave seen by Bourne et al. [9, 17] and Chocron et al. [24]. A similar phase-change/coordination change was also hypothesized to explain the shear localization and reduction in strength of silica-glass with pressure [36, 37]. Markenscoff [38] suggests that volume collapse in materials under pressure causes shear instabilities, which in Schill et al.’s [37] work was seen to be important to model failure waves in fused silica rods. Therein, it was proposed that the change in the coordination number of the atoms from 4-fold to an intermediate 5-fold structure results in a temporary reduction in shear strength of fused silica [39]. However, the magnitude of densification and the kinetics associated with the proposed phase-change [40] remains unclear, thereby complicating a rigorous evaluation of this hypothesis. Further experiments and insightful inferences are essential to unequivocally establish the mechanism responsible for failure waves in shock compression experiments on normal [23] glasses. The present work will only consider the ‘microcrack’ hypothesis [1, 7, 30] and the ‘phase transition/densification’ hypothesis [6] for evaluation and comparison. Since these hypotheses are representative of their respective categories (‘nonlocal’ and ‘local’ hypotheses), the other hypotheses can be evaluated/verified in a similar manner.

The present work attempts to critically examine the various open questions that remain regarding failure waves in glasses, including the possible mechanisms for their existence. In summary, shock compression and spall experiments at different

stresses together with numerical simulations seek to address the following questions:

1. Is the recompression wave [2, 4, 13] observed in normal plate-impact experiments caused by the failure wave? Can computational simulations and models of SLG aiming to reproduce this recompression bump offer insights into the mechanism responsible for the failure wave?
2. Does the failure wave exist in SLG for impact-stresses higher than 8 GPa [4]? If not, this would be a yet unexplored additional feature of the failure wave that could help infer the mechanism responsible for the failure wave and inelastic deformation in SLG.
3. Do failure waves form on secondary surfaces in SLG, or do failure waves originate only from the impact surface? Formation (non-formation) of failure waves on a secondary surface such as a SLG-SLG interface [33, 41] would support (contradict) the microcrack hypothesis.
4. Does the onset of failure waves cause SLG to become opaque near the impact-surface as observed by Dandekar and Beaulieu [13]?
5. Can any insightful inferences be drawn from experimental or simulation results to establish/discount any of the hypotheses regarding the mechanism of the failure wave?

A description of the materials used in the experiments and the design of experiments to address the questions summarized above are presented in Sec. 2.2. The results from the shock compression and spall experiments conducted over a range of impact stresses are presented and discussed in Sec. 2.3. A summary and conclusions for the study are presented in Sec. 2.4.

2.2 Materials and methods

The normal plate impact experiments conducted in this work involved tungsten carbide (WC) disks impacting soda-lime glass (SLG) disk targets as shown in Fig. 1. The SLG disks were sourced from University Wafers, Inc., South Boston, MA and had densities of $2,480 \pm 10 \text{ kg/m}^3$. The disks were 30 mm in diameter and had an average surface roughness of less than 1 nm. Two experiments used 6 mm thick disks, while all other SLG disks were 5 mm thick. The WC impactors were of BC-00 grade sourced from Basic Carbide Corporation, Lowber, PA. The WC impactors

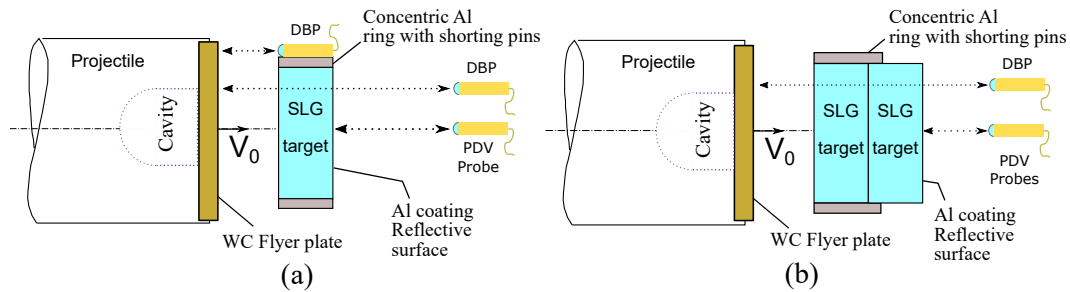


Figure 2.1: Schematics of normal impact experiments on SLG and the velocity measurement using Photonic Doppler Velocimetry (PDV). The Down-Barrel Probe (DBP) measures the velocity of the WC impactor. The cavity in the projectile behind the WC flyer plate ensures release to zero stress at the WC rear surface. (a) Regular configuration used for most experiments. (b) Layered glass impact configuration used for experiment #AJ-3.

had a density of $15,480 \pm 100 \text{ kg/m}^3$, and its stress-particle velocity Hugoniot was taken from Kettenbeil [42]. The WC disks were 34 mm in diameter, and the thicknesses varied depending on the experiment. A $0.5 \mu\text{m}$ thick aluminum layer was vapor-deposited onto the rear surface of the SLG to provide a reflective coating for velocimetry. This surface was slightly scuffed with a 1200 grit size sandpaper prior to vapor-depositing aluminum on it. The roughened surface diffuses the reflected light and thus prevents the loss of signal that might arise due to any tilt present in the angle of impact. Free surface velocity measurements were conducted using Photonic Doppler Velocimetry (PDV) employing a 1550 nm wavelength laser [43]. The impact velocity was obtained using an additional PDV probe called the Down-Barrel Probe (DBP) (Fig. 2.1(a)). This probe is generally mounted next to the target with its face flush to the impact face of the target. In two of the experiments (#AJ-2, #AJ-3), however, they were mounted alongside the PDV probe, gauging the impactor surface velocity before and after impact (Fig. 2.1(b)).

The spall experiments performed herein can be broadly classified into two types, with the spall plane/tensile wave formation i) ahead of, and ii) behind the failure wave. The location of the spall plane was varied by changing the thickness of the impactor. A rough initial estimate of the failure wave velocity was needed to predict whether the spall plane forms ahead or behind the failure front. The initial estimate of the failure wave speed in glasses (1.3 km/s) was taken from spall experiments by Kanel et al. [11] and embedded stress-gauge experiments by Kanel et al. [33] on SLG. The speed of the failure wave was observed to be invariant with stress and was thus assumed to be a constant in designing all the experiments. Also, it

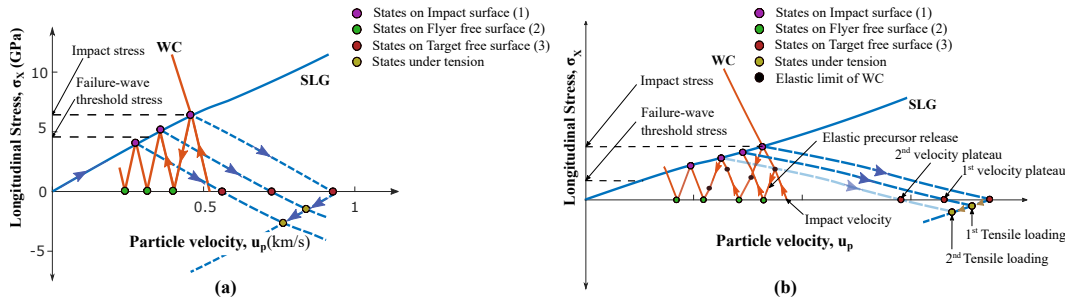


Figure 2.2: Schematic stress-particle velocities (a) for experiments with impact stress less than 7.5 GPa. SLG can be assumed to be elastic at these stresses [35], making the loading and release paths identical. (b) for experiments with impact stresses higher than 7.5 GPa, which exceeds the Hugoniot elastic limit of WC.

should be noted that there is a range of feasible thicknesses for the flyer plate for experiments with a spall plane ahead of the failure wave. The flyer thickness should be small enough to allow formation of a tensile wave ahead of the failure wave and large enough to prevent the stresses on the impact-surface from unloading below the failure wave threshold. Representative Hugoniot curves for low and high impact-stress experiments are shown in Figs. 2.2 (a) and (b). The Hugoniot curves provide an estimate of the stress and particle velocities, and their evolution with time, at the surfaces of the WC impactor and the SLG target.

For experiments with tensile wave formation ahead of the failure wave, the failure wave speed can be estimated from the thickness of the failed-section and arrival time of the recompression. The material distance-time ($X-t$) characteristic diagram drawn alongside the experimental results can also be used to infer the Lagrangian speed of the failure wave using its slope on the diagram. Two of the spall experiments also involved probing the velocity of the WC Impactor surface sample as shown in Fig. 2.1. These experiments were designed to verify claims made by Dandekar and Beaulieu [13] regarding opacity of the impact surface with the onset of failure waves in SLG for impact stresses higher than 5 GPa.

Summary of experiments

A summary of the experiments performed is shown in Table 2.1. A compilation of all the free surface velocity recordings is shown in Fig. 2.3, with the shock arrival times normalized by the thickness of the SLG targets in each experiment. The impact stresses shown in Table 2.1 were computed using shock-Hugoniot data for SLG [35] and WC [42] (see Appendix A). The intersection of the Hugoniot curves of SLG and WC in the longitudinal stress-particle velocity ($\sigma_x - u_p$) plane provides the solution to

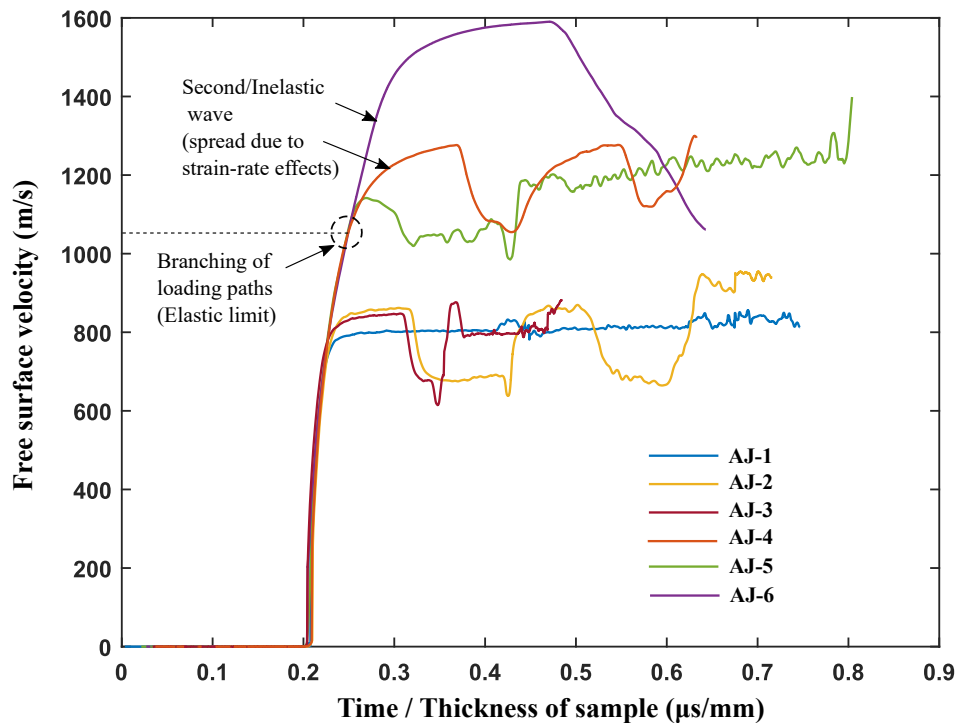


Figure 2.3: Summary of the free rear surface velocity recordings for all experiments. The horizontal axis representing time is scaled by sample thickness to match wave-arrival timings for all experiments.

the impact-stress and the interface velocity after impact. The uncertainties in the measured particle velocities arise primarily due to an uncertainty in identifying the peak frequency in the power spectrum of the short-time Fourier transform [44]. The uncertainties in particle velocities, shown in Table 2.1, are estimated following procedures outlined in [42, 45].

The significant features highlighted in these results are the relatively large rise times of the inelastic waves and the deviation of the compression/loading curves from each other above a threshold impact stress. The free surface particle velocity corresponding to the onset of inelastic deformation in SLG appears to be approximately 1,050 m/s. This measured free surface velocity implies an in-material particle velocity of 525 m/s corresponding to the onset of inelastic shock waves. This value matches the elastic limit observed by Alexander et al. [35] (Fig. A.1).

Modeling soda-lime glass behavior and numerical simulations

Figure 2.4 shows the schematic of the 2-D plane-strain simulation, performed in the commercial finite element analysis (FEA) software LS-DYNA [46] used to compute

| Expt. # | WC-impactor thickness (mm) | SLG target thickness (mm) | Impactor velocity (m/s) | Impact stress (GPa) | Observed peak free surface velocity (m/s) | Failure wave speed ^a (km/s) |
|---------|----------------------------|----------------------------------|-------------------------|---------------------|---|--|
| AJ-1 | 4.98 | 5.96 | 520±0.84 | 6.4±0.01 | 800±0.39 | 1.3 |
| AJ-2 | 1.99 | 4.96 | 519±1.90 | 6.4±0.02 | 860±0.31 | 1.3 |
| AJ-3 | 3.65 | 9.90 (4.95/4.95) ^b | 514±2.35 | 6.4±0.03 | 848±0.05 | 1.3/0.5 ^c |
| AJ-4 | 1.06 | 5.85 | 750±3.21 | 8.3±0.03 | 1141±0.07 | 1.3 |
| AJ-5 | 3.08 | 4.96 | 770±2.78 | 8.5±0.03 | 1275±0.07 | 1.3 |
| AJ-6 | 5.01 | 4.95 | 992±8.10 | 10.8±0.03 | 1590±0.32 | N/A ^d |

Table 2.1: Summary of experimental conditions and results. ^aFailure wave speed in material frame. ^bThickness of the first/second SLG disk in this experiment. ^cSpeed of the failure wave in the first/second SLG disk in this experiment. ^dNo failure wave was observed in this experiment.

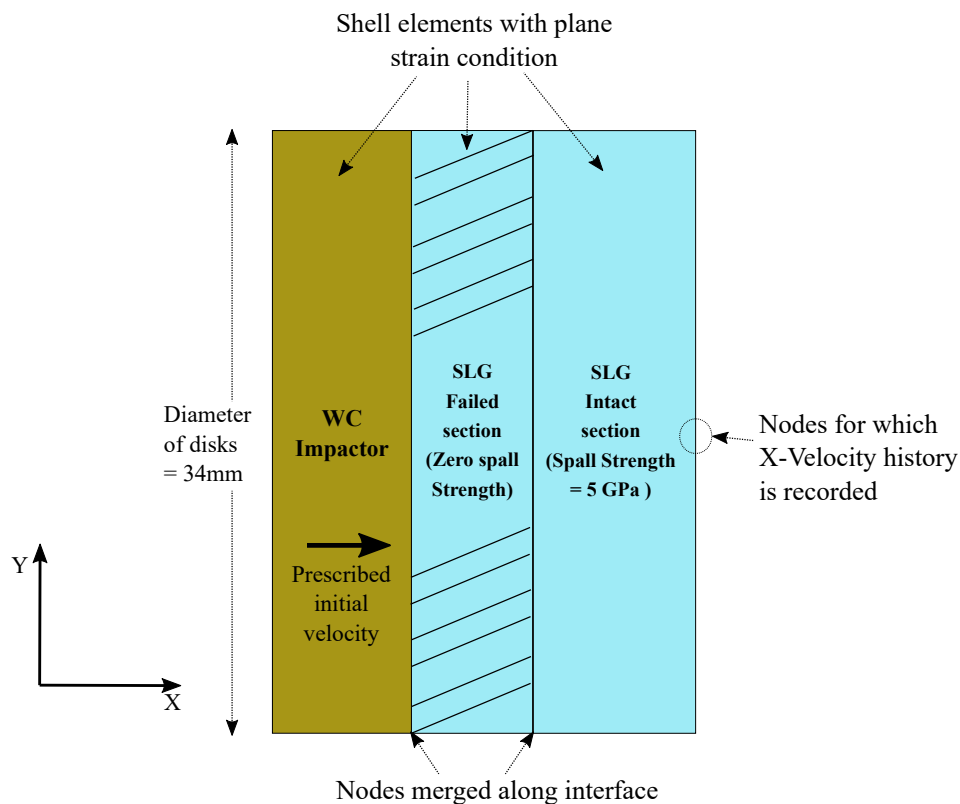


Figure 2.4: Schematic of the simulation domain used in the modeling of experiments on soda-lime glass.

the shock compression response of SLG in the experiments. The longitudinal stress-volumetric strain and pressure-volumetric strain Equations of State (EOS) employed are shown in Fig. 2.5. EOS-1 was used for simulating experiments with impact stresses higher than the Hugoniot Elastic Limit (HEL) of SLG. EOS-2, which incorporates an abrupt densification in SLG, was used to capture the velocity deficit and recompression bumps caused by the failure wave at lower stresses. Further details regarding the derivation of these EOS are provided in Appendix A.

For uniaxial strain conditions, with impact/loading along the X-axis:

$$\sigma_x = \begin{cases} p + \frac{4G\epsilon_{vol}}{3} & \epsilon_{vol} < \epsilon_{HEL} \\ p + \frac{2Y(\epsilon_p)}{3} & \epsilon_{vol} \geq \epsilon_{HEL} \end{cases} \quad (2.1)$$

where p is the pressure, G is the shear modulus, Y is the yield-strength of the material, and ϵ_p is the effective inelastic strain accumulated in the material. The simulation uses J_2 von Mises plasticity yield criterion.

The pressure p is given by:

$$p = \left(\frac{\sigma_x + 2\sigma_y}{3} \right) \quad (2.2)$$

where σ_x and σ_y are the longitudinal and lateral (transverse) stresses, respectively.

In the simulations, the pressure for the SLG Hugoniot is prescribed as a function of the volumetric strain (ϵ_{vol}) in a tabulated form as discussed in Appendix A. This relation between p and ϵ_{vol} is called an Equation of State (EOS). For a given uniaxial strain (ϵ_{vol}), the value of p and σ_x is computed from the EOS and Eq. 2.1, respectively. Then, the lateral stress(σ_y) is computed using Eq. 2.2.

The uniaxial strain is related to the current density (ρ) and initial (reference) density (ρ_0) by:

$$\epsilon_{vol} = 1 - \frac{\rho_0}{\rho} \quad (2.3)$$

The rounding of the elastic wave in the rear surface velocity record for SLG can be attributed to its initial concave-down compression Hugoniot (Fig. A.2). Also, as seen in Fig. 2.3, the second inelastic wave undergoes significant dispersion (spreading) [34, 35]. This makes defining a clear Hugoniot Elastic Limit (HEL) for SLG more challenging. To address this, a novel technique was employed by Alexander et al. [35] using the loading-unloading hysteresis in the stress-strain curves to infer the HEL of SLG to be 7.5 GPa. Kanel [1] suggests that the rounding

of the second velocity peak observed in SLG for plate impact experiments can be attributed mainly to strain-rate effects that prevail in silica glasses and other ceramics as well. A Cowper-Symonds rate-hardening expression is used to capture strain-rate effects. Other relevant properties of SLG such as the shear modulus and bulk modulus were taken from Kettenbeil's work [42]. A summary of SLG properties used in the simulations and experimental design is provided in Table 2.2.

The yield surface for strength, Y is computed using a power law hardening model with strain hardening. Temperature effects are not accounted for in the simulations as the impact stresses and inelastic effects cause relatively small temperature rise [42]. The strain hardening parameters for SLG are chosen to keep strain hardening effects negligible. In simulations using EOS-2, both strain-hardening and the strain-rate hardening were neglected as EOS-2 is employed only for impact stresses below the HEL, where hardening effects are not relevant. The flow stress, Y is expressed as:

$$Y(\varepsilon_p, \dot{\varepsilon}_p) = \left(Y_0 + B\varepsilon_p^n \right) \left(1 + \left(\frac{\dot{\varepsilon}_p}{C\dot{\varepsilon}_{p0}} \right)^{\frac{1}{P}} \right) \quad (2.4)$$

where Y_0 is the initial yield strength (HEL), n is the strain-hardening exponent, and P is the strain-rate hardening parameter. B and C are material constants and $\dot{\varepsilon}_{p0}$ is the reference strain-rate for the simulation. The values of the various constants used in the simulation of SLG are shown in Table 2.2. The parameters B , n , P and C were obtained by calibrating the strength model to reproduce the SLG behavior for past experiments [28, 47] and $\dot{\varepsilon}_{p0}$ is taken to be 10^6 s^{-1} . The initial yield strength (Y_0) is inferred from the HEL using Eq. 2.5. It can be seen from Fig. 2.5 that the strain at yield, $\varepsilon_{HEL} = 0.1005$. Thus, using Eq. 2.5, $Y_0 = 6.13 \text{ GPa}$.

$$Y_0 = 2G\varepsilon_{HEL} \quad (2.5)$$

The Grüneisen Parameter (Γ_0) used for SLG was computed from data provided in Grady and Chhabildas [48]. However, as discussed in Appendix A, changing the Grüneisen Parameter was seen to have no significant effect on the simulations.

The failed section, as shown in Fig. 2.4, is a section of material with properties slightly different from the intact section. The failed section used here has a fixed-length equal to the Lagrangian distance travelled by the failure front, which is taken to propagate at a speed of 1.3 km/s before it is arrested by a release wave. This

| Density, ρ_0 (kg/m ³) | Shear Modulus, G (GPa) | Bulk Modulus, K (GPa) | Grüneisen Parameter, Γ_0 |
|---|------------------------------|-----------------------------|------------------------------------|
| 2480 | 30.5 | 45.3 | 5.06 |

| Model Parameters (Eq. 2.4) | | | | |
|----------------------------|---------|-----|-----|---|
| Y_0 (GPa) | B (GPa) | n | C | P |
| 6.1 | 1.0 | 0.8 | 900 | 2 |

Table 2.2: Properties of soda-lime glass used in the simulations.

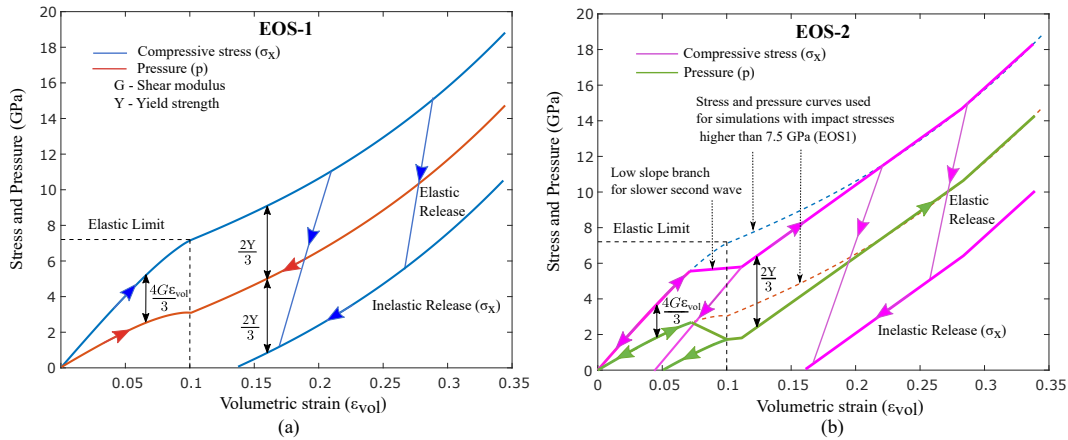


Figure 2.5: Pressure and stress vs. volumetric strain Equations of State (EOS) used to model behavior of SLG. (a) EOS-1 was used to model SLG for impact stresses higher than 7 GPa. (b) EOS-2 was used for SLG at impact stresses below 7 GPa, which incorporates densification in order to capture the slower second compression wave. The details of the construction of the two equations of state are presented in Appendix A.

thickness of the failed section is inferred from the X-t diagram for the experiment and is used here to emulate the effect of the failure wave. The material in the failed section has the same compressive strength and EOS definition as the intact section, however its tensile/spall strength is different. The failed section is assigned zero (no) spall strength, whereas the intact section has a spall strength of 5 GPa. Past experiments [3] have shown that silica glasses with failure wave phenomenon retain spall strengths higher than 4.4 GPa in the intact section ahead of the failure front.

Past experiments using lateral stress gauges [5, 9] and PSPI technique [10] have also observed a reduction in shear strength of the material behind the failure wave. These features of a propagating failure front and reduced yield-strength behind the failure front were not incorporated in these simulations. The thickness of the failed

| Density, ρ_0 (kg/m ³) | Shear Modulus, G (GPa) | Bulk Modulus, K (GPa) | Model Parameters (Eq 2.4) | | | | |
|---|------------------------------|-----------------------------|---------------------------|---------|------|------|---|
| | | | Y_0 (GPa) | B (GPa) | n | C | P |
| 15480 | 273 | 379 | 4.3 | 9.2 | 0.38 | 1500 | 2 |

| C_0 (m/s) | Grüneisen Parameter, Γ_0 | S | $\dot{\epsilon}_{p0}$ (s ⁻¹) |
|-------------|------------------------------------|-------|--|
| 4930 | 1.62 | 1.309 | 10 ⁶ |

Table 2.3: Material properties of tungsten carbide (WC) used in the simulations [42, 49].

section in an experiment is initially estimated using the X-t characteristic diagram assuming elastic longitudinal wave speeds. A better estimate for the thickness of the failed section is obtained by calibrating the thickness to get a better agreement between the simulation and observed free surface velocity record.

Properties of the tungsten carbide (WC) impactor used in the experiments are summarized in Table 2.3. The EOS used for WC is the standard Mie-Grüneisen form shown below,

$$U_s = C_0 + S [u_p] \quad (2.6)$$

where C_0 is the bulk sound speed, U_s is the Lagrangian shock-wave speed, S is a material parameter, and $[u_p]$ is the jump (increase) in particle velocity across the shock.

2.3 Results and discussion

Experiment #AJ-1 (Impact velocity, 520m/s)

The experiment #AJ-1 was designed and conducted to verify the existence of failure waves at impact stresses of around 6.4 GPa, slightly below the HEL of the material. The WC disk used was 5 mm thick and 34 mm in diameter. The SLG disk was 6 mm thick and 34 mm in diameter. Based on these thickness values and corresponding wave speeds, the spall plane is estimated to form behind the failure wave, thus probing the spall strength of SLG behind the expected failure front. Vapor deposited gold tabs as illustrated by Clifton and Jiao [50] were used for detecting the time of impact and to trigger the recording of the signal on the oscilloscope. Plots of the free surface velocity, as recorded by the PDV, along with the numerically simulated curves using the two equations of state (Fig. 2.5) are shown in Fig. 2.6. A few important observations from the plot are: (i) the lack of tensile unloading,

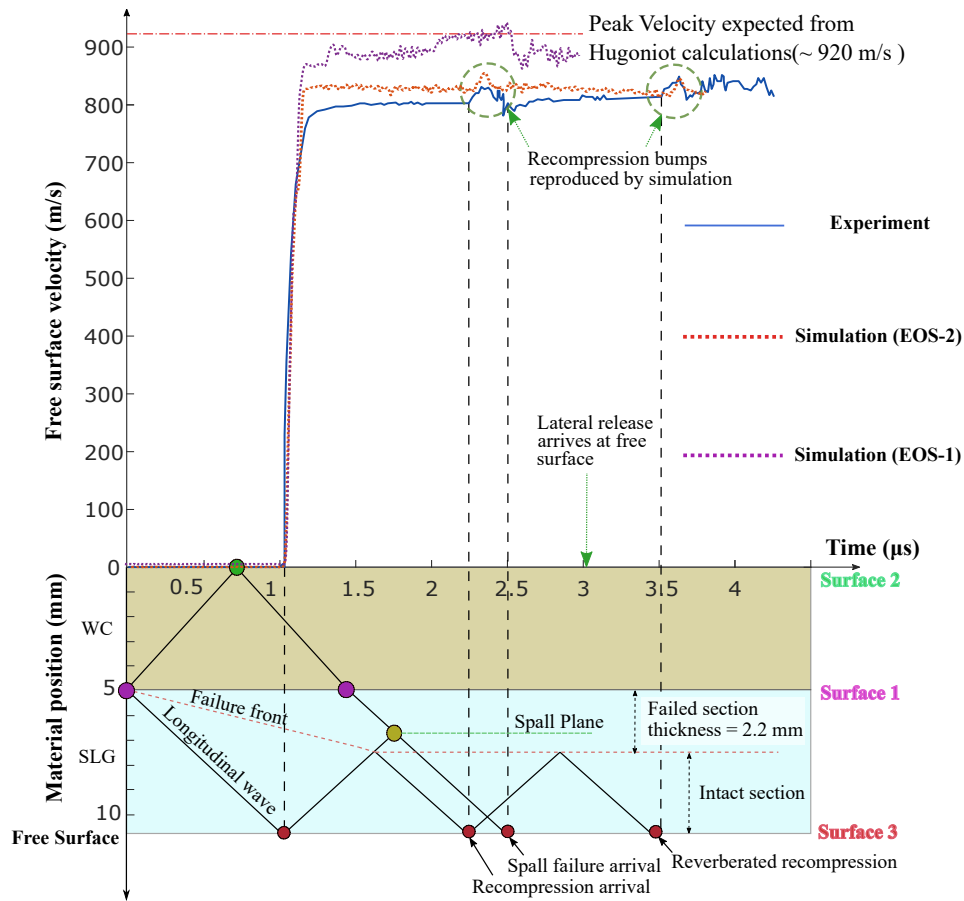


Figure 2.6: Free surface velocity vs. time alongside a schematic $X-t$ characteristic diagram for experiment #AJ-1. The spall plane was designed to be behind the failure front. Impact occurs at $t=0$.

(ii) a deficit of the peak velocity, (iii) a recompression bump which is also seen to reverberate.

The absence of a tensile unloading implies that the spall strength of the material behind the presumed failure wave is zero, indicating the presence of cracks/comminuted material in regions behind the failure wave. A small recompression at around $2.25 \mu\text{s}$ after the impact is also observed in the velocity record. This recompression has been observed in the past and is generally attributed to the interaction of the release wave from the free surface of the SLG with the failure front [4, 33]. As seen in Fig. 2.6, the arrival time of the recompression bump can be used to determine the speed of the purported failure wave by computing its slope in the $X-t$ characteristic diagram. The failure wave speed is thus seen to be 1.3 km/s in this experiment. The cause of the observed recompression bump and the nature of the interaction between the failure wave and the release wave is discussed later in this section. Another im-

portant observation from the velocity record is that the observed peak velocity (800 m/s) is significantly lower than the peak-velocity expected from Hugoniot calculations (920 m/s) and simulations using EOS-1 for SLG (see Fig. 2.6). This deficit in peak velocity (~ 120 m/s) could be due to a slower travelling second compression wave with a speed less than 1.5 km/s [34]. The recompression bump observed at roughly $2.25 \mu\text{s}$ can also be attributed to the interaction of the longitudinal release wave with this slower travelling second wave. A similar explanation to the origins of the recompression bump was proposed by Simha et al. [12]. Using embedded stress-gauges, they observed a second compression wave travelling at a speed of around 1.6 km/s, similar to the failure wave speed observed in the current work.

This observation lends support to the hypothesis that the observed ‘failure wave’ could be a result of phase-transition/atomic coordination number change [6, 37] occurring within the SLG. Such phenomena are usually associated with significant densification and localized strains [6] that could cause comminution of the material behind the phase-change wave. Localized nucleation of cracks behind the failure front, as would be expected from this hypothesis, were observed by Bourne et al. [9]. As mentioned earlier, an alternate hypothesis is that failure waves arise due to microcracks nucleating on the impact-surface and propagating into the SLG material [1, 7]. However, this hypothesis does not predict a deficit in peak velocity and a recompression bump, both of which are observed in the current experiment. Also, the observed deficit in velocity seems to discount the hypothesis [13] that the material behind the failure front possesses lower impedance as compared to the intact material. Presence of a growing layer of low-impedance material between the impactor and intact material would entail a peak-velocity higher than the expected 920 m/s. It would also entail a distinct reverberation and ringing-up of longitudinal stress as observed in plate-impact experiments with low-impedance samples sandwiched between high impedance anvils [50]. To the authors’ knowledge, none of the stated features have been observed in previous plate impact experiments on SLG.

From Eq. A.4 (Appendix A), it can be seen that the speed of an inelastic shock-wave has to be greater than the material’s bulk wave speed at a given strain. The bulk wave speed evaluated using Eq. A.3 (Appendix A) at the peak-strain observed in this experiment is 3.1 km/s, which is significantly higher than the observed failure wave speed of 1.3 km/s. It can thus be inferred that the failure wave/second compression wave is not a regular inelastic wave.

Another important observation from Fig. 2.6 is the reverberation of the recom-

pression. This is consistent with the understanding that the failure front stops propagating upon interacting with the longitudinal release wave from the free surface of the SLG. A similar experiment was carried out by Ginzburg and Rosenberg [51] using stress gauges to record longitudinal stress. However, it is unclear as to why no reverberations were observed in their investigation. The tensile waves cause the material behind and ahead of the failure front to separate from each other at the failure front. This gives rise to the reverberations observed within the intact section of the SLG seen in Fig. 2.6. The results of simulations attempting to model this experiment are also presented in Fig. 2.6. EOS-1 (Fig. 2.5(a)) is modified to obtain EOS-2 (Fig. 2.5(b)), which includes densification, and thus accounts for a second compression wave with a speed of 1.3 km/s. The simulation with EOS-2 and 2.2 mm thick failed-section accurately captures the peak velocity observed in the experiment. Notably, the timings of the recompression and reverberation bumps are also precisely captured. This validates the pre-estimated thickness of the failed section used in the simulation. The success of the simulation in capturing these previously elusive features lends further support to the hypothesis of a slower second compression wave being associated with the failure wave phenomenon.

Experiment #AJ-2 (Impact velocity, 519m/s)

The experiment #AJ-2 was designed for two purposes: (i) to ascertain if the recompression bump observed in experiment #AJ-1 is due to interaction with the failed section or due to a separate compression wave, and (ii) to check for opacity of the impact surface of the SLG in the presence of failure waves, as observed by Dandekar and Beaulieu [13].

The arrival time of the recompression bump, as shown in Fig. 2.6, has been used to ascertain the speed of the failure wave from spall experiments by other authors in the past [4, 33]. However, it is yet to be verified if the observed recompression is due to the failure wave or an altogether different compression wave. This question was raised by Simha et al. [12] where they noted that experiments using transverse stress gauges and experiments using the arrival timing of the recompression bump yielded significantly different values for the failure wave speed. To address this discrepancy, the spall experiment was designed to have the spall plane ahead of the failure wave as shown in Fig. 2.7. This direct method seems to be the most reliable among the techniques to determine the speed of the failure wave [11]. The experimental results shown in Fig. 2.7 consists of the observed free surface velocity record of the SLG alongside the characteristic X-t diagram. The figure also shows the post-impact

apparent/observed velocity history at the impact surface recorded by the Down-Barrel probe (DBP). It can be noted that the failure wave does not seem to render the impact surface of SLG opaque. The velocity record from the DBP before impact (not shown) was used to ascertain the impactor velocity. An appropriate window correction factor must be applied to the velocity record to infer the actual post-impact impactor-target interface velocity. To the authors' knowledge, the window correction factor for SLG with 1550 nm wavelength light at various stresses is yet to be experimentally determined. The peak-velocity of the free surface velocity record is approximately the same as that of the other experiments with similar impact stresses. An important feature to note from Fig. 2.7 is the reverberation of the compressive stress in the intact section of the SLG. These reverberations observed within the intact section of the SLG indicate complete separation of the intact and failed sections of the SLG at the failure front. This longitudinal fissure along the failed-front further suggests that the material behind the failed-front is thoroughly comminuted. It remains unclear, however, as to whether/how axially propagating microcracks could result in such thorough comminution of material under shock compression. A fast phase-transition/densification causing localized nucleation of cracks and rapid comminution could be a better explanation for this observation.

Also, it is observed that the failure wave stops propagating after interacting with the tensile wave. This can be noted from the X-t characteristic diagram and from the results of simulations using a fixed failed-section length of 2 mm. As shown in Fig. 2.8, the presence of hydrostatic tension at a crack tip is expected to promote unstable propagation of the crack. This would mean that the interaction of the tensile wave with the failure front would have accelerated the axial propagation of the failure wave rather than arrest it as observed. Therefore, this result seems to discount the presence of axially oriented cracks in the failed section at these impact stresses.

The use of EOS-1, as seen in experiment #AJ-1 (Fig. 2.6) cannot reproduce the deficit in the peak velocity. Thus, the simulations made use of the EOS-2 equation of state and a failed section length of 2 mm for SLG. The resulting peak velocities and reverberation features of the simulation are in good agreement with the experimental observation. These results, as in the case of #AJ-1, seem to indicate the presence of a slower travelling secondary compression wave, which could be due to a densification in the SLG.

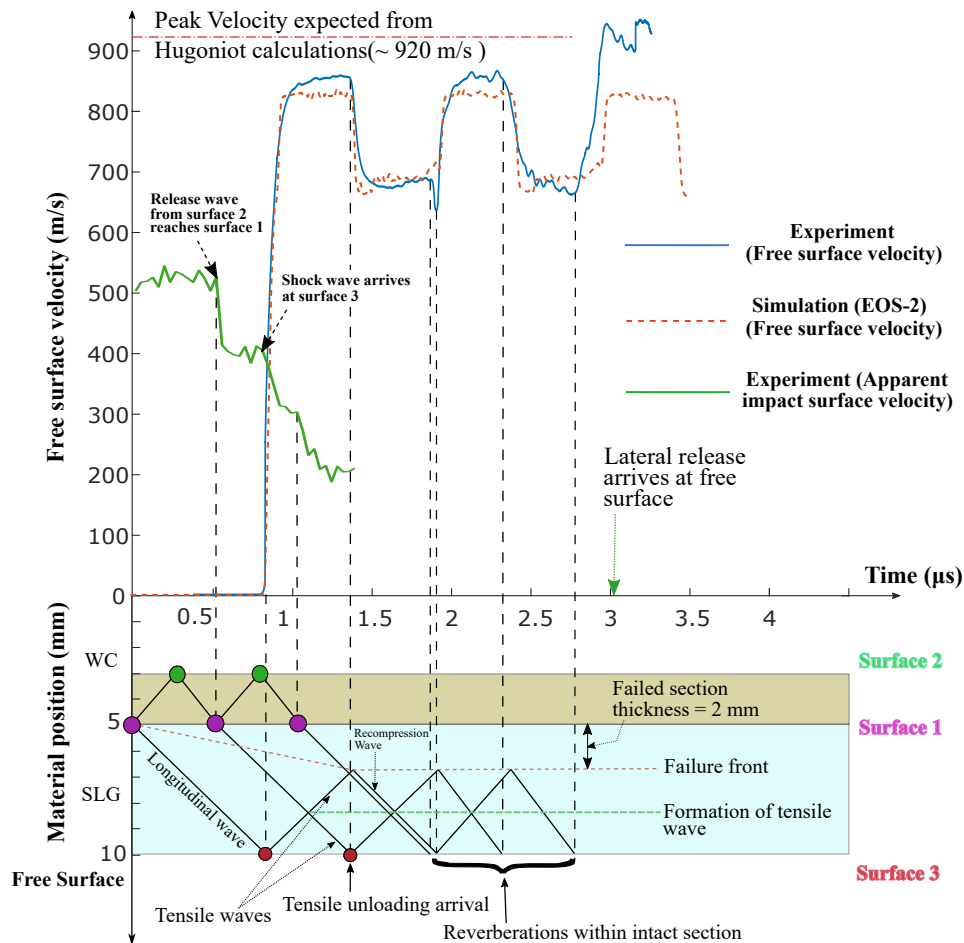


Figure 2.7: Schematic X-t characteristic diagram and free surface velocity vs. time plots for experiment #AJ-2. The apparent velocity of the impact surface obtained using the DBP is also shown. The tensile wave is formed ahead of the failure front.

Experiment #AJ-3 (Impact velocity, 514m/s)

The experiment #AJ-3 involved a 3.7 mm thick WC disk impacting a 9.9 mm thick target consisting of two 4.95 mm SLG disks held together without any air gap in between them. The SLG disks were glued only at the outer periphery. Schematic of this experiment can be seen in Fig. 2.1(b). The purpose of this experiment was to discern if the failure wave phenomenon is due to microcracks propagating into the SLG from its impacted surface or due to a bulk phenomenon like phase-transition. If failure waves arise due to the former reason, then an identical failure wave can be expected to re-originate from surface #4 (Fig. 2.9) when the longitudinal wave from the impact surface arrives there. There would then be an absence of tensile unloading observed at the rear surface (surface #3). This is because the spall plane would be almost coincident with the expected failure front. Also, as seen earlier

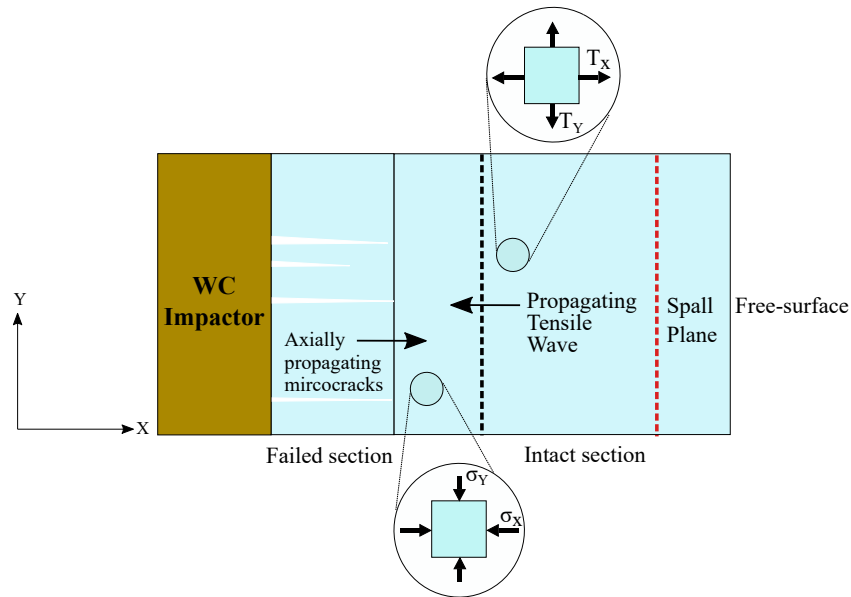


Figure 2.8: Schematic showing the interaction of tensile wave from the rear free surface with failure wave in experiment #AJ-2 (Fig. 2.7). The tensile wave is expected to further aid in propagating the axial cracks

from results of experiment #AJ-1 (Fig. 2.6), failure waves are known to result in a deficit in the peak-velocity [1, 12, 48]. Therefore, in the event of generation of failure waves at the SLG-SLG interface, there could be a further reduction in longitudinal stress/peak normal velocity observed at the rear free surface.

If the failure waves were due to a bulk phenomenon like phase transition, there would be no failure waves that originate from the SLG-SLG interface. There would then have been no early pullback from the failure front and no reduction in the free surface velocity from its earlier value of 834 m/s (Fig. 2.7). In the absence of failure waves from the SLG-SLG interface, a pullback can be expected at around $3.42 \mu\text{s}$ due to interaction of the tensile wave with the SLG-SLG interface. The free surface velocity recorded at surface #3 is shown in Fig. 2.9. The impact velocity was 514 m/s, and the impactor-face velocity recorded by the DBP is also shown in Fig. 2.9. The figure also presents the changes in the apparent impact surface velocity correlated with events during the experiment. These changes are effected either by the change in velocity of the impact interface or due to abrupt changes in the refractive index of the SLG [52, 53]. It can be noted that, similarly to experiment #AJ-2 (Fig. 2.7), there are significant fluctuations in the impact-surface velocity immediately after impact. This could be due to the failure wave causing partial reduction in transmissibility of the SLG to 1550 nm laser light. A similar result

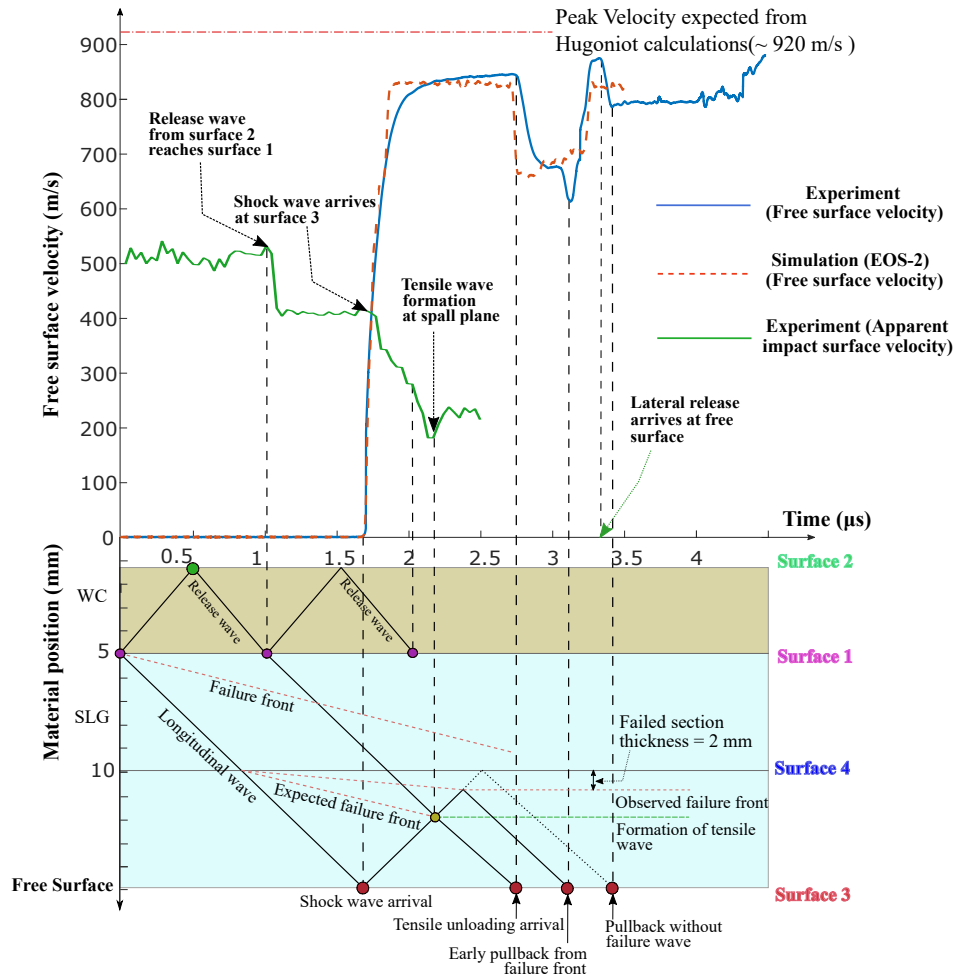


Figure 2.9: Free surface velocity vs. time plots and a schematic of the X-t characteristic diagram for experiment #AJ-3. The material-speed of the failure wave observed in the second glass layer is 0.477 km/s, as compared to 1.3 km/s observed in the first glass layer

was noted by Renganathan et al. [14] for impact stresses between 4 and 7.5 GPa. However, unlike Dandekar and Beaulieu's work [13], there was no complete loss of light (opacity) observed with the onset of the failure wave.

It can be seen from the schematic X-t characteristic diagram in Fig. 2.9, that the observed normal velocity profile indicates the presence of a slower travelling failure wave in the second SLG disk. The speed of the failure wave observed in the second SLG disk is 0.477 km/s as opposed to the 1.3 km/s speed of failure wave in the first SLG disk. Another important observation is that the observed peak free surface velocity is the same as previous experiments, 834 m/s (#AJ-1 and #AJ-2). This would mean that the second failure wave did not reduce the peak longitudinal stress

as the first failure wave is seen to have in previous experiments. Kanel's [1, 33] experiments with layered glass targets glued together with embedded stress-gauges showed a different outcome. Each layer of SLG was seen to reduce the longitudinal stress by a similar amount and the failure wave was seen to have the same velocity (1.5 km/s) in each SLG disk. The exact cause for the difference in observations between the current experiment and past works [33] remains unclear.

A similar experiment on layered SLG disks had been carried out by Bourne et al. [41] with the use of embedded lateral stress gauges. It was also observed that the failure waves originate at the SLG-SLG interface. However, the speed of the failure wave in the second SLG and the peak longitudinal stress could not be observed with only lateral stress gauges. Also, the use of embedded lateral stress gauges being intrusive, the interface between SLG and the stress-gauge could be a source of failure (cracks/debonding).

The simulations for this experiment made use of the EOS-2 equation of state with 0.85 mm thick failed section for the SLG. The primary features of the observed velocimetry record such as the deficit in peak-velocity, arrival times and amplitudes of the tensile, and recompression waves are adequately captured. This lends further credibility to the employed model of SLG (EOS-2), which involves a permanent densification.

Experiment #AJ-4 (Impact velocity, 750 m/s)

The experiment #AJ-4 was conducted to probe the existence and speed of the failure wave at impact stresses higher than 8 GPa. The WC impactor used in this experiment was 1.06 mm thick and 34 mm in diameter. The SLG disk was 6 mm thick and 34 mm in diameter. The measured free surface velocity profile is shown in Fig. 2.10. Due to the use of a thin WC impactor and faster release wave speeds in SLG, the stress wave attenuates as it propagates into the SLG. Additionally, the higher stresses involved give rise to a separate inelastic wave in the WC impactor. These factors make a complete X-t characteristic diagram more complicated to construct and interpret. The important observations made from experimental data and simulation results are summarized in Fig. 2.10.

A recompression signal can be observed in the experimental data at around 2.3 μ s. The simulations employing EOS-1 equation of state and a 2 mm thick 'failed-section' of material approximately captures the time of arrival of the recompression. It can thus be inferred that the failure wave exists at this impact stress and travels

at a speed of around 1.3 km/s, which is same as its speed at lower impact-stresses. An additional complication arises here due to the fact that the initial elastic release-wave speeds are significantly larger than the shock-wave speeds [35]. This causes the compressive stress-wave to attenuate as it travels through the SLG, and thus interferes with measurement of the failure wave speed at a constant stress level. As discussed in Appendix A, the simulation can be expected to capture this attenuation better with improvements in modelling the release behavior of SLG.

It should also be noted from the stress-particle velocity Hugoniot shown in Fig. 2.2(b), that the stress on surface #2 (Fig. 2.10) does not fall below the failure wave threshold [13] in the course of this experiment. Thus, the failure wave is expected to travel until it encounters the release wave from surface #3. Another observation that is made by comparing the experimental data to the simulation result is that the data shows only one velocity plateau/tensile pullback before the recompression arrives. The simulation predicts two other velocity plateaus which are not observed in the experimental result. There are two plausible explanations for this difference. One reason could be that the tensile waves that give rise to the first and second velocity plateaus are significantly slower than anticipated for SLG (as marked in X-t diagram in Fig. 2.10). The slope of the stress-particle velocity relation was assumed to be the same in compression and tension for the simulation. A slower tensile wave could explain why the second tensile wave pullback could not arrive before the observed recompression. Another possible reason is that the SLG could have transitioned from brittle-failure to inelastic deformation or ductile-failure at these high tensile and compressive stresses [54]. This would give rise to a prolonged first plateau followed by a recompression due to material failure. If this is the case, the observed recompression might not be due to the failure wave at all. Further analysis of the results, comparison with high-fidelity simulations, and other experiments at these stresses would be needed to evaluate the above hypotheses.

Experiment #AJ-5 (Impact velocity, 770 m/s)

The experiment #AJ-5 involved the impact of a 3.1 mm thick WC flyer on a 4.95 mm thick SLG disk at an impact velocity of 770 m/s. The purpose of this experiment was to further verify and improve upon the findings of experiment #AJ-4, which was at a similar impact stress. Also, similarly to experiments #AJ-2, #AJ-3, and #AJ-4, the spall plane was designed to be in the intact material ahead of the expected failure front. A recompression/pullback is expected at the rear surface due to interaction of the tensile wave with the failure front. The X-t characteristic diagram and the

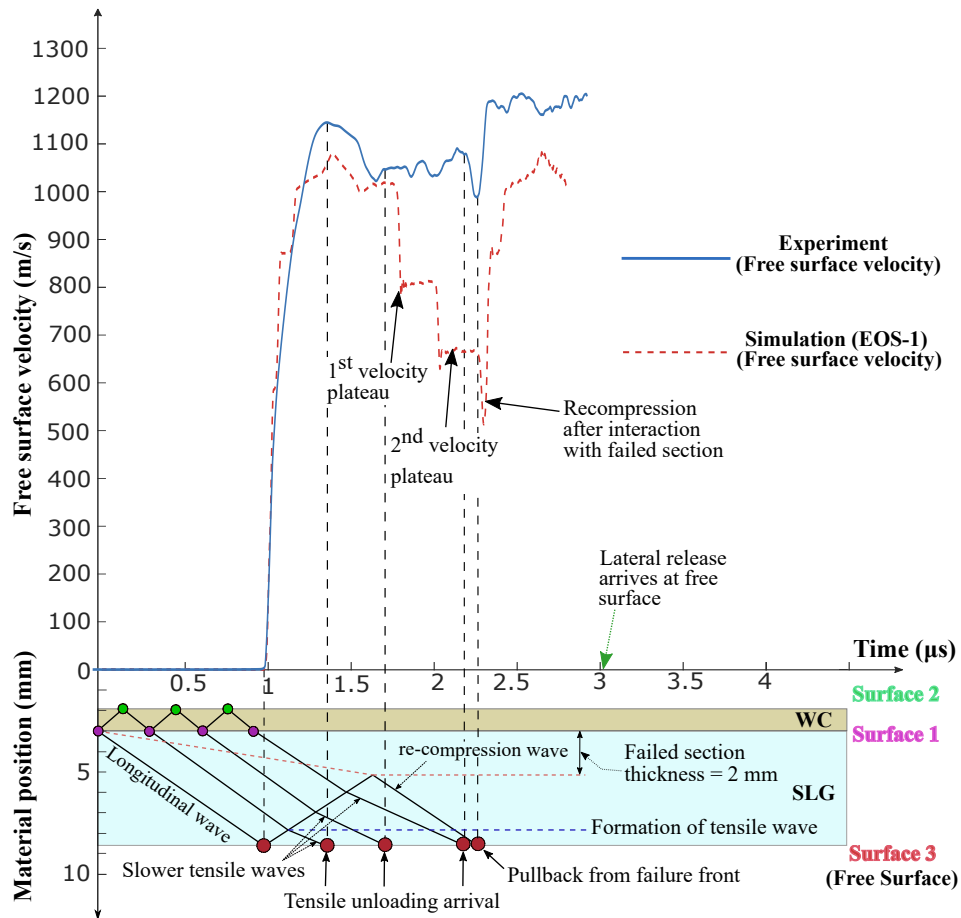


Figure 2.10: Free surface velocity vs. time plots and a schematic of the X-t characteristic diagram for experiment #AJ-4. Owing to high rise time of shocks in SLG and the use of a thin WC impactor, the stress-wave is attenuated as it propagates through the SLG. Simulations predict two additional tensile unloading which are not observed in the experiment.

arrival timing of the recompression can be used to compute the failure wave speed.

The results of the experiment and simulation are presented in Fig. 2.11 alongside the X-t characteristic diagram. The impactor used in this experiment, unlike the one used in experiment #AJ-4, is thick enough to avoid complications arising from attenuation of the stress-wave as it propagates through the SLG. Additionally, the thicknesses of the WC and SLG disks permit recording of multiple reverberations at the free surface of the SLG.

Although involving similar impact stresses, the extended velocity plateau, observed upon tensile unloading in experiment #AJ-4, is not observed in this experiment. This could be due to the lack of a second tensile unloading in the current experiment. Another important observation can be made from the X-t characteristic diagram in

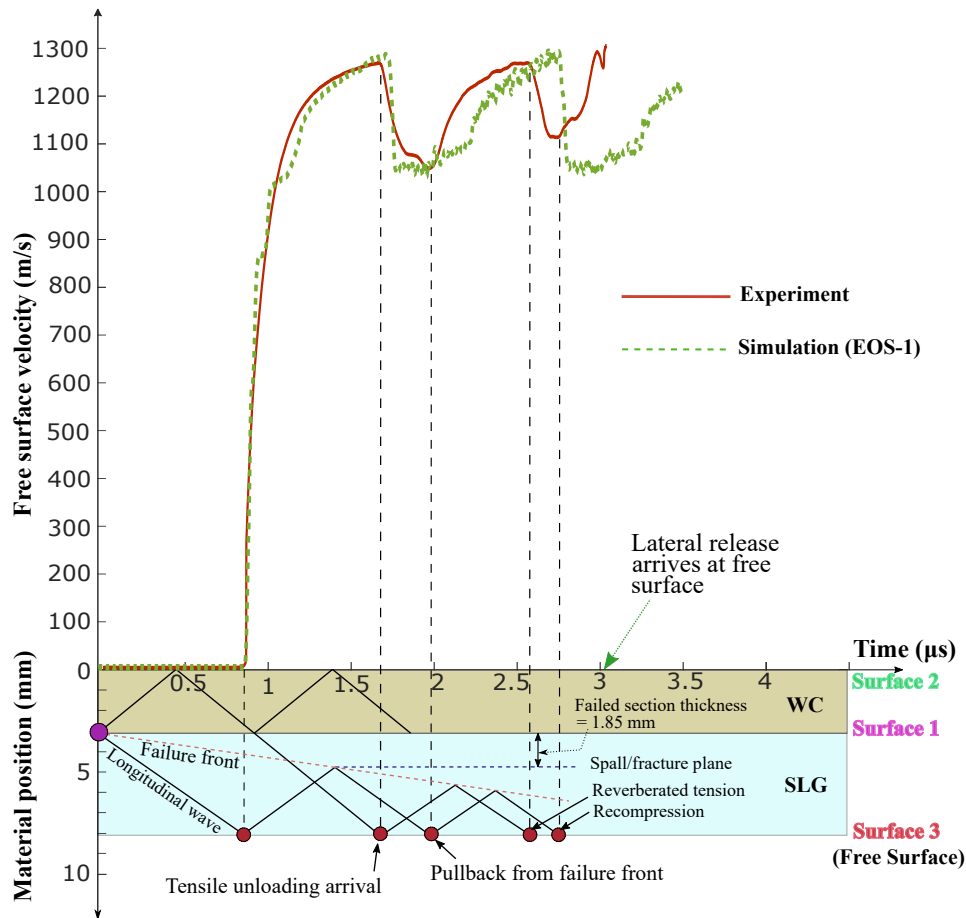


Figure 2.11: Free surface velocity vs. time and a schematic X-t characteristic diagram for the experiment #AJ-5. The formation of tensile wave is ahead of the failure wave. The reverberations indicate that the failure wave continues to propagate at 1.3 km/s after interacting with the tensile wave.

Fig. 2.11. The arrival times of the reverberations indicate that the failure wave continues to propagate into the SLG at an unchanged speed of 1.3 km/s, despite its interaction with the tensile waves from the spall plane. This is in stark contrast to the results of experiment #AJ-2, wherein the tensile wave was seen to arrest the propagation of the failure wave. This could be due to the effect of the multi-axial tensile stress-state on an axially oriented crack as shown in Fig. 2.8. However, similar to experiment #AJ-2, the reverberations observed in this experiment suggest that the intact and failed sections of the material separate longitudinally at the failure front.

The simulation used to replicate this experiment employed EOS-1 equation of state and a 1.85mm thick failed section for SLG. The rounded compression feature of the free surface velocity and the peak velocity are well captured by the simulation. The

simulation also captures the time of arrival and amplitude of the tensile unloading at the rear surface of the SLG. However, the arrival-timing of the reverberations were not captured by the simulation. This is primarily due to the use of a fixed length for the failed section in the simulation, in contrast to the experimentally observed failure wave that continues to propagate despite interacting with the tensile wave.

It is important to note here that the simulations successfully captured the observed peak-velocity while using the EOS-1 equation of state, which does not involve a second compression wave due to densification. This would imply that the deficit in peak-velocity caused by the failure wave in experiments #AJ-1, #AJ-2 and #AJ-3 is not observed in this experiment. This further indicates that a slower second compression wave could be absent in this experiment. The cause underlying this observation is unclear, considering that a distinct second-wave travelling at 1.6 km/s was observed at impact stresses of 8 GPa by Brar et al. [4] and Simha et al. [4, 12]. Future work which can account for the release behavior of SLG (Appendix A) is needed. This may help achieve a better agreement between the simulation and experiment even while using EOS-2, thereby resolving the problem of an apparently missing second wave.

Experiment #AJ-6 (Impact velocity, 992 m/s)

The experiment #AJ-6 was conducted to probe the existence of failure waves at a high impact-stress of around 11 GPa. The WC impactor was 5 mm thick and 34 mm in diameter. The SLG target was 5 mm thick and 30 mm in diameter. The thicknesses of the WC and SLG disks were chosen such that the tensile wave-origin/spall plane was behind the failure front, similar to experiment #AJ-1. The high initial release wave speeds at surface #2, expected at these high-impact stresses [35], is also accounted for in the $X-t$ diagram (Fig. 2.12).

In the presence of a failure wave, just as seen in Fig. 2.6 for experiment #AJ-1, there would be no tensile unloading observed. However, the most significant observation that can be made from the results in Fig. 2.12 is the unloading due to the formation of tensile waves in SLG. This clearly shows that failure waves cease to exist at impact velocities above 992 m/s with WC impactor, which corresponds to an impact-stress of 10.8 GPa. To the authors' knowledge, this is the first experiment to gauge the spall strength of SLG at these impact stresses. Such an observation was also made in the case of K-8 Glass by Razorenov and Kanel [2]. Therefore, this could be a previously unexplored feature of the failure wave phenomenon itself rather than that

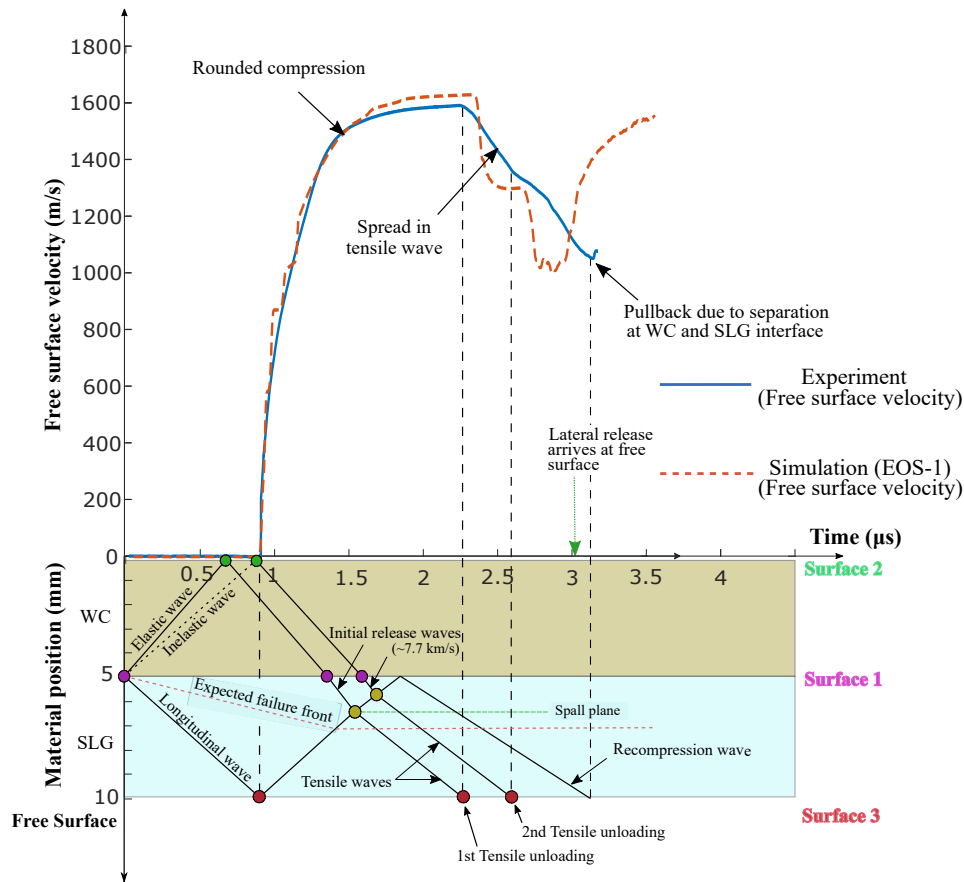


Figure 2.12: Free surface velocity vs. time and a schematic X-t characteristic diagram for the experiment #AJ-6. The high speed of initial-release waves [35] were accounted for in the X-t diagram. The speed of the tensile waves was inferred from the velocity profile. Failure waves are absent in this experiment and no failed section was used in the simulation.

of a specific glass, i.e, failure waves disappear at higher stresses for all glasses.

This observation presents another challenge to inferring the mechanism responsible for the failure wave phenomenon. Kanel [1] attempts to reconcile this observation with the hypothesis that the failure waves are due to microcracks propagating into the sample from the impact surface [7]. He hypothesized that at certain higher stresses characteristic to the material, the higher pressures could suppress cracking thereby effecting a brittle-to-ductile transition in the material. Wing-cracks [32] that are known to propagate axially even under states of high pressures, should be explored as a plausible mechanism for the failure wave that is consistent with this observation.

The results of the simulation shown in Fig. 2.12 made use of the EOS-1 equation

of state, details of which are discussed in Sec. 2.2 and Appendix A. The simulation is seen to capture the significant features marked in the experiment, including the rounded (smooth) compression wave. The spread in the tensile unloading is yet to be captured by the simulations. However, the time of arrival of the shock wave, first and second tensile unloading-waves, and the respective stresses at the peaks are all well reproduced. The separation of the WC and SLG interface is also captured in the simulation. This simulation did not involve any failed section as was used in the previous simulation. The simulation reveals that the tensile stresses at the first and second unloading waves are roughly 1 GPa and 5 GPa, respectively. Given that the magnitudes of the first and second experimentally observed unloading were matched by the simulations, these tensile strengths can be considered reliable. The absence of failure waves at these stresses is thus re-confirmed by simulations, which show that the SLG material retained a tensile strength of at least 5 GPa.

Stress vs. volumetric strain

Figure 2.13 provides a summary view of the results in the form of a stress-strain graph. The results from the current work have been plotted alongside previous works on SLG (adapted from Gorfain et al. [28]). It should be noted that the in-material compressive stresses in SLG cannot be ascertained from free surface velocimetry data, due to the sudden release of stress at the free surface. The stresses and strains for the current work have been estimated using EOS-1 stress-particle velocity Hugoniot for SLG, and the equation of state shown in Table 2.3 for the WC impactor. The observed deficit in particle velocity and speed of the failure wave were used to infer the volume densification for experiments #AJ-1, 2, and 3 (see Eq. A.6 in Appendix A). It can also be observed that certain previous shock compression experiments at stresses similar to that of experiments #AJ-1, 2, and 3 do not report a likewise sudden densification. This could be due to not accounting for a deficit in peak velocity that might have occurred in those experiments.

The results of experiments #AJ-1, 2, and 3, which were carried out at nearly identical impact velocities, are seen to be within the uncertainty ranges of each other (Fig. 2.13). This illustrates the repeatability of these experiments which show almost identical densification due to the failure wave. Furthermore, since the simulations performed in the current work are able to reproduce the key features observed in the velocimetry data, it appears reasonable to attribute these features to the behavior of SLG, as opposed to an experimental artefact.

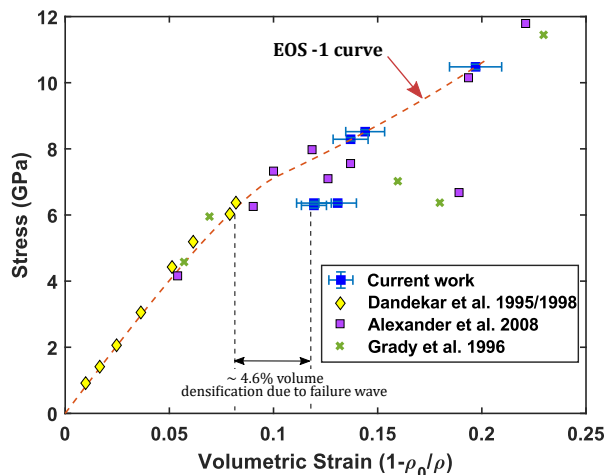


Figure 2.13: Stress vs. volumetric strain for SLG from the current work plotted alongside previous works by Dandekar et al. [13, 52, 53], Alexander et al. [47] and Grady et al. [48]. The data for the works of the other authors is adapted from the compilation provided by Gorfain et al. [28].

2.4 Conclusions

The experiments and simulations discussed in Sec. 2.3 provided significant insights into understanding the properties and mechanism of the failure wave phenomenon in soda-lime glass (SLG). The findings and inferences are summarized below:

- It was observed that the speed of the failure wave did not change appreciably with increase in impact stress, with its speed remaining at 1.3 km/s.
- It was observed that the failure wave phenomenon does not exist in SLG for impact stresses higher than 10.8 GPa.
- The results of experiments and relevant simulations strongly indicate that the failure wave carries an additional compressive-stress and densification. This seems to be the primary cause of the observed deficit in peak velocity. This secondary compression wave suggests that the failure wave phenomenon could be due to a phase-transition/densification in the SLG. The deficit in peak-velocity and lack of reverberations also indicate that there is no mismatch in impedance between the intact and failed sections of SLG. This would discount the hypothesis that the impedance of SLG behind the failure wave (failed section) is less than its impedance ahead of the failure wave (intact section).
- The recompression bump observed in the current and past works on shock

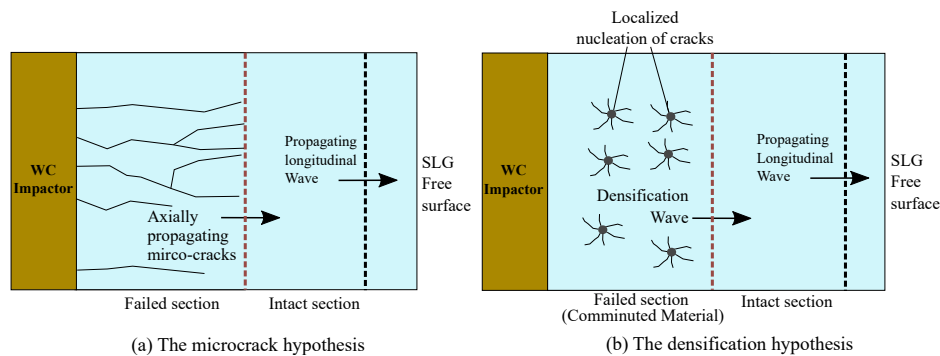


Figure 2.14: Schematics of two possible mechanisms to explain the cause of the failure wave phenomenon. (a) The microcrack hypothesis suggests that the failure wave is due to microcracks propagating into the SLG from the impact surface. (b) The densification hypothesis suggests that a slower phase transition-like densification causes cracking and comminution of the SLG material behind it.

compression of SLG can indeed be attributed to the slower traveling failure wave.

- The reverberations observed in the current work indicate the longitudinal separation of the intact and failed sections of SLG material. This is seen to occur when tensile waves interact with the failure front. At an impact stress of 6.4 GPa, this interaction is seen to arrest the failure wave propagation, which would discount the existence of axially oriented microcracks behind the failed section. However, at an impact stress of 8.5 GPa, the tensile wave is seen to have negligible effect on the propagation of the failure wave. This observed propagation of the failed section under zero-stress conditions seems to favor the microcrack hypothesis in explaining the origins of the failure wave phenomenon.
- The generation and propagation of failure waves at the SLG-SLG interface was observed. However, this second failure wave was seen to propagate significantly slower than the failure waves previously observed at this impact stress. The underlying reason for this peculiar observation is unclear. However, this observation seems to lend support to the hypothesis that failure waves are caused by microcracks propagating into the SLG from the impact surface.

The shock compression experiments on SLG were undertaken to evaluate the prominent hypotheses, as shown in Fig. 2.14, regarding the cause of the failure wave phenomenon. One of the hypotheses considered for evaluation, attributed the failure

wave phenomenon to a phase-transition/coordination number change of the atomic structure in the SLG causing comminution and localized nucleation of cracks in the material [6]. The other hypothesis was that the failure waves are due to microcracks propagating axially into the SLG from the impact-surface [30]. However, the mechanism underlying the failure wave phenomenon remains yet unclear, with existence of observations to support both class of hypotheses. Further experiments to visually observe the SLG impact surface during impact are necessary to decisively ascertain the mechanism underlying the failure wave phenomenon. It is suggested that such photography of the impact-surface of the SLG be performed longitudinally, [18, 55] as opposed to a previously attempted lateral observation [17] in order to avoid the interference caused by the ‘surface failure front’ [18].

Simulation using a user defined material model in LS-DYNA with a pressure dependent strength would be able to account for the reduction in strength observed behind a failure wave. Additionally, the available release wave speed data can be used to construct a more accurate stress-release and tensile behavior for SLG.

Finally, to the authors’ knowledge, no plate impact experiments have been performed on anomalous [23, 56] glasses such as fused silica glass and borosilicate glass to probe the existence of failure waves. Fused silica has no network modifiers [47] in its atomic structure and borosilicate-glass has boron atoms functioning as network-forming atoms. Unlike SLG, both these glasses are known to avoid cracking by undergoing significant densification in indentation tests [23, 56]. Plate impact experiments to investigate failure waves in these glasses can shed light on the unexplored role of network forming and network breaking ions in the failure wave phenomenon.

References

- ¹G. I. Kanel, S. V. Rasorenov, and V. E. Fortov, *Shock-wave phenomena and the properties of condensed matter, Chapter 4*. (Springer Science & Business Media, Mar. 2004).
- ²S. V. Rasorenov, G. I. Kanel, V. E. Fortov, and M. M. Abasehov, “The fracture of glass under high-pressure impulsive loading,” *International Journal of High Pressure Research* **6**, Publisher: Taylor & Francis, 225–232 (1991).
- ³G. Raiser and R. J. Clifton, “Failure waves in uniaxial compression of an aluminosilicate glass,” *AIP Conference Proceedings* **309**, Publisher: American Institute of Physics, 1039–1042 (1994).

- ⁴N. S. Brar, Z. Rosenberg, and S. J. Bless, “Spall strength and failure waves in glass,” *Le Journal de Physique IV* **01**, Publisher: EDP Sciences, C3–639–C3–644 (1991).
- ⁵N. S. Brar, S. J. Bless, and Z. Rosenberg, “Impact-induced failure waves in glass bars and plates,” *Applied Physics Letters* **59**, Publisher: American Institute of Physics, 3396–3398 (1991).
- ⁶R. J. Clifton, “Analysis of failure waves in glasses,” *Applied Mechanics Reviews* **46**, Publisher: American Society of Mechanical Engineers Digital Collection, 540–546 (1993).
- ⁷H. D. Espinosa, X. Yueping, and N. S. Brar, “Micromechanics of failure waves in glass: I. Experiments,” *Journal of the American Ceramic Society* **80**, Publisher: Wiley Online Library, 2061–2073 (1997).
- ⁸G. I. Kanel, A. M. Molodets, and A. N. Dremin, “Investigation of singularities of glass strain under intense compression waves,” *Combustion, Explosion and Shock Waves* **13**, 772–777 (1977).
- ⁹N. K. Bourne and Z. Rosenberg, “The dynamic response of soda-lime glass,” *AIP Conference Proceedings* **370**, Publisher: American Institute of Physics, 567–572 (1996).
- ¹⁰R. J. Clifton, M. Mello, and N. S. Brar, “Effect of shear on failure waves in soda lime glass,” *AIP Conference Proceedings* **429**, Publisher: American Institute of Physics, 521 (1998).
- ¹¹G. I. Kanel, S. V. Rasorenov, A. V. Utkin, H. He, F. Jing, and X. Jin, “Influence of the load conditions on the failure wave in glasses,” *High Pressure Research* **16**, 27–44 (1998).
- ¹²C. H. M. Simha and Y. M. Gupta, “Time-dependent inelastic deformation of shocked soda-lime glass,” *Journal of Applied Physics* **96**, Publisher: American Institute of Physics, 1880–1890 (2004).
- ¹³D. Dandekar and P. Beaulieu, “Failure wave under shock wave compression in soda-lime glass,” *Metallurgical and Material Applications of Shock-Wave and High-Strain-Rate Phenomena*, 211–218 (1995).
- ¹⁴P. Renganathan, Y. Toyoda, and Y. Gupta, “Optical Response of Soda-Lime Glass Shocked to 14 GPa,” *Journal of Dynamic Behavior of Materials* **6**, 207–212 (2020).
- ¹⁵D. E. Grady, “Shock-wave compression of brittle solids,” *Mechanics of Materials* **29**, Publisher: Elsevier, 181–203 (1998).
- ¹⁶D. E. Grady, “Shock deformation of brittle solids,” *Journal of Geophysical Research: Solid Earth* **85**, 913–924 (1980).

- ¹⁷N. K. Bourne, Z. Rosenberg, and J. E. Field, “High-speed photography of compressive failure waves in glasses,” *Journal of Applied Physics* **78**, Publisher: American Institute of Physics, 3736–3739 (1995).
- ¹⁸S. Bauer, F. Bagusat, E. Strassburger, M. Sauer, and S. Hiermaier, “New insights into the failure front phenomenon and the equation of state of soda-lime glass under planar plate impact,” *Journal of Dynamic Behavior of Materials* **7**, 81–106 (2021).
- ¹⁹Y. Partom, “Modeling failure waves in glass,” *International Journal of Impact Engineering* **21**, 791–799 (1998).
- ²⁰R. Feng, “Formation and propagation of failure in shocked glasses,” *Journal of Applied Physics* **87**, Publisher: American Institute of Physics, 1693–1700 (2000).
- ²¹Z. Chen, R. Feng, X. Xin, and L. Shen, “A computational model for impact failure with shear-induced dilatancy,” *International Journal for Numerical Methods in Engineering* **56**, 1979–1997 (2003).
- ²²H. Said and J. Glimm, “A continuum description of failure waves,” *Journal of Theoretical and Applied Mechanics* **56**, Number: 3, 657–674 (2018).
- ²³A. Arora, D. B. Marshall, B. R. Lawn, and M. V. Swain, “Indentation deformation/fracture of normal and anomalous glasses,” *Journal of Non-Crystalline Solids* **31**, 415–428 (1979).
- ²⁴S. Chocron, D. D. Barnette, T. J. Holmquist, C. E. Anderson, R. P. Bigger, and T. Z. Moore, “Damage threshold of borosilicate glass under plate impact,” *Journal of Dynamic Behavior of Materials* **2**, 167–180 (2016).
- ²⁵G. I. Kanel, S. V. Rasorenov, and V. E. Fortov, “The failure waves and spallations in homogeneous brittle materials”, in *Shock Compression of Condensed Matter–1991*, edited by S. C. Schmidt, R. D. Dick, J. W. Forbes, and D. G. Tasker (Elsevier, Amsterdam, Jan. 1992), pp. 451–454.
- ²⁶D. P. Dandekar and P. Bartkowski, “Shock response of AD995 alumina,” *AIP Conference Proceedings* **309**, Publisher: American Institute of Physics, 733–736 (1994).
- ²⁷G. A. Cooper, J. C. F. Millett, N. K. Bourne, and D. P. Dandekar, “Delayed failure in a shock loaded alumina,” *AIP Conference Proceedings* **845**, Publisher: American Institute of Physics, 847–850 (2006).
- ²⁸J. E. Gorfain, C. T. Key, and C. S. Alexander, “Application of a computational glass model to the shock response of soda-lime glass,” *Journal of Dynamic Behavior of Materials* **2**, 283–305 (2016).
- ²⁹T. J. Holmquist and G. R. Johnson, “A Computational Constitutive Model for Glass Subjected to Large Strains, High Strain Rates and High Pressures”, *Journal of Applied Mechanics* **78**, 10.1115/1.4004326 (2011).

- ³⁰H. D. Espinosa, X. Yueping, and N. S. Brar, “Micromechanics of Failure Waves in Glass: II, Modeling”, en, *Journal of the American Ceramic Society* **80**, 2074–2085 (2005).
- ³¹S. Dondeti and H. Tippur, “A comparative study of dynamic fracture of soda-lime glass using photoelasticity, digital image correlation and digital gradient sensing techniques,” *Experimental Mechanics* **60**, 10 . 1007 / s11340 - 019 - 00549 - 5 (2019).
- ³²W. Chen and G. Ravichandran, “Failure mode transition in ceramics under dynamic multiaxial compression,” *International Journal of Fracture* **101**, Publisher: Springer, 141–159 (2000).
- ³³G. I. Kanel, A. A. Bogatch, S. V. Rasorenov, and Z. Chen, “Transformation of shock compression pulses in glass due to the failure wave phenomena,” *Journal of Applied Physics* **92**, 5045–5052 (2002).
- ³⁴D. Grady, “Shock compression of ceramics with microstructure,” in *Physics of Shock and Impact, Volume 2 Materials and shock response, Chapter 6* (IOP Publishing, 2017).
- ³⁵C. S. Alexander, L. C. Chhabildas, and D. W. Templeton, “The Hugoniot elastic limit of soda-lime glass,” *AIP Conference Proceedings* **955**, Publisher: American Institute of Physics, 733–738 (2007).
- ³⁶W. Schill, S. Heyden, S. Conti, and M. Ortiz, “The anomalous yield behavior of fused silica glass,” *Journal of the Mechanics and Physics of Solids* **113**, 105–125 (2018).
- ³⁷W. Schill, “Variational and multiscale modeling of amorphous silica glass,” Ph.D. thesis (California Institute of Technology, June 2020).
- ³⁸X. Markenscoff, “Volume collapse instabilities in deep-focus earthquakes: a shear source nucleated and driven by pressure,” *Journal of the Mechanics and Physics of Solids*, 104379 (2021).
- ³⁹C. Meade and R. Jeanloz, “Effect of a coordination change on the strength of amorphous SiO₂,” *Science* **241**, Publisher: American Association for the Advancement of Science, 1072–1074 (1988).
- ⁴⁰J. K. Knowles and R. Abeyaratne, “Impact-Induced Transitions in Two-Phase Elastic Materials,” in *Evolution of Phase Transitions: A Continuum Theory* (Cambridge University Press, Cambridge, 2006), pp. 59–82.
- ⁴¹N. Bourne, J. Millett, and Z. Rosenberg, “On the origin of failure waves in glass,” *Journal of Applied Physics* **81**, Publisher: American Institute of Physics, 6670–6674 (1997).
- ⁴²C. Kettenbeil, “Dynamic Strength of Silica Glasses at High Pressures and Strain Rates,” Ph.D. thesis (California Institute of Technology, 2019).

- ⁴³O. T. Strand, D. R. Goosman, C. Martinez, T. L. Whitworth, and W. W. Kuhlow, “Compact system for high-speed velocimetry using heterodyne techniques,” *Review of Scientific Instruments* **77**, Publisher: American Institute of Physics, 083108 (2006).
- ⁴⁴B. J. Jensen, D. B. Holtkamp, P. A. Rigg, and D. H. Dolan, “Accuracy limits and window corrections for photon Doppler velocimetry,” *Journal of Applied Physics* **101**, Publisher: American Institute of Physics, 013523 (2007).
- ⁴⁵D. H. Dolan, “Accuracy and precision in photonic Doppler velocimetry,” *Review of Scientific Instruments* **81**, Publisher: American Institute of Physics, 053905 (2010).
- ⁴⁶L. S. T. Corp., *LS-DYNA | Livermore Software Technology Corp.* Feb. 2021.
- ⁴⁷C. S. Alexander, L. C. Chhabildas, W. D. Reinhart, and D. W. Templeton, “Changes to the shock response of fused quartz due to glass modification,” *International Journal of Impact Engineering, Hypervelocity Impact Proceedings of the 2007 Symposium* **35**, 1376–1385 (2008).
- ⁴⁸D. E. Grady and L. C. Chhabildas, “Shock-wave properties of soda-lime glass,” English, in Iyer K.R. and Chou S.C. (eds) *Proceedings of the 14th U.S. Army Symposium on solid mechanics* (Nov. 1996).
- ⁴⁹S. Ravindran, V. Gandhi, Z. Lovinger, M. Mello, and G. Ravichandran, “Dynamic strength of copper at high pressures using pressure shear plate experiments,” *Journal of Dynamic Behavior of Materials*, **10**. 1007/s40870-020-00287-z (2021).
- ⁵⁰R. J. Clifton and T. Jiao, “Testing, Experiments and Properties of HSREP,” in *Elastomeric Polymers with High Rate Sensitivity*, edited by R. G. Barsoum (Elsevier, 2015), pp. 28, 31.
- ⁵¹A. Ginzburg and Z. Rosenberg, “Using reverberation techniques to study the properties of shock loaded soda-lime glass,” *AIP Conference Proceedings* **429**, Publisher: American Institute of Physics AIP, 529 (2008).
- ⁵²D. P. Dandekar, “Index of refraction and mechanical behavior of soda-lime glass under shock and release wave propagations,” *Journal of Applied Physics* **84**, Publisher: American Institute of Physics, 6614–6622 (1998).
- ⁵³D. P. Dandekar, “Shock, release, and tension response of soda-lime glass,” *AIP Conference Proceedings* **429**, Publisher: American Institute of Physics, 525–528 (1998).
- ⁵⁴D. E. Grady, “The spall strength of condensed matter,” *Journal of the Mechanics and Physics of Solids* **36**, 353–384 (1988).
- ⁵⁵D. Schmitt, B. Svendsen, and T. J. Ahrens, “Shock Induced Radiation from Minerals,” in *Shock Waves in Condensed Matter*, edited by Y. M. Gupta (Springer US, Boston, MA, 1986), pp. 261–265.

- ⁵⁶Z. Burghard, A. Zimmermann, J. Rödel, F. Aldinger, and B. R. Lawn, “Crack opening profiles of indentation cracks in normal and anomalous glasses,” *Acta Materialia* **52**, 293–297 (2004).

*Chapter 3***SHOCK COMPRESSION AND RELEASE STUDY TO PROBE
PHASE TRANSITION IN SODA-LIME GLASS****3.1 Introduction**

There have been many shock compression studies in the past to estimate the Hugoniot Elastic Limit (HEL) of SLG [1–5]. Finding the HEL of SLG is non-trivial, mainly due to the concave-down nature of its compression stress-strain response. The concave-down loading velocimetry profiles observed in plate impact experiments on SLG do not reveal a clear elastic-inelastic transition. A novel approach adopted in [2] estimated the HEL of SLG to be approximately 7.5 GPa. This was done by identifying the onset of hysteresis in the loading and unloading stress-strain profiles. A similar approach was adopted in [1], wherein the impact stress at which the compression wave-speed differed from release wave-speed was estimated to be the HEL of SLG. The point at which the two wave speeds differ coincides with the onset of inelasticity, wherein the slopes of the compression and release paths in stress-strain curves are different. The HEL was thus estimated to be 3.1 GPa in that work. Despite the use of similar principles, the difference in HEL estimates between the two aforementioned works might be due to the use of midpoint of the release-fan to measure the release wave-speed in the latter work, rather than use of the initial release wave-speed. Various other techniques to measure the HEL of SLG provide similar estimates between 4-6 GPa [4–6].

This stress range of 4-6 GPa corresponds to the threshold stress for the onset of the failure wave phenomenon [1, 7, 8]. The SLG is observed to undergo a complete and sudden loss of spall strength behind a failure-front that travels significantly slower than the compression wave. As discussed in the previous chapter, this failure wave phenomenon is also found to carry a significant densification similar to what would be expected of a phase-transition. Silicon dioxide, which forms a major constituent of SLG and other silica glasses, has many crystalline polymorphs such as α -quartz, coesite, and stishovite, all of which are denser than amorphous silica. The temperature-pressure phase diagram for SiO_2 [9] indicates that α -quartz and coesite are the thermodynamically favored crystalline structures for SiO_2 for pressures of 4-6 GPa. The α -quartz to coesite phase transition is known to be

kinetically hindered and slow [10]. Crystallization of the α -quartz phase, from amorphous silica, were not observed in previous shock compression experiments [11, 12], presumably because this transition is kinetically hindered at temperatures achieved in these experiments. However, laser-driven compression experiments on amorphous silica [11] seem to indicate onset of transition from the amorphous phase to the stishovite phase at stresses of 4.7 GPa. Another recent work involving quasistatic compression of SLG nanopillars [13] also indicates the possibility of SLG transforming to a stiffer stishovite phase at stresses of around 5 GPa. Past quasi-static compression experiments [14] and molecular simulation studies [15] on amorphous SiO_2 also indicate the presence of an ice-like first-order transition from low density amorphous phase to high density amorphous phase at pressures of 3.6 GPa. Studying the loading-unloading behavior of SLG subjected to shock compression to these stresses can provide significant insights into the existence and kinetics of a possible phase transition in the material at these aforementioned stresses.

Previous shock compression and release experiments to study the loading-unloading behavior of SLG [16] observed a progressively stiff release response with higher impact stresses. A similar stiffening of release was observed in the case of fused quartz [17], which could be due to a gradual irreversible transformation to a stiffer phase. However, as will be discussed later, this stiffening of release can also be attributed to regular elastic release behavior. Therefore a more careful analysis of the release behavior of SLG will be necessary to unequivocally establish the existence of a phase transition in SLG at relatively low impact stresses (4-7 GPa) under shock compression. Also, complete unloading of SLG was not achieved in the previous shock compression study [2]. This complete unloading of stress can provide insights into the existence of reverse phase transition and permanent densification in the material.

Permanent densification of SLG under shock compression can be indicative of its inelastic behavior or an irreversible phase transition or a combination of both. Such permanent densification was observed in SLG shock compressed to stresses above 4 GPa in past works which employed embedded strain-gauges [4] or which used changes in refractive index to infer densification in SLG [18]. Thus, the current work presents shock compression and release experiments on SLG to construct the loading and complete unloading response of the material. Also, inferences drawn from the experimental results from this study and previous studies are used to model

the general release behavior of SLG, for which a robust and satisfactory model is not presently available.

3.2 Materials and methods

The normal plate impact experiments conducted in this work used tungsten carbide (WC) and soda-lime glass (SLG) disks impacting SLG disk targets as shown in Fig. 3.1. The SLG disks were sourced from University Wafers, Inc., South Boston, MA and had densities of $2,480 \pm 10 \text{ kg/m}^3$. The target SLG disks were 5 mm thick and 30 mm in diameter, while the impactor SLG disk was 3 mm thick and 30 mm in diameter. Both had an average surface roughness of less than 1 nm. Aluminum rings were glued to the disks as shown in Fig. 3.1 to facilitate trigger upon impact. A $0.5 \mu\text{m}$ thin Aluminum layer was also deposited on the rear surface of the SLG target to provide a reflective coating for velocimetry measurements. The WC impactor was of BC-00 grade and sourced from Basic Carbide Corporation, Lowber, PA. They had a density of $15,480 \pm 100 \text{ kg/m}^3$. The WC disk was 2 mm thick and 34 mm in diameter. Lithium Fluoride crystal (LiF[100]) disks were used as windows in these experiments. These disks were 25.4 mm in diameter, $6.32 \pm 0.01 \text{ mm}$ in thickness, and were sourced from ASPHERA Inc., Santa Cruz, CA. The LiF crystals had densities of $2,640 \text{ kg/m}^3$ and less than 0.2° misalignment between the $\langle 100 \rangle$ crystal axis and the disk axis. No Anti-Reflective coating was deposited on the LiF disks as Fresnel reflections from the rear surface of the LiF window do not interfere significantly with Photon Doppler Velocimetry (PDV) measurements [19].

The velocity-time profile of the SLG-LiF[100] interface was obtained using PDV [20], which employs a 1,550 nm wavelength light to probe the interface. Due to the presence of the LiF[100] window, appropriate optical and impedance mismatch corrections will have to be applied to the observed velocity profile to obtain the in-material particle velocity. This procedure is outlined in Appendix B. Furthermore, the in-material velocity profile thus obtained is used to construct the stress-strain loading history of the SLG target. The following differential equations are integrated to achieve this [21, 22]:

$$d\varepsilon = \frac{du}{C_h(u)} \quad (3.1)$$

$$d\sigma = \rho_0 C_h(u) du \quad (3.2)$$

where $C_h(u)$ is the wave-speed in material frame and u is the particle velocity in the target material, which is initially at rest. $C_h(u)$ and u are obtained from

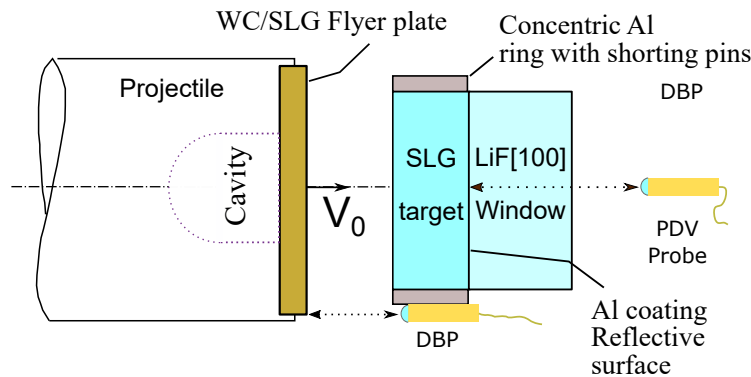


Figure 3.1: Schematic of plate impact experiment used to observe the shock compression and release behavior of SLG using Photon Doppler Velocimetry (PDV). The Down-Barrel Probe (DBP) measures the velocity of the impactor. The presence of the LiF[100] window ensures that the SLG material remains under compression as the PDV probe records the SLG-LiF interface velocity. A $0.5 \mu\text{m}$ thick aluminum (Al) coating provides a reflective surface for PDV measurement. The cavity behind the impactor ensures that the stress releases to zero at the rear-surface of the impactor.

| Expt. # | Impactor | Impactor thickness (mm) | Impact velocity (m/s) | Target thickness (mm) | Peak interface velocity (m/s) (optically corrected) | Peak in-material velocity (m/s) | Peak stress (GPa) |
|---------|----------|-------------------------|-----------------------|-----------------------|---|---------------------------------|-------------------|
| WSL-1 | WC | 2 | N/A | 5 | 411.5 ± 0.51 | 424.1 | 5.68 ± 0.26 |
| SSL-2 | SLG | 3 | 1266.1 ± 2.40 | 5 | 523.3 ± 0.03 | 577.3 | 7.27 ± 0.25 |

Table 3.1: Summary of experimental results

the in-material particle velocity data, which in turn is obtained from processing the velocimetry data as outlined in Appendix B. The only significant source of uncertainty in the computed stress-strain profile is the tilt in impact/ time of trigger, which is illustrated in Fig. 3.2. It should be noted that when impactors other than SLG are used (such as WC), one must account for the multiple reverberations in the impactor plate.

3.3 Results and discussion

Experiment #WSL-1

Experiment #WSL-1 involved impacting a 2 mm thick WC disk onto a 5 mm thick SLG disk target. Since the timings of reverberations of the stress-waves in the WC impactor was accurately observed by velocimetry of the WC-SLG interface in experiment #AJ-2 (see Chapter 2), the impactor thickness and velocity were chosen to replicate that experiment. These reverberation timings were then used

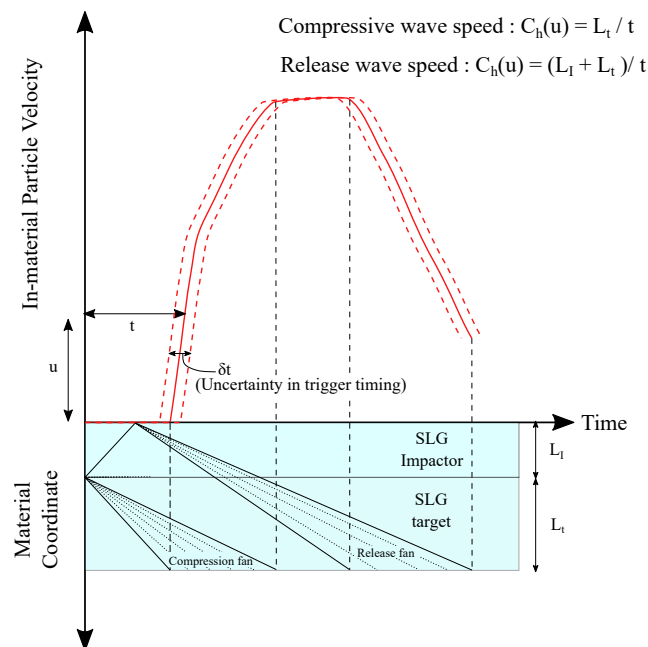


Figure 3.2: Schematic of procedure to evaluate the wave speed in material frame, $C_h(u)$.

to determine the speeds of the release waves arriving at the SLG-LiF interface. A plot of the observed and optically corrected interface velocity alongside a material position-time diagram is shown in Fig. 3.3. The measured interface velocity can be seen to consist of high frequency oscillations, which become more pronounced after the first and second unloadings. This noise can be attributed to a reduction in the intensity of the light reflected back to the PDV, and will have to be excluded from the velocity measurements in order to accurately capture the stress-strain response of SLG. The optically corrected data was thus smoothed, by interpolation, to remove these oscillations while retaining the important features in the data such as the two-wave structures of the first and second release. The smoothed data is then used to construct the stress-strain curve as discussed in Section 2.2. The stress-strain curve for this experiment, constructed using the procedure outlined in Section 3.2, is shown in Fig. 3.4. The dashed lines represent the bounds in uncertainty due to uncertainty in trigger-timing of around 40 ns. The peak compressive stress is observed to be 5.68 GPa, after which the unloading is observed to occur in multiple steps, each effected by the reverberation of the release waves in the WC impactor.

A significant observation is that the loading and unloading paths do not coincide. The unloading occurs only partially, up to a stress of around 2.8 GPa, due to the

use of an impactor with impedance higher than the SLG target. However, the second unloading can be seen to proceed parallel to the loading curve. It can thus be assumed that a complete unloading would have resulted in a permanent densification in the material. It is very unlikely that this small hysteresis is due to onset of inelasticity in the material, as a small hysteresis would imply a small yield strength for the material at these stresses, which would further entail an unlikely and abrupt increase in pressure due to reduced deviatoric stresses. As will be discussed later, this observed hysteresis in the stress-strain curve is more likely due to a hysteresis in the pressure loading and unloading effected by a gradual phase-transition occurring in the material. The pressure-strain curve shown in Fig. 3.4 is obtained by subtracting the elastic deviatoric stress from the longitudinal stress using a constant shear modulus of 30.5 GPa for SLG.

The impact velocity could not be measured in this experiment due to lack of light reflected back to the Down-Barrel Probe. Although this impact velocity was not necessary to construct the stress-strain curve for the experiment, a consequence of not knowing the impact velocity is that the existence and extent of densification due to the failure wave, expected in SLG at these stresses, cannot be estimated. As was shown in Chapter 2, the densification due to the failure wave is associated with a difference between the observed and expected peak velocity. Without knowledge of the impact velocity, the expected peak velocity and hence the deficit in velocity cannot be estimated. The targeted velocity for the experiment was 520 m/s. As will be discussed later, finite element analysis simulations of this experiment using ABAQUS Explicit were able to match the observed peak-velocity (optically corrected) by considering an impact velocity of 490 m/s.

Additionally, due to reflections from the rear surface of the LiF window, the PDV probe was able to record the velocity-time history of the rear-surface of LiF as well. Velocity measurements of the LiF free surface indicate a spall occurring in the LiF material, which could be a possible reason for the complete loss of signal from the SLG-LiF interface. The peak velocity for the LiF rear-surface can be seen to be approximately twice the optically corrected peak interface velocity, thus lending further credibility to the optical corrections applied to the observed interface velocity.

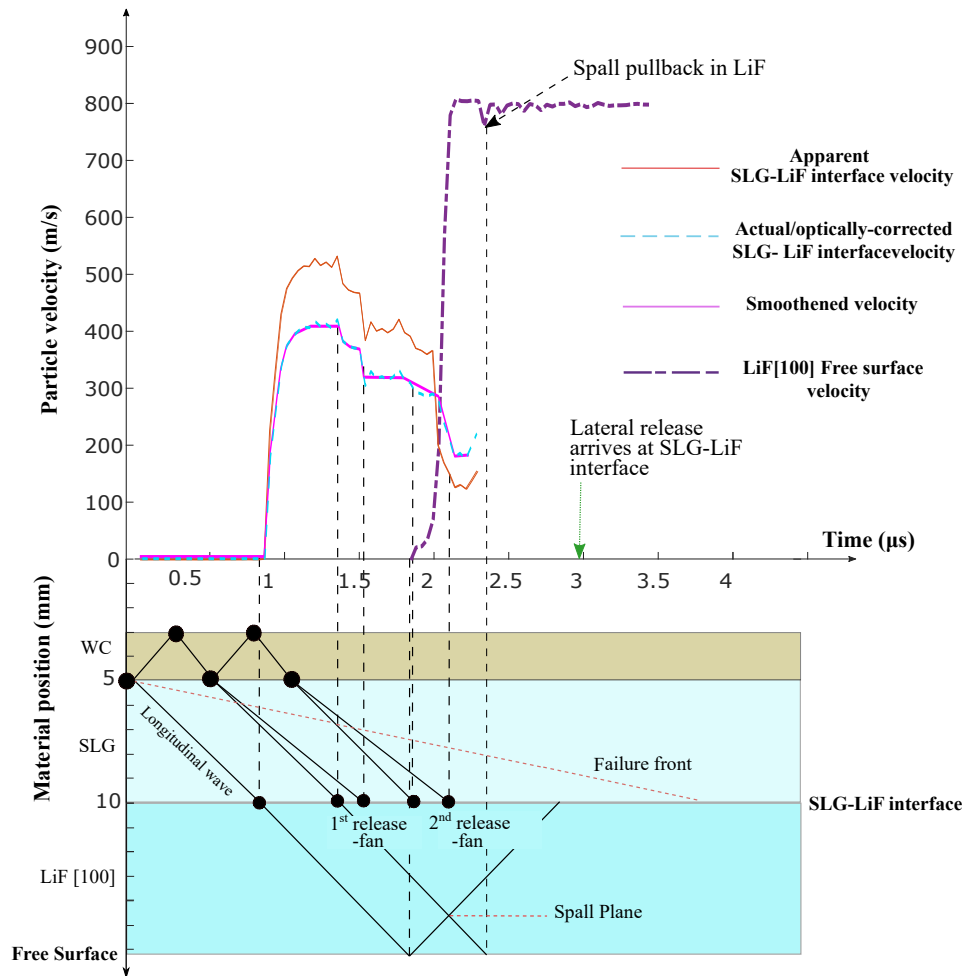


Figure 3.3: Velocimetry data from experiment WSL-1 for SLG-LiF interface and LiF free surface. A failure wave velocity of 1.3 km/s was assumed in the (X-t) diagram.

Experiment #SSL-2

Experiment #SSL-2 involved symmetric impact between a 3 mm thick SLG disk onto a 5 mm thick SLG disk target at an impact velocity of 1,266 m/s. A plot of the observed and optically corrected SLG-LiF interface velocity alongside a material position-time diagram is shown in Fig. 3.5. The optically corrected data is used to construct the stress-strain curves shown in Fig. 3.6. The dashed lines represent the bounds in uncertainty due to uncertainty in trigger timing of around 40 ns. The peak compressive stress is observed to be 7.27 GPa. It can also be observed that complete unloading of stress to 0 GPa is achieved in this experiment, with a major part of the unloading curve parallel to the loading curve. It is thus observed that SLG retains a permanent volumetric strain of around 2%, which is higher than the permanent strain observed in experiment WSL-1. As discussed later, this increasing

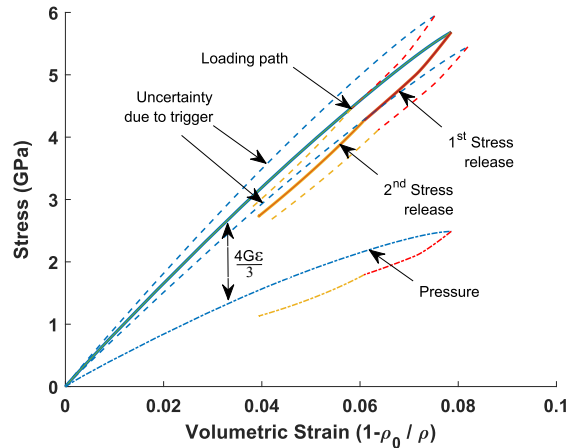


Figure 3.4: Stress-strain curve for SLG material in experiment WSL-1. The dashed lines indicate the bounds in uncertainty of stress-strain curve due to uncertainty in trigger timing. The pressure curve is inferred from the stress curve by subtracting the elastic deviatoric stress.

of permanent volumetric strain with increase in impact stress is a strong indicator of a gradual, irreversible phase transition occurring in SLG. The pressure-strain curves plotted in Fig. 3.6 were computed by subtracting the appropriate deviatoric stress from the stress-strain curve. The deviatoric stress was taken to be $\frac{4}{3}G\varepsilon$ for strains smaller than ε_{HEL} and $\frac{4}{3}G\varepsilon_{HEL}$ for strains higher than that.

The observed peak velocity for the LiF free surface can again be seen to be approximately twice the optically corrected peak value for the interface velocity, thus lending further credibility to the optical corrections applied to the observed data. A significant observation can be made in the SLG-LiF interface velocity data after it has been corrected for optical effects and impedance mismatch (see Fig. B.7). The resultant in-material particle velocity can be seen to have a peak value of 577.3 m/s. This is around 56 m/s lesser than 633 m/s, which would be the expected peak velocity for symmetric SLG-SLG impact. This deficit occurs due to a fast travelling release wave that arrives at the SLG-LiF interface at $1.5 \mu\text{s}$, thereby quenching/attenuating any compression wave that travels slower than 3.3 km/s. These slower travelling waves can be due to a regular plastic behavior in the SLG, which gives rise to a slower plastic shock-wave, or due to the failure wave travelling at 1.3 km/s (discussed in Chapter 2). Thus, depending on the speed of this second wave and the observed deficit in peak velocity, an additional 1.8% to 4.6% (see Eqn. A6 in Appendix A) of volume densification/strain will have to be considered in the stress-strain curve. For further illustrations and calculations in this work, the additional densification will

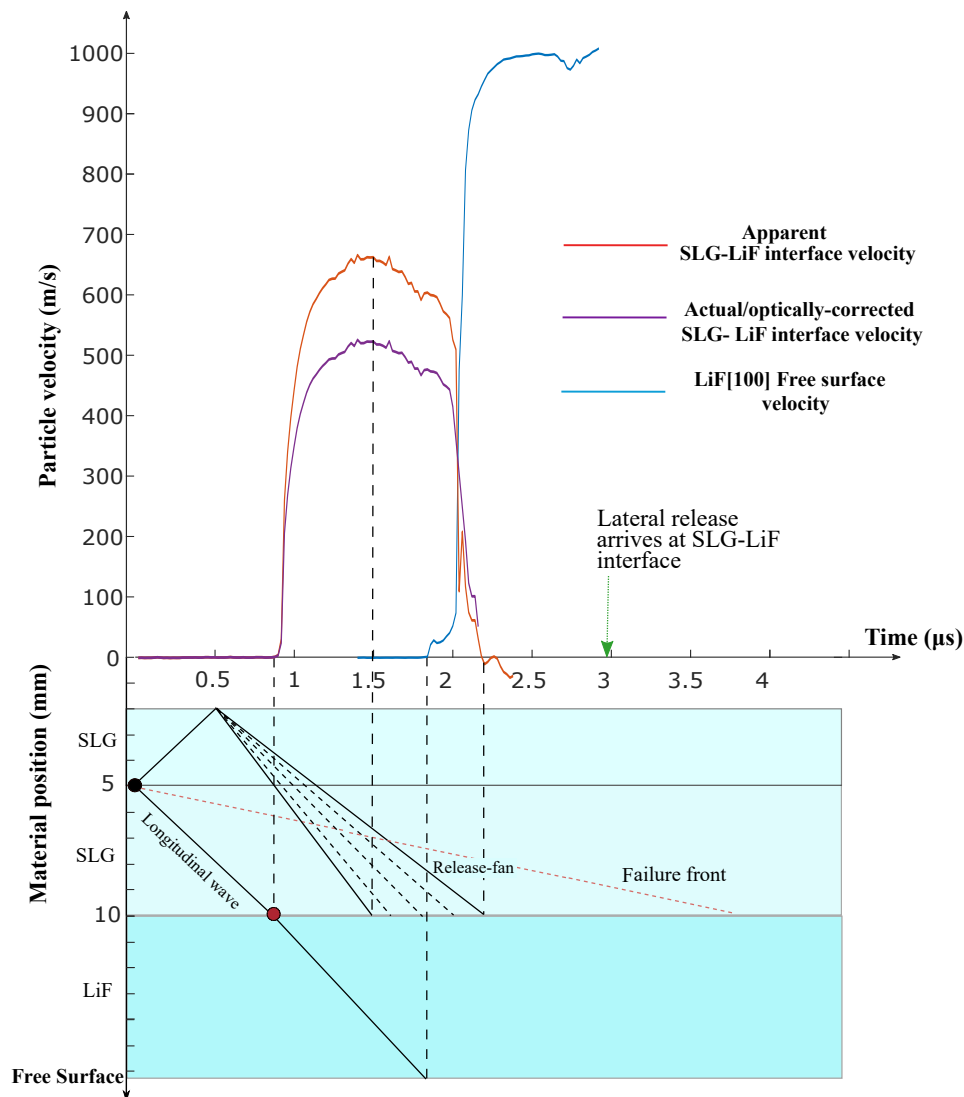


Figure 3.5: Velocimetry data of experiment #SSL-2 for SLG-LiF interface and LiF free surface. A failure wave velocity of 1.3 km/s was assumed in the (X-t) diagram.

be assumed to be 4.6% in magnitude and taken to be caused by the failure wave. The stress-strain curve incorporating this densification is also shown in Fig. 3.6b.

Role of initial elastic release and phase transition

Since, in general, plasticity is associated with the deviatoric stresses in the material, the pressure-volume equation of state (EOS) of the material can be assumed to be unaffected by inelastic behavior. Thus, under conditions of plastic yielding, the loading and unloading paths in the pressure-volume EOS can be assumed to be the same for a material. In contrast, a phase transition can be expected to alter the pressure-volume response of the material and give rise to a hysteresis in the

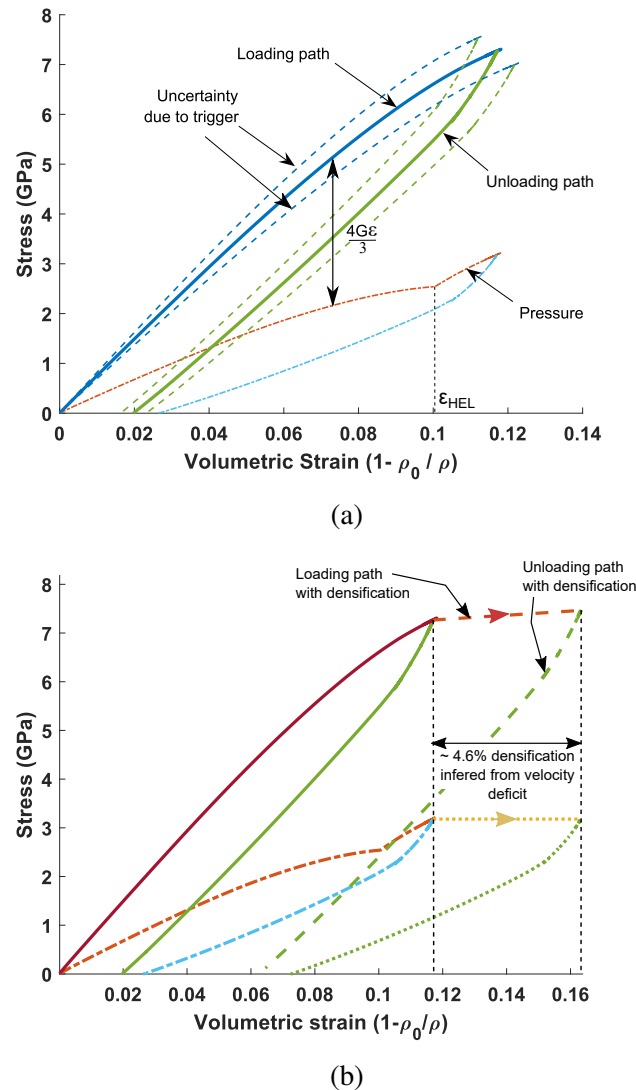
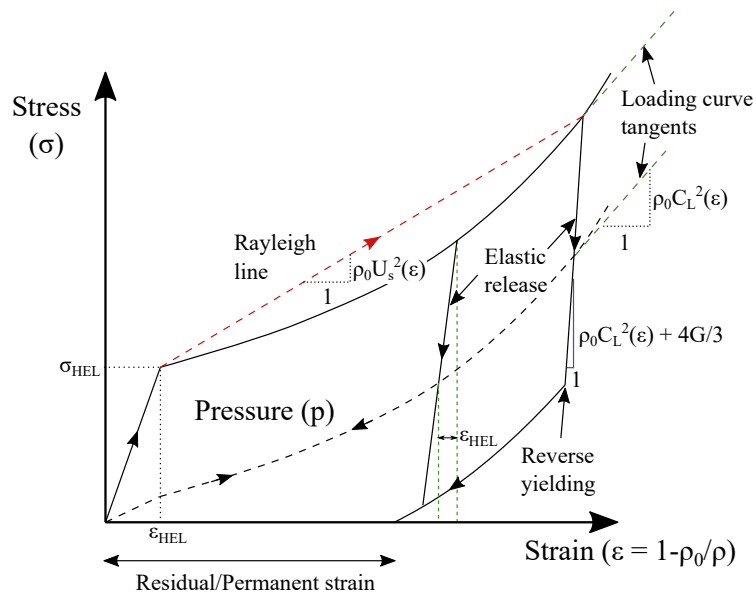
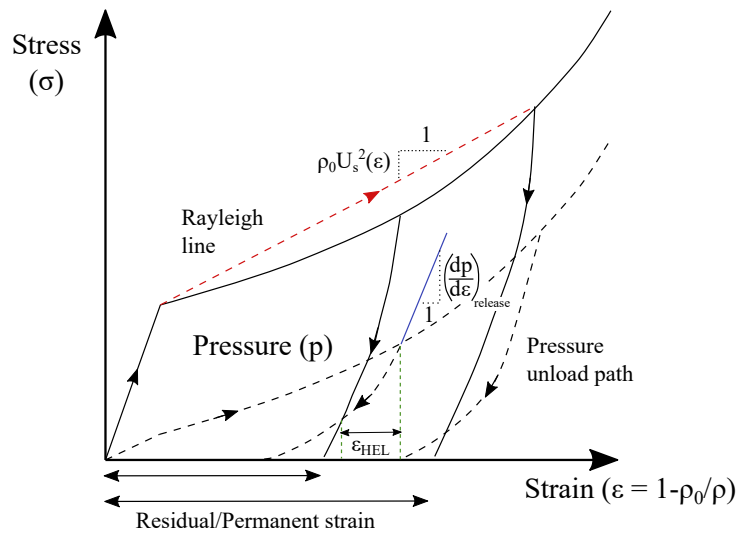


Figure 3.6: Stress-strain curve for SLG material inferred from experiment #SSL-2 (a) not accounting for additional compression due to the failure wave. (b) accounting for additional compression due to the failure wave. The dashed-lines indicate the bounds in uncertainty of stress-strain curve due to uncertainty in trigger timing (40 ns). The pressure curve is inferred from the stress curve by subtracting the elastic deviatoric stress.

pressure loading and unloading. Thus, a difference in loading and release paths in the pressure-volume EOS of the material would indicate a phase transition. A phase transition in the material can also be expected to cause permanent densification that increases with impact stress/peak compressive stress. The relationship between the initial release wave speed (C_R), shear-modulus as a function of strain ($G(\epsilon)$), and the longitudinal wave speed prior to release (C_L) is derived next.



(a.)



(b.)

Figure 3.7: Schematic stress-strain diagrams of shock-loading and release for materials with (a) Regular inelastic response and (b) Phase transition. For material with phase transition the mismatch in pressure loading and unloading paths can be observed. Additionally, materials with phase transition can be expected to undergo higher permanent strains for higher impact stresses. Both materials considered here are assumed to lack strain-hardening.

Under conditions of uniaxial strain, prevalent in plate-impact experiments, the longitudinal stress (σ), pressure (p), and the longitudinal/volumetric strain (ε) can be related as follows:

$$\sigma = \begin{cases} p + \frac{4G\varepsilon}{3} & \varepsilon \leq \varepsilon_{HEL} \\ p + \frac{2Y(\varepsilon)}{3} & \varepsilon > \varepsilon_{HEL} \end{cases}$$

where $Y(\varepsilon)$ is the yield (flow) strength as a function of strain. Further, under elastic longitudinal release,

$$\sigma(\varepsilon) = p(\varepsilon) + \frac{4G(\varepsilon)}{3}(\varepsilon - \varepsilon_{init} + \varepsilon_{HEL})$$

where ε_{init} is the maximum compressive strain attained before unloading starts, as shown in Fig. 3.7(a). Further, differentiating the above relationship gives,

$$\left(\frac{d\sigma}{d\varepsilon}(\varepsilon) \right)_{release} = \left(\frac{dp}{d\varepsilon}(\varepsilon) \right)_{release} + \frac{d}{d\varepsilon} \left(\frac{4G(\varepsilon)}{3}(\varepsilon - \varepsilon_{init} + \varepsilon_{HEL}) \right) \quad (3.3)$$

The above equation, when evaluated at $\varepsilon = \varepsilon_{init}$, gives the initial elastic release wave speed : $C_R^2(\varepsilon_{init}) = \frac{1}{\rho_0} \frac{d\sigma}{d\varepsilon}(\varepsilon_{init})$. In order to further simplify Eq. 3.3 to evaluate $C_R(\varepsilon_{init})$, the slope of the pressure-strain curve upon release will have to be evaluated. This is described next.

Assuming SLG to have regular elastic release

Referring to Fig. 3.7(a), it can be seen that for regular elastic release, the loading and unloading paths for pressure coincide. Thus, the slope of the pressure-strain curve upon release will be identical to the slope of the stress Hugoniot at ε_{init} . For $\varepsilon_{init} < \varepsilon_{HEL}$, the slope of the stress Hugoniot, and hence $\left(\frac{dp}{d\varepsilon}(\varepsilon) \right)_{release}$, is equal to $\rho_0 C_L^2(\varepsilon_{init})$. The value for the longitudinal compression wave speed ($C_L(\varepsilon_{init})$) as a function of strain can be inferred from Fig. 3.8, wherein only the compressive wave speeds before $\varepsilon_{init} = \varepsilon_{HEL}$ ($\varepsilon_{HEL} = 0.1$) correspond to C_L . The compressive wave-speeds after $\varepsilon_{init} = \varepsilon_{HEL}$ correspond to shock-wave speeds ($U_S(\varepsilon)$) and will have to be treated differently, as discussed next.

For $\varepsilon_{init} \geq \varepsilon_{HEL}$, the slope of the stress Hugoniot $\frac{d\sigma_h}{d\varepsilon}$ is evaluated by considering the equation for Hugoniot stresses (σ_h) higher than σ_{HEL} :

$$\begin{aligned} \sigma_h - \sigma_{HEL} &= \rho_0 U_S^2(\varepsilon)(\varepsilon - \varepsilon_{HEL}) \\ \implies \frac{d\sigma_h}{d\varepsilon} &= \rho_0 U_S^2(\varepsilon) + 2\rho_0 U_S(\varepsilon) \frac{dU_S}{d\varepsilon}(\varepsilon)(\varepsilon - \varepsilon_{HEL}) \end{aligned} \quad (3.4)$$

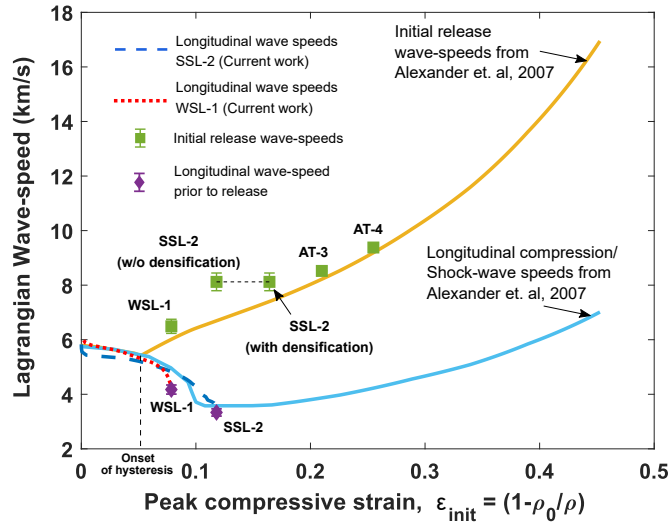


Figure 3.8: Plot of Lagrangian wave speeds of compression and release waves in SLG. The data for experiments AT-3 and AT-4 are taken from [16]. The compression and release wave speeds for SLG provided as a function of peak particle velocity in [2] was modified by converting particle velocity to strains (Eq. A.2 in Appendix A). The onset of hysteresis is the strain at which the release and compression wave-speeds start to differ significantly.

To evaluate $U_S(\varepsilon)$, the equation shown in Fig. A.1 of Appendix A can be used. The shock speed as function of particle velocity ($U_S(u_p)$) can be expressed as $U_S(\varepsilon)$ as follows (all velocities in km/s):

$$U_S(u_p) = 3.15 + 1.54(u_p - u_{pHEL})$$

Using $\varepsilon - \varepsilon_{HEL} = \frac{u_p - u_{pHEL}}{U_S(u_p)}$, the above equation can be re-expressed as:

$$U_S(\varepsilon) = \frac{3.15}{1 - 1.54(\varepsilon - \varepsilon_{HEL})} \quad (3.5)$$

$$\Rightarrow \frac{dU_S}{d\varepsilon} = \frac{4.851}{(1 - 1.54(\varepsilon - \varepsilon_{HEL}))^2} \quad (3.6)$$

Thus, Eq. 3.4 can be evaluated using Eqs. 3.6 and 3.5 (all pressures and stresses in GPa):

$$\frac{d\sigma_h}{d\varepsilon} = \rho_0 \left(\frac{3.15}{1 - 1.54(\varepsilon - \varepsilon_{HEL})} \right)^2 + 2\rho_0 \left(\frac{3.15}{1 - 1.54(\varepsilon - \varepsilon_{HEL})} \right) \left(\frac{4.851}{(1 - 1.54(\varepsilon - \varepsilon_{HEL}))^2} \right) (\varepsilon - \varepsilon_{HEL}) \quad (3.7)$$

In summary, for initial-release assuming simple elastic-inelastic behavior,

$$\left(\frac{dp}{d\varepsilon}(\varepsilon)\right)_{release} = \begin{cases} \rho_0 C_L^2(\varepsilon) - \frac{4}{3}G & \varepsilon \leq \varepsilon_{HEL} \\ Eq. 3.7 & \varepsilon > \varepsilon_{HEL} \end{cases} \quad (3.8)$$

Thus, Eq. 3.3, now simplifies to:

$$G'(\varepsilon_{init}) + \frac{1}{\varepsilon_{HEL}}G(\varepsilon_{init}) = \frac{3}{4\varepsilon_{HEL}} \left(\rho_0 C_R^2(\varepsilon_{init}) - \left(\frac{dp}{d\varepsilon}(\varepsilon_{init})\right)_{release} \right) \quad (3.9)$$

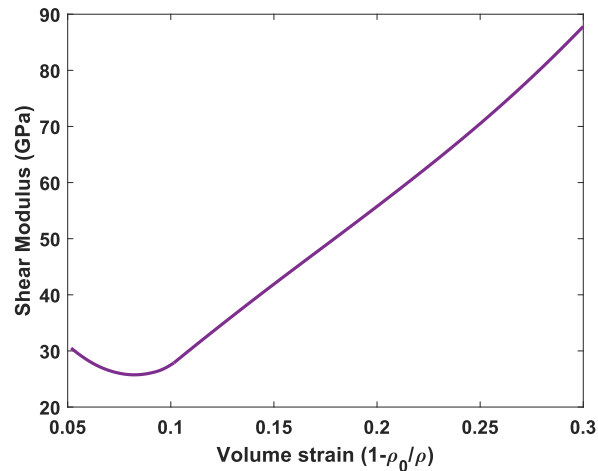
This first order linear differential equation can be solved to obtain shear modulus (G) as a function of volumetric strain $\varepsilon = 1 - \frac{\rho_0}{\rho}$, which is plotted in Fig. 3.9. In solving Eq. 3.9, it was assumed that the shear modulus remains constant (at 30.5 GPa) before the onset of hysteresis. The shear modulus cannot be computed using the aforementioned procedure when there is no mismatch between the compression and release wave speeds. This difference in wave speeds that occurs only after onset of hysteresis, as shown in Fig. 3.8, is a prerequisite to evaluating the shear modulus.

It can be observed in Fig. 3.9b, that the shear modulus of SLG computed as a solution to Eq. 3.9 is able to capture the anomalous behavior of shear modulus observed in other closely related materials such as fused quartz and fused silica. Notably, the shear modulus is observed to initially decrease with increase in pressure, and at a threshold pressure it starts increasing. The variation of shear modulus and the threshold pressure are accurately captured by the computed solution. However, it can be seen that the computed solution for shear modulus of SLG is always significantly higher than the experimentally observed values of other materials' shear modulus. Especially for pressures greater than 3 GPa, the computed value of G for SLG is more than 20 GPa higher than that predicted for fused silica by molecular dynamics (MD). Possible reasons and implications of this are discussed in the following section.

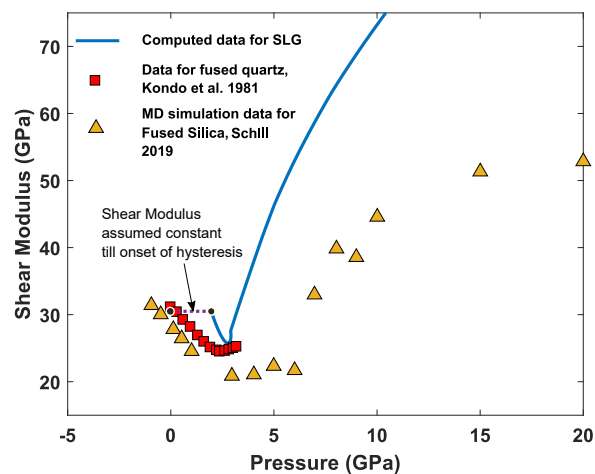
Phase-transition as cause for observed hysteresis in SLG

The main reason Eq.3.9 significantly overestimates the shear modulus of SLG could be the use of an underestimated value for $\left(\frac{dp}{d\varepsilon}(\varepsilon)\right)_{release}$.

As shown in Fig.3.7, in case of a simple elastic-inelastic transition, as was assumed to compute the shear modulus, the slope for the pressure-strain curve upon release is taken to be identical to the pressure-strain slope under compression. However, as



(a)



(b)

Figure 3.9: Estimates of shear modulus (a) Plot of computed shear modulus vs. volumetric strain for SLG as computed using Eq. 3.9. (b) Plot of shear modulus vs. pressure for SLG, by converting strains in previous plot to corresponding pressure in SLG (using EOS-1 described in Chapter 2). Data for SLG is plotted alongside data for fused quartz from [23] and MD simulations results from [24].

evidenced by the resultant overestimation of the shear modulus, it may be necessary to consider the release slope of the pressure-strain curve to be higher than the loading slope. As shown in Fig.3.7b, this would be the case if the material experiences a phase transition and resultant hysteresis in loading and unloading for the pressure.

Other techniques of measuring the shear modulus under shock compression would be necessary to unequivocally measure the shear modulus of SLG. Due to lack of reliable measurements of shear modulus in SLG as a function of pressure, a

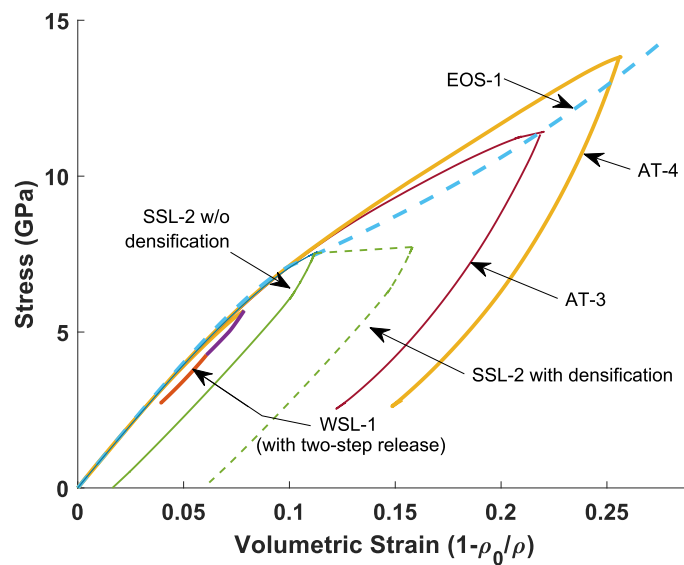
constant G was assumed for purposes of modeling and estimating the pressure from the observed stress.

Summary of experimental results

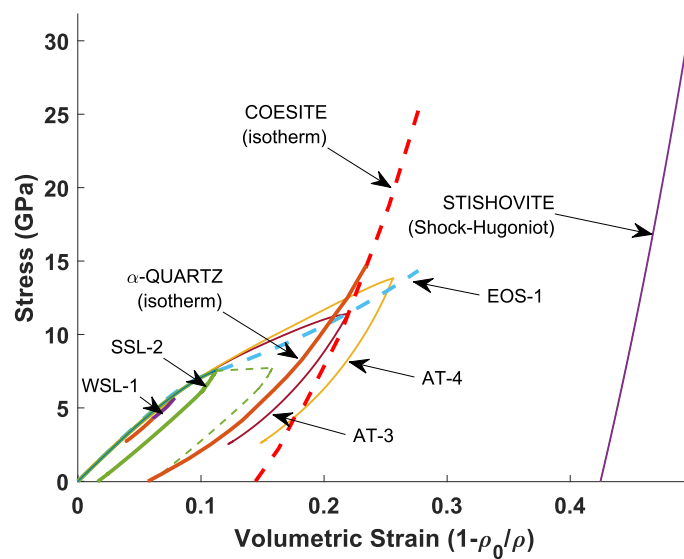
Figure 3.10(a) provides, in summary, a plot of SLG's observed stress-strain response in experiments WSL-1, SSL-2, AT-3, and AT-4. The interface-velocity data for experiments AT-3 and AT-4 were taken from [16], corrected for SLG-LiF impedance mismatch, and then processed to obtain the stress-strain curve shown in the plot. Experiments AT-3 and AT-4 were chosen for analysis here as they too used symmetric SLG-SLG plate impact with LiF[100] windows for shock compression and release of SLG. Both AT-3 and AT-4 used 6 mm thick SLG impactors and targets. Experiment AT-3 involved an impact velocity of 1.99 km/s, while experiment AT-4 involved an impact velocity of 2.38 km/s. The use of a SLG impactor makes the velocity data more reliable for the purpose of extracting the stress-strain response. It can be observed that the loading-unloading hysteresis and permanent densification starts in SLG at around 5-6 GPa of impact stress and continues to grow as the impact stress increases. As discussed earlier, this behavior is more consistent with occurrence of a gradual and irreversible phase transition in the material as opposed to a regular inelastic behavior. This onset of loading-unloading hysteresis can also be related to the failure-wave phenomenon which is observed to occur in SLG that is shock compressed to stresses between 4.7 GPa [1, 8] and 10.8 GPa (see Chapter 2). Figure 3.10(b) shows a plot of the observed stress-strain behavior of SLG alongside the stress hugoniot of stishovite, and pressure-isotherms of α -quartz and coesite. It can be noted that the unloading paths of SLG for experiments AT-3 and AT-4 closely resemble the pressure-isotherm for α -quartz. It was observed in [25] that under compression to stresses of around 110 GPa, the stress-strain response of SLG was very similar to that of the stishovite phase.

3.4 Modeling

The plate impact experiments are modeled using ABAQUS Explicit [28], a commercial finite element analysis software used to model dynamic events. The simulation uses a geometry shown schematically in Fig. 2.4, with 2-D plane-strain rectangular elements. After checking for convergence with mesh-refinement, each element length is chosen to be 10 μm thick along the X-axis (shock loading direction) and 100 μm wide along Y-axis [29]. Similar to what was described in Chapter 2, the materials are modeled using isotropic strain, strain-rate dependent hardening, and



(a)



(b)

Figure 3.10: Stress-strain response of SLG and other polymorphs of SiO_2 . (a) Stress-strain plots of symmetric shock-release experiments on SLG. (b) Alongside data in (a), stress or pressure vs. strain curves for high pressure polymorphs of SiO_2 : Pressure vs. strain isotherm for α -quartz, pressure vs. strain isotherm for coesite, Stress vs. strain Hugoniot for stishovite. SLG- LiF interface data for experiments AT-3 and AT-4 were taken from [16] and then processed to obtain the shown stress-strain plots for these experiments. EOS-1 is the equation of state for SLG used in chapter 2. Equations of state for α -quartz, coesite, and stishovite were taken from [26], [9] and [27], respectively.

| Density, ρ_0 (kg/m ³) | Shear Modulus, G (GPa) | Y_0 (GPa) | Equation of state parameters | | |
|---|--------------------------------|-------------|------------------------------|------|---------------------------------------|
| | | | C_0 (m/s) | S | Grüneisen Parameter (Γ_0) |
| 2640 | 32.3 | 0.286 | 5150 | 1.35 | 1.7 |

Table 3.2: Properties of LiF[100] used in the simulation. Equation of state properties were obtained from [31], where Grüneisen parameter (Γ_0) is assumed to be $(2S - 1)$.

J₂ plasticity, with yield (flow) strength (Y) given by:

$$Y(\varepsilon_p, \dot{\varepsilon}_p) = (Y_0 + B\varepsilon_p^n) \left(1 + \left(\frac{\dot{\varepsilon}_p}{C\dot{\varepsilon}_{p0}} \right)^{\frac{1}{p}} \right) \quad (3.10)$$

The equation of state (EOS) and material properties used for WC are provided in Table 2.3 of Chapter 2. The LiF[100] window is modeled using the linear EOS, $U_s = C_0 + Su_p$, with parameters shown in Table 3.2. The shear modulus (G_0) for LiF is computed using a Poisson's ratio of 0.3 [30] and a bulk modulus (K_0) of 70 GPa, which is assumed to be constant for the range of stresses simulated in this work. The bulk modulus was computed using the relation $K_0 = \rho_0 C_0^2$ and $C_0 = 5.15$ km/s [31]. The yield strength of LiF[100] was inferred from its HEL (0.5 GPa) provided in [32]. Owing to the small yield strength of LiF[100], all hardening effects in the material are ignored for the range of stresses encountered in this work. The properties used for LiF[100] are summarized in Table 3.2.

The equation of state and strength parameters used for SLG were similar to what was discussed in the previous chapter. The only difference was that the strain hardening parameter B (see Table 2.2) was set to zero for SLG in the current VUMAT implementation. As before, the relevant deviatoric stresses were subtracted from EOS-1 to determine the increments in pressure as a function of volumetric compression. Since the shear modulus (G) is assumed to be constant in the current implementation, the hysteresis observed in the stress-strain plot (Fig. 3.10) is shown to be captured by incorporating a hysteresis in the pressure. The method for specifying the path of decrease in pressure as function of volumetric strain is described next.

Figure 3.11 shows a plot of the evolution of Lagrangian release wave speeds as a function of volumetric strain for the different experiments analyzed in this work. For each of the experiments, the observed initial release wave speed is in good agreement with the best-fit curve provided in [2] as shown in Fig. 3.8 as well. After the initial release, the release wave speed first undergoes a steep decrease and eventually starts to decrease gradually with volumetric strain. This is similar

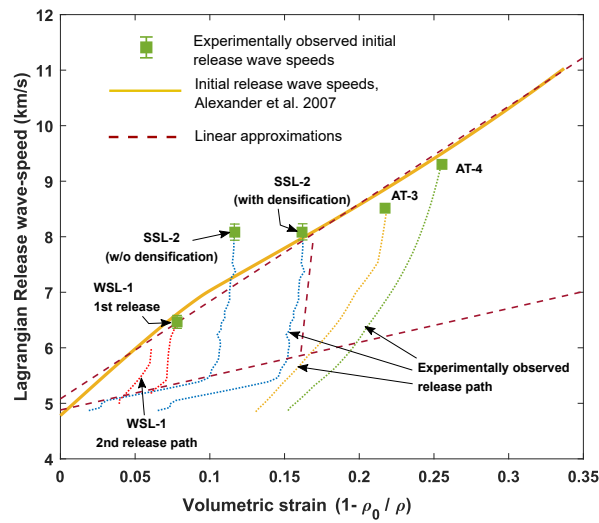
to the behavior of LiF[100] observed in [30, 33], wherein the release wave speed underwent a steep reduction in the “quasi-elastic” section and transitioned to a more gradual “plastic/bulk” behavior. The length of the quasi-elastic segment was used to estimate the strength of LiF[100] in [30], with a smaller quasi-elastic segment corresponding to a smaller strength. Also, in the aforementioned works on LiF[100], it can be noticed that for plastic behavior (gradual reduction), the release wave speeds were almost identical to the longitudinal compressive wave speeds. However, in the case of SLG, as observed in Figs. 3.8 and 3.11, the gradual release segment had release wave speeds significantly higher than the longitudinal compressive wave-speeds. This is another indicator that SLG does not undergo a simple elastic-inelastic transition and an additional phenomenon of phase transition to a stiffer phase will have to be considered to explain the observed behavior.

The release wave speeds observed in Fig. 3.11 can be related to the derivative of stress as a function of strain: $\left(\frac{d\sigma}{d\varepsilon}\right)_{release} = C_R^2(\varepsilon)$. The derivative for pressure under release: $\left(\frac{dp}{d\varepsilon}\right)_{release}$ is obtained by subtracting the appropriate deviatoric term from the stress derivative. As seen in Figs. 3.4 and 3.6, upon release the deviatoric stress (absolute difference between pressure and stress) never exceed the prescribed yield strength of SLG of 6.1 GPa. Thus, reverse yielding or yielding under release can be neglected for the range of stresses encountered in these experiments. Thus, for peak compressive strains (ε_{init}) greater than the threshold for onset of hysteresis (see Fig. 3.8), the pressure release is prescribed using Fig. 3.11b as follows:

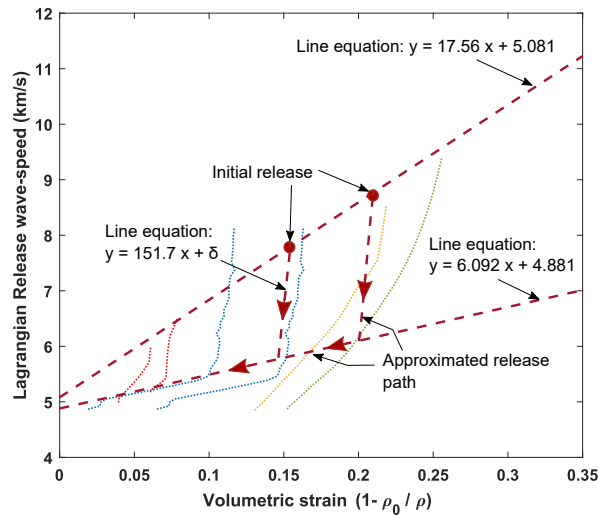
$$\left(\frac{dp}{d\varepsilon}\right)_{release} = \max \begin{cases} \rho_0(151.7\varepsilon + \delta)^2 - \frac{4}{3}G \\ \rho_0(6.092\varepsilon + 4.88)^2 - \frac{4}{3}G \end{cases} \quad (3.11)$$

where $\delta = (17.56 - 151.7)\varepsilon_{init} + 5.081$ is dependent on the peak compressive strain. The unit for density in the above equation is g/cc, for δ is km/s, and for the pressure-derivative and shear modulus is GPa.

The release path prescribed in Eq. 3.11 alongside the loading path prescribed by EOS-1 and regular J_2 plasticity is implemented using ABAQUS VUMAT for the SLG material. Results for the simulation are shown in Fig. 3.12, plotted alongside the optically corrected SLG-LiF interface velocity.



(a)



(b)

Figure 3.11: Plots of experimentally observed evolution of release wave-speeds under release compared with approximate linear estimates of the same used in modelling. (a) Plot of Lagrangian release wave speed evolution with strain observed in experiments. The initial release wave speed plot is the same as in Fig. 3.8 and is taken from [2]. The data for release paths for experiments AT-3 and AT-4 are taken from [16]. (b) Plot of approximate estimations of the release path for different peak compressive strains. This is used to model the evolution of release wave speed with strain in SLG. The δ in the equation for the high-slope release path denotes a variable intercept depending on the peak/initial-release strain.

Discussion

An impact velocity of 490 m/s was assumed for the WC impactor in this simulation. It can be observed that the simulated SLG-LiF interface velocity profile adequately

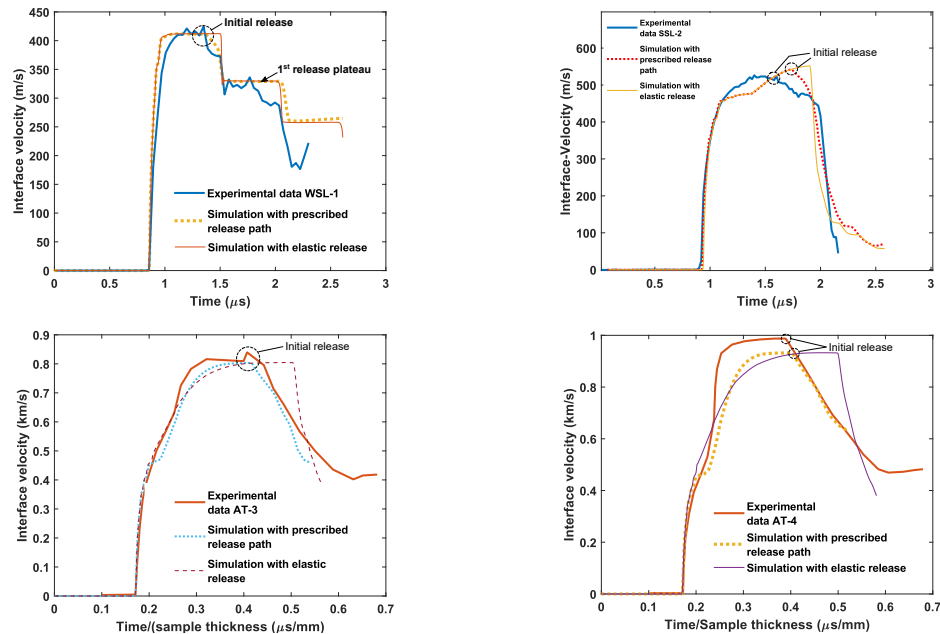


Figure 3.12: Comparison of experimentally measured interface velocity (optically corrected) and simulation results. Data for experiments AT-3 and AT-4 were taken from [16], and were digitized using [34]. Results from two types of simulations are shown for each experiment. One set of simulations assume a regular elastic unloading, and the other set of simulations involve a release path prescribed using Eq. 3.11.

captures the peak velocity and the first release plateau. The timing of the initial release and a two-wave structure in the first release is also captured. However, the second velocity plateau is significantly overestimated by the simulations. The simulations also do not capture a two-wave structure that seems to be present in the second release as well. This could be due to a complicated second-release behavior of SLG not accounted for in modeling the release or due to inadequate optical corrections in the experimental data after arrival of the shock-wave at the LiF free surface. Knowledge of the actual impact velocity, which was not observed due to lack of light return to the Down-Barrel probe would have been useful to infer the existence and extent of a sudden densification due to the failure wave in SLG. This could have then been used to adapt EOS-1 to better capture the observed response.

It can be observed that the simulations adequately capture the peak velocity observed experimentally. Although the initial release wave speed is underestimated by the simulations, the timing and extent of release in the later part of the release fan is well captured.

The experimentally observed peak velocity and initial release wave speed are adequately captured by the simulation. The later part of the unloading/release path is also closely replicated by the simulation. The simulations for experiment AT-4 adequately capture the initial release wave speed and the subsequent unloading behavior of SLG. However, the peak velocity seems to be underestimated by the model. This could be because, as seen in Fig. 3.10, the EOS-1 curve used to model the compression response of SLG slightly underestimates the peak stress for experiment AT-4.

3.5 Conclusion

In summary, experiments have been performed to study the release behavior of SLG at 5.7 and 7.3 GPa impact stresses. Permanent densification and loading-unloading hysteresis, which was observed in both experiments, was seen to increase with impact stress. Further, a theoretical evaluation of the shear modulus of SLG using data from these experiments and other related experiments in open literature yielded results that strongly indicate the occurrence of a gradual, irreversible phase transition in SLG to a stiffer phase. This phase-transition, which seems to start at around 5 GPa of impact stress could also play an important role in the failure wave phenomenon observed in SLG shock-compressed to these stresses. Lastly, based on the observed release wave speeds in SLG, a constitutive model to capture the release behavior of SLG subject to shock-compression was also proposed and evaluated.

References

- ¹D. Dandekar and P. Beaulieu, "Failure wave under shock wave compression in soda-lime glass," *Metallurgical and Material Applications of Shock-Wave and High-Strain-Rate Phenomena*, 211–218 (1995).
- ²C. S. Alexander, L. C. Chhabildas, and D. W. Templeton, "The Hugoniot elastic limit of soda-lime glass," *AIP Conference Proceedings* **955**, Publisher: American Institute of Physics, 733–738 (2007).
- ³C. H. M. Simha and Y. M. Gupta, "Time-dependent inelastic deformation of shocked soda-lime glass," *Journal of Applied Physics* **96**, Publisher: American Institute of Physics, 1880–1890 (2004).
- ⁴N. K. Bourne and Z. Rosenberg, "The dynamic response of soda-lime glass," *AIP Conference Proceedings* **370**, Publisher: American Institute of Physics, 567–572 (1996).

- ⁵Z. Rosenberg, Y. Ashuach, E. Dekel, and E. Bar-On, “The split-target technique for measurements of strength under high shock pressures,” *Measurement Science and Technology* **19**, Publisher: IOP Publishing, 045706 (2008).
- ⁶Z. Rosenberg, D. Yaziv, and S. Bless, “Spall strength of shock-loaded glass,” *Journal of Applied Physics* **58**, Publisher: American Institute of Physics, 3249–3251 (1985).
- ⁷N. S. Brar, S. J. Bless, and Z. Rosenberg, “Impact-induced failure waves in glass bars and plates,” *Applied Physics Letters* **59**, Publisher: American Institute of Physics, 3396–3398 (1991).
- ⁸R. J. Clifton, M. Mello, and N. S. Brar, “Effect of shear on failure waves in soda lime glass,” *AIP Conference Proceedings* **429**, Publisher: American Institute of PhysicsAIP, 521 (1998).
- ⁹R. J. Hemley, A. P. Jephcoat, H. K. Mao, L. C. Ming, and M. H. Manghnani, “Pressure-induced amorphization of crystalline silica”, en, *Nature* **334**, Number: 6177 Publisher: Nature Publishing Group, 52–54 (1988).
- ¹⁰J. Wackerle, “Shock-Wave Compression of Quartz”, *Journal of Applied Physics* **33**, Publisher: American Institute of Physics, 922–937 (1962).
- ¹¹A. E. Gleason, C. A. Bolme, H. J. Lee, B. Nagler, E. Galtier, D. Milathianaki, J. Hawreliak, R. G. Kraus, J. H. Eggert, D. E. Fratanduono, G. W. Collins, R. Sandberg, W. Yang, and W. L. Mao, “Ultrafast visualization of crystallization and grain growth in shock-compressed SiO₂,” *Nature Communications* **6**, Number: 1 Publisher: Nature Publishing Group, 8191 (2015).
- ¹²S. J. Tracy, S. J. Turneure, and T. S. Duffy, “In situ x-ray diffraction of shock-compressed fused silica,” *Physical Review Letters* **120**, Publisher: American Physical Society, 135702 (2018).
- ¹³M. Pozuelo, J. Lefebvre, P. Srivastava, and V. Gupta, “Stishovite formation at very low pressures in soda-lime glass,” *Scripta Materialia* **171**, 6–9 (2019).
- ¹⁴G. D. Mukherjee, S. N. Vaidya, and V. Sugandhi, “Direct observation of amorphous to amorphous apparently first-order phase transition in fused quartz,” *Physical Review Letters* **87**, Publisher: American Physical Society, 195501 (2001).
- ¹⁵D. J. Lacks, “First-order amorphous-amorphous transformation in silica,” *Physical Review Letters* **84**, Publisher: American Physical Society, 4629–4632 (2000).
- ¹⁶C. S. Alexander, L. C. Chhabildas, W. D. Reinhart, and D. W. Templeton, “Changes to the shock response of fused quartz due to glass modification,” *International Journal of Impact Engineering, Hypervelocity Impact Proceedings of the 2007 Symposium* **35**, 1376–1385 (2008).
- ¹⁷L. C. Chhabildas and D. E. Grady, “Chapter IV : 6 - Shock loading behavior of fused quartz,” in *Shock Waves in Condensed Matter 1983*, edited by J. R. Asay, R. A. Graham, and G. K. Straub (Elsevier, Amsterdam, Jan. 1984), pp. 175–178.

- ¹⁸R. V. Gibbons and A. T. J., “Shock metamorphism of silicate glasses,” *Journal of Geophysical Research* (1896-1977) **76**, 5489–5498 (1971).
- ¹⁹B. J. Jensen, D. B. Holtkamp, P. A. Rigg, and D. H. Dolan, “Accuracy limits and window corrections for photon Doppler velocimetry,” *Journal of Applied Physics* **101**, Publisher: American Institute of Physics, 013523 (2007).
- ²⁰O. T. Strand, D. R. Goosman, C. Martinez, T. L. Whitworth, and W. W. Kuhlow, “Compact system for high-speed velocimetry using heterodyne techniques,” *Review of Scientific Instruments* **77**, Publisher: American Institute of Physics, 083108 (2006).
- ²¹L. Davison, *Fundamentals of Shock Wave Propagation in Solids*, Shock Wave and High Pressure Phenomena (Springer-Verlag, Berlin Heidelberg, 2008).
- ²²M. A. Meyers, “Shock Waves: Equations of State,” in *Dynamic Behavior of Materials*, Section: 5 (John Wiley & Sons, Ltd, 2007), pp. 124–151.
- ²³K.-i. Kondo, S. Iio, and A. Sawaoka, “Nonlinear pressure dependence of the elastic moduli of fused quartz up to 3 GPa,” *Journal of Applied Physics* **52**, Publisher: American Institute of Physics, 2826–2831 (1981).
- ²⁴W. Schill, “Variational and multiscale modeling of amorphous silica glass,” Ph.D. thesis (California Institute of Technology, June 2020).
- ²⁵J. E. Gorfain, C. S. Alexander, and C. T. Key, “High-pressure shock response and phase transition of soda-lime glass,” *AIP Conference Proceedings* **2272**, Publisher: American Institute of Physics, 100011 (2020).
- ²⁶D. B. McWhan, “Linear compression of -quartz to 150 kbar,” *Journal of Applied Physics* **38**, Publisher: American Institute of Physics, 347–352 (1967).
- ²⁷S.-N. Luo, J. L. Mosenfelder, P. D. Asimow, and T. J. Ahrens, “Direct shock wave loading of Stishovite to 235 GPa: Implications for perovskite stability relative to an oxide assemblage at lower mantle conditions,” *Geophysical Research Letters* **29**, [_eprint: https://agupubs.onlinelibrary.wiley.com/doi/pdf/10.1029/2002GL015627](https://agupubs.onlinelibrary.wiley.com/doi/pdf/10.1029/2002GL015627), 36–1–36–4 (2002).
- ²⁸*Explicit dynamic analysis*, <https://abaqus-docs.mit.edu/2017>.
- ²⁹C. Kettenbeil, “Dynamic Strength of Silica Glasses at High Pressures and Strain Rates,” Ph.D. thesis (California Institute of Technology, 2019).
- ³⁰T. Ao, M. D. Knudson, J. R. Asay, and J.-P. Davis, “Strength of lithium fluoride under shockless compression to 114 GPa,” *Journal of Applied Physics* **106**, Publisher: American Institute of Physics, 103507 (2009).
- ³¹T. Oniyama, “Shock Compression of Molybdenum Single Crystals to High Stresses,” Ph.D. thesis (California Institute of Technology, 2020).
- ³²Y. M. Gupta, “Effect of crystal orientation on dynamic strength of LiF,” *Journal of Applied Physics* **48**, Publisher: American Institute of Physics, 5067–5073 (1977).

³³Q. Liu, X. Zhou, X. Zeng, and S. N. Luo, “Sound velocity, equation of state, temperature and melting of LiF single crystals under shock compression,” *Journal of Applied Physics* **117**, Publisher: American Institute of Physics, 045901 (2015).

³⁴A. Rohatgi, *Webplotdigitizer: version 4.4*, 2020.

Chapter 4

PRESSURE-SHEAR PLATE IMPACT EXPERIMENTS ON SODA-LIME GLASS

4.1 Background

As shown in Fig. 4.1, Pressure Shear Plate impact (PSPI) experiments involve oblique impact of an impactor on a parallel aligned target disk [1]. The oblique impact generates both longitudinal and shear waves in the target and can thus be used to study the shear response of materials confined to higher pressures. In contrast to the shock and release technique described in Chapter 1, the PSPI technique can be used to measure the strength of a material at a constant pressure. A variant of the PSPI technique sandwiches a thin foil of a material of interest between thicker disks (anvils) of higher shear impedance [2–4] (see Fig. 4.1b). This serves to probe the pressure equilibrated shear response of the sandwiched material which is subject to pressures and shear stresses prescribed by the anvils.

A schematic time-material position (t - X) diagram of the sandwiched PSPI experiment is shown in Fig. 4.2. The ‘shear window’ shown in the figure is the time duration for which the transverse velocity signal corresponds to the compressed state of the sandwiched material.

A schematic longitudinal and shear stress-particle velocity diagram for a sandwiched PSPI experiment is shown in Fig. 4.3. The stresses in the sandwiched material ‘ring up’ to a value determined by the impact velocity and the anvil material. If the anvils remain elastic under combined pressure-shear loading, the shear stress and strain experienced by the anvil as a function of time can be inferred from the measured transverse velocity profile. For a transverse free surface velocity $v_{fs}(t)$, the shear stress (τ) and strain (γ) experienced by the sandwiched sample is given by [5]:

$$\tau(t) = \frac{\rho_0 C_S V_{fs}(t)}{2} \quad (4.1)$$

$$\gamma(t) = \int_0^t \left(\frac{V_0 - V_{fs}(t')}{h} dt' \right) \quad (4.2)$$

where h is thickness of the sandwiched sample, ρ_0 is the density of the anvil, and C_S is the speed of elastic shear waves in the anvil.

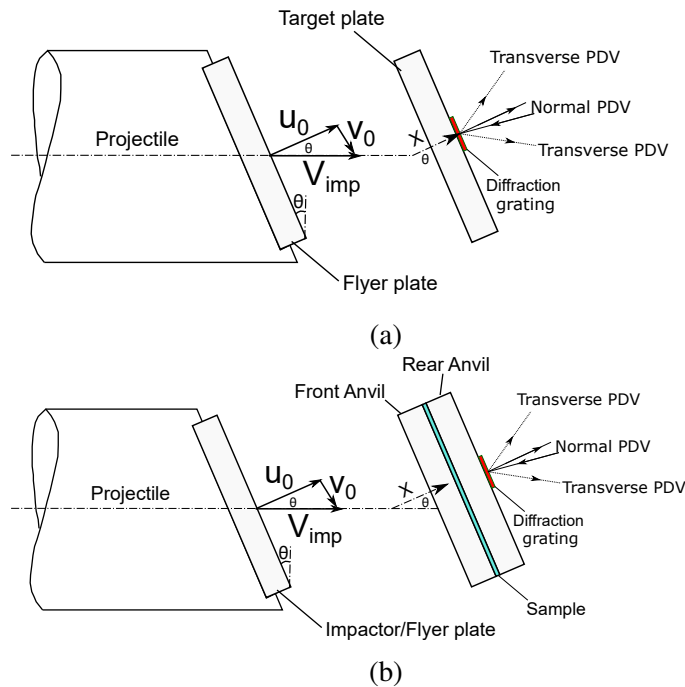


Figure 4.1: Schematic of pressure shear plate impact (PSPI) experiments. (a) Symmetric PSPI experiment, (b) Sandwiched PSPI experiment.

Symmetric PSPI experiments, wherein the impactor and target disks are of the same material, are used to calibrate parameters for modeling the anvil materials [6]. For experiments with normal impact stresses higher than the elastic limit of the anvils, these models are used to estimate the properties of the sandwiched material by forward simulations to reproduce the observed free-surface transverse velocity profile.

4.2 Experiments to determine the shear-strength of SLG at various pressures.

Several PSPI experiments have been conducted in the past to probe the shear-strength of SLG [6–9]. Experiments in [8] involved oblique impact between steel and SLG disks to probe the strength of SLG, behind the failure wave. The shear-strength of SLG was found to decrease significantly behind the failure-wave. The sandwiched PSPI technique was employed in [7] to probe the strength of SLG subject to normal stresses of 2.5-5 GPa. In that work, SLG wafers of various thicknesses were used to probe its strength as a function of shear-strain as well. Details of PSPI experiments in sandwiched configuration, performed using WC anvils and thick SLG wafers, is shown in Table 4.1. For reasons discussed later, two normal impact experiments with SLG sandwiched between WC anvils were also performed as a part of the

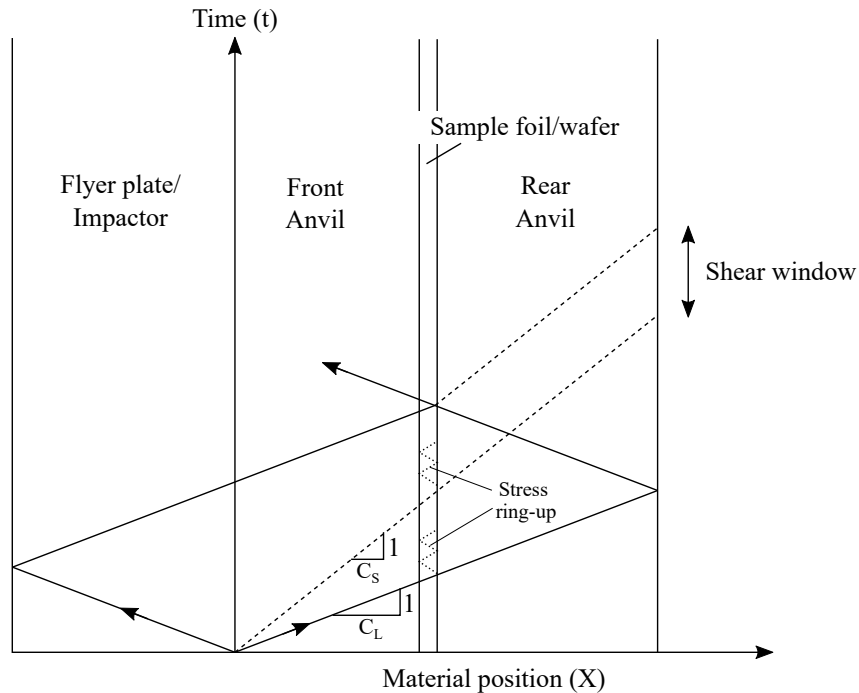


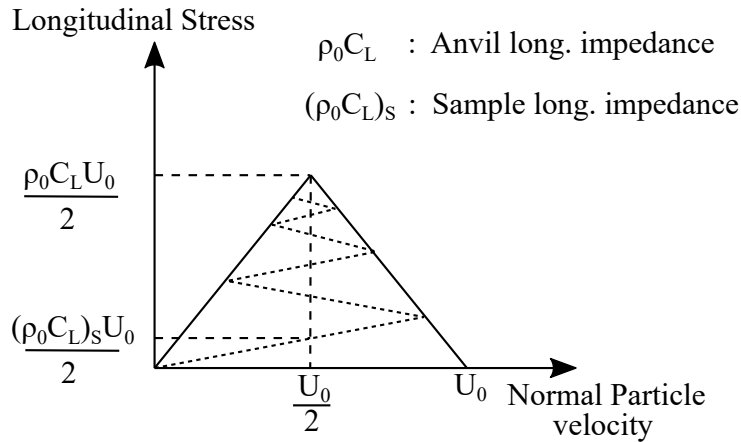
Figure 4.2: Time-material position ($t - X$) schematic of a sandwiched PSPI experiment. C_L and C_S denote the anvil material's longitudinal wave speed and shear wave speed, respectively, in Lagrangian coordinates.

| Expt. # | Thickness (mm) | | | V_{imp} (m/s) | $\theta(^{\circ})$ |
|---------|----------------|-------|---------------------|--------------------|--------------------|
| | Glass | Flyer | Anvils (front/rear) | | |
| CK-1807 | 0.3 | 4.97 | 1.96/3.70 | 328 | 18 |
| CK-1808 | 0.1 | 4.96 | 1.96/3.70 | 330 | 18 |
| AJ-1909 | 0.3 | 5.00 | 1.50/3.17 | 321 | 0 |
| AJ-2007 | 0.8 | 5.01 | 1.97/3.70 | 350 | 0 |

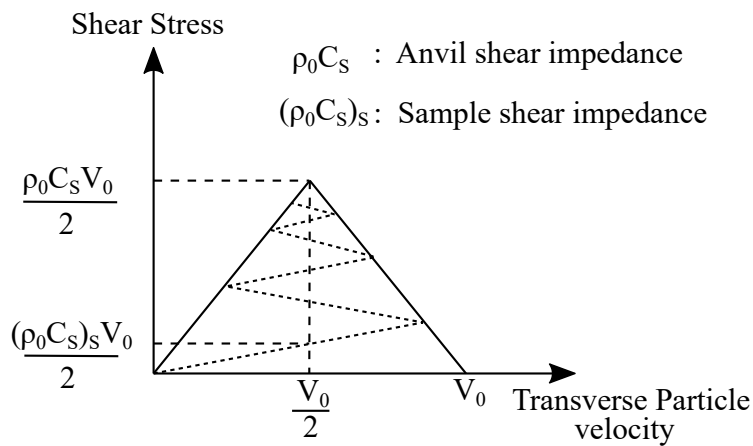
Table 4.1: Summary of experiments with SLG wafers sandwiched between WC anvils. Experiments CK-1807 and CK-1808 are taken from [9]. Experiments AJ-1909 and AJ-2007 are normal impact experiments.

present work. The PSPI experiments considered in Table 4.1 are taken from [9]. Results of these experiments are shown in Fig. 4.4.

Simulations performed in [9] to reproduce the results of experiments CK-1807 and 1808 were able to capture most of the features of the normal and transverse velocity profiles with good success. The simulations of these experiments show that the sandwiched SLG sample was able to withstand peak shear stresses of around 1.5 GPa at 14.5 GPa normal stress (13.5 GPa pressure), thus implying that the strength



a)



b)

Figure 4.3: A schematic of (a) longitudinal stress vs. particle velocity and (b) shear stress vs. particle velocity Hugoniots in sandwiched PSPI experiments. The dotted lines represent the sandwiched material's 'ring-up' response. The solid lines are the anvil materials stress Hugoniot, which for linearly elastic materials are straight lines in stress-particle velocity space.

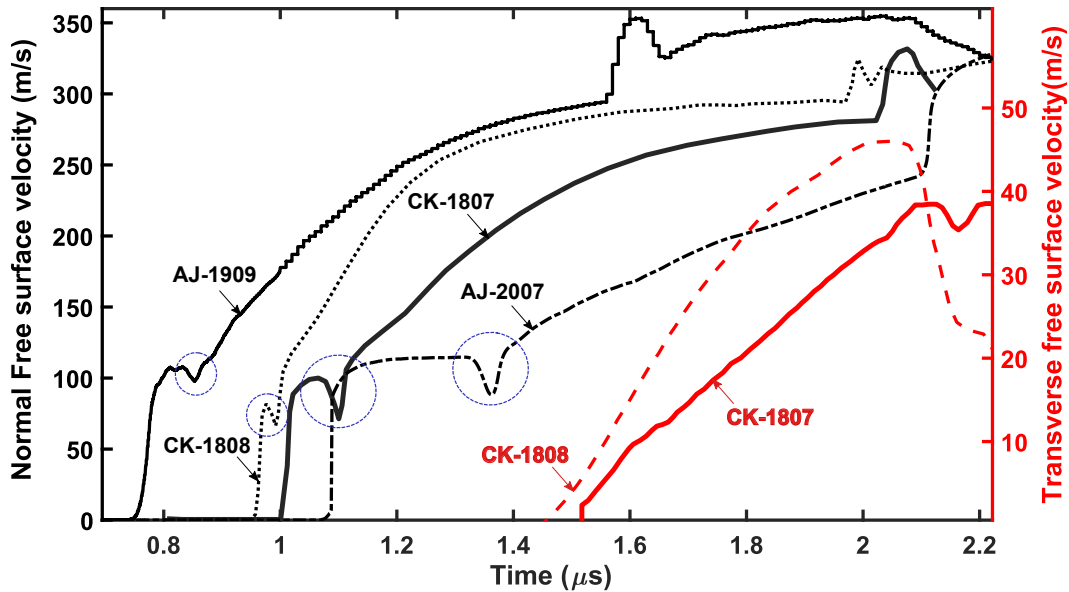


Figure 4.4: Free surface normal and transverse velocities for experiments shown in Table 4.1. The curves in black are normal free-surface velocities and curves in red are the transverse free-surface velocities for the PSPI experiments. The abrupt drop in normal free-surface velocity after the first normal stress ring-up is highlighted.

of SLG at these pressures is around 3 GPa.

However, the simulations in [9] were unable to capture the sudden drop in normal free surface velocity observed in Expts. CK-1807 and 1808. This drop, highlighted in Fig. 4.4, can be seen to occur at a free surface velocity of around 100 m/s. This corresponds to a first ring-up normal stress of around 5 GPa in SLG. Since the threshold stress for the onset of failure waves in SLG is also around 5 GPa, it appears reasonable to attribute this drop in velocity to the failure wave phenomenon. The cause underlying this drop in velocity was further explored using the normal impact experiments AJ-1909 and AJ-2007 as described next.

Explaining the drop in normal velocity

To evaluate the possibility that the observed drops in normal velocity were due to arrival of shear waves at the SLG wafer, normal impact experiments (with no shear) AJ-1909 and AJ-2007 were performed. As shown in Fig. 4.4, similar drops in velocities were also observed in these normal impact experiments thus indicating that shear stresses play no role in causing the observed drop in velocity. Similar drops in free surface velocity were also observed in sandwiched configuration PSPI experiments on Corning Glass (CG) wafers [10]. In that work, the authors postulate that this observed drop in particle velocity could be due to an open unglued gap

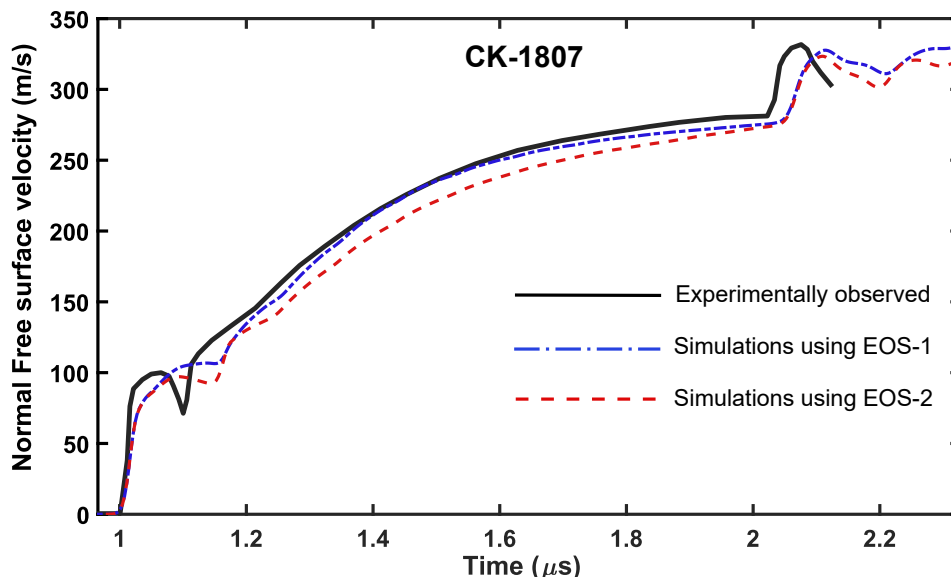


Figure 4.5: Plot of normal free surface velocity vs. time for Expt. CK-1807 and simulations using EOS-1 and EOS-2 equations of state for SLG (discussed in Chapter 2).

between the glass wafer and WC anvil. However, considering that these drops in normal velocity are of comparable magnitude across experiments and occur at similar normal stresses (5 GPa), it might be more reasonable to attribute this behavior to failure-waves or other phenomenon in SLG as opposed to an experimental artefact. Further PSPI experiments using other materials, like Alumina AD 995 (discussed next), as anvils and performed at different impact stresses can be helpful to conclusively evaluate the role of the failure wave phenomenon in the observed drop in surface velocity.

Further, a simulation was carried out to replicate the normal velocity profile of experiment CK-1807. This simulation used EOS-2 equation of state, which incorporates a densification due to the failure-wave, and other parameters discussed in Chapters 2 and 3 for SLG. As seen in Fig. 4.5, the simulation is able to reproduce a drop in normal velocity occurring between the first and second ring-ups as expected. However, the magnitude of the drop is considerably smaller than what is observed experimentally. A more significant drop in normal velocity can be achieved by simulations if reduction in strength of SLG is considered. This lends further support to the possibility that the drop in velocity is a result of the glass' material behavior.

| Expt. # | Impactor thickness (mm) | Target thickness (mm) | Impact velocity (m/s) | Peak normal stress (GPa) | Skew angle (°) | Impact tilt (mrads) |
|---------|-------------------------|-----------------------|-----------------------|--------------------------|----------------|---------------------|
| AJ-2001 | 4 | 4 | 234 | 4.4 | 25 | 1.5 |

Table 4.2: Summary of symmetric PSPI experiment on alumina AD995.

4.3 Alumina AD995 as an anvil for PSPI experiments

A prerequisite for being able to infer the shear stress-strain response of the sandwiched material, using Eqs. 4.1, 4.2, is that the anvils remain elastic. This would mean that the anvils used for PSPI experiments should have a Hugoniot Elastic Limit (HEL) higher than the desired impact stresses. Further, the longitudinal wave speed in the material should be low enough to allow for a significant shear window (see Fig. 4.2). Alumina AD995 has a HEL of 6.71 GPa, a longitudinal wave speed of 10.66 km/s, and a shear wave speed of 6.28 km/s [11].

A symmetric PSPI experiment was performed on Alumina AD995 to verify feasibility of its use as an anvil in PSPI experiments involving normal impact stresses lesser than its HEL of 6.71 GPa. The Alumina AD995 disks were sourced from ETD Precision Ceramics Corp., San Jose, CA. The impactor disk was 4 mm thick and 34 mm in diameter, while the target disk was of the same thickness (4 mm) and 32 mm in diameter. Both disks were lapped and polished on both sides to the best possible finish at Production Lapping Inc., Monrovia, CA. A thin layer of gold was vapor deposited onto the surface of the impactor to serve as a conductive layer which in turn serves to trigger PDV data-acquisition upon contact between impactor and target. A diffraction grating was also deposited on the rear surface of the target, to facilitate transverse PDV as described in [9]. The impact velocity for the symmetric PSPI experiment was 234 m/s, with a skew angle of 25°. This results in a normal stress of 4.4 GPa in alumina. The free surface normal and transverse velocity results for this experiment are shown in Fig. 4.6. The parameters for this experiment are summarized in Table 4.2.

As shown in Fig. 4.6, due to a tilt between the target and impactor surfaces, the transverse velocity shows an initial increase in value before the arrival of shear waves at the free surface. Furthermore, the first peak transverse velocity can be seen to be around 55 m/s, which is significantly lesser than the expected 99 m/s ($= 234 \sin(25^\circ)$). This is attributed to the yielding/failure of alumina that is postulated to occur under pure-shear loading prevalent after the longitudinal release wave and shear waves interact. A similar observation was made in the case of WC in

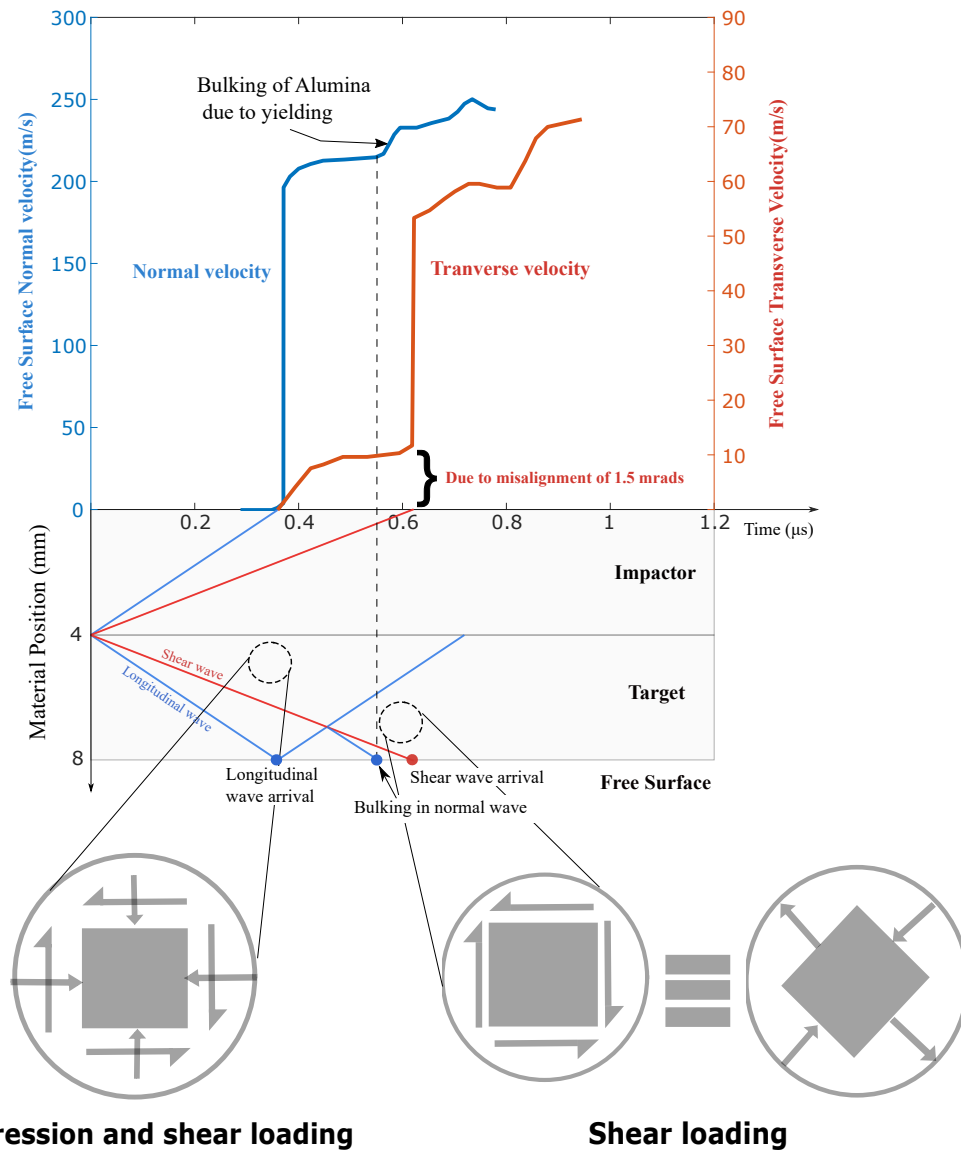


Figure 4.6: Free surface velocities for symmetric PSPI of alumina AD 995 (Expt. AJ-2001). The free surface velocities are plotted alongside a X-t characteristic diagram. Stress states prevalent in relevant regions of the X-t diagram is shown. The pure shear state is postulated to have caused a failure in the Alumina material.

[12]. This result thus implies that the alumina AD995 anvils can sustain a maximum shear stress of around 600 MPa before yielding. Thus, alumina AD995 appears to be a feasible anvil for carrying out sandwiched configuration PSPI experiments, involving normal stresses less than 6.71 GPa and shear stresses less than 600 MPa.

References

- ¹A. S. Abou-Sayed, R. J. Clifton, and L. Hermann, “The oblique-plate impact experiment,” *Experimental Mechanics* **16**, 127–132 (1976).
- ²S. Grunschel, “Pressure-shear plate impact experiments on high-purity aluminum at temperatures approaching melt,” Ph.D. thesis (Brown University, 2009).
- ³C. H. Li and R. J. Clifton, “Dynamic stress-strain curves at plastic shear strain rates of 10^5 s^{-1} ”, AIP Conference Proceedings **78**, Publisher: American Institute of Physics, 360–366 (1982).
- ⁴R. W. Klopp, R. J. Clifton, and T. G. Shawki, “Pressure-shear impact and the dynamic viscoplastic response of metals,” *Mechanics of Materials* **4**, 375–385 (1985).
- ⁵R. J. Clifton and R. W. Klopp, “Pressure-shear plate impact testing”, *Metals handbook* **8**, Publisher: Amer. Soc. Metals Metals Park, 230–239 (1985).
- ⁶C. Kettenbeil, Z. Lovinger, S. Ravindran, M. Mello, and G. Ravichandran, “Pressure-shear plate impact experiments at very high pressures,” AIP Conference Proceedings **2272**, Publisher: American Institute of Physics, 120010 (2020).
- ⁷S. Sundaram and R. J. Clifton, “Flow behavior of soda-lime glass at high pressures and high shear rates,” AIP Conference Proceedings **429**, Publisher: American Institute of Physics, 517–520 (1998).
- ⁸R. J. Clifton, M. Mello, and N. S. Brar, “Effect of shear on failure waves in soda lime glass,” AIP Conference Proceedings **429**, Publisher: American Institute of Physics AIP, 521 (1998).
- ⁹C. Kettenbeil, “Dynamic Strength of Silica Glasses at High Pressures and Strain Rates,” Ph.D. thesis (California Institute of Technology, 2019).
- ¹⁰H. D. Espinosa, X. Yueping, and N. S. Brar, “Micromechanics of failure waves in glass: I. Experiments,” *Journal of the American Ceramic Society* **80**, Publisher: Wiley Online Library, 2061–2073 (1997).
- ¹¹N. K. Bourne, J. C. F. Millett, M. Chen, J. W. McCauley, and D. P. Dandekar, “On the Hugoniot elastic limit in polycrystalline alumina,” *Journal of Applied Physics* **102**, Publisher: American Institute of Physics, 073514 (2007).
- ¹²B. Zuanetti, T. Wang, and V. Prakash, “Plate impact investigation of the dynamic response of commercial tungsten carbide under shock-induced compression and

combined compression-and-shear loading,” *International Journal of Impact Engineering* **131**, 200–208 (2019).

SUMMARY AND FUTURE WORK

5.1 Summary

The properties and mechanisms underlying the failure wave phenomenon in SLG were probed using experiments and finite element simulations in this work as described in Chapter 2. Therein it was inferred that the failure wave causes an additional volumetric compression of 4.6% in the SLG material at impact stresses of around 6 GPa. This densification is postulated to arise from a phase transition or atomic coordination number change in the material. It was also observed that there was no failure wave generated in SLG for impact stresses of around 10 GPa, indicating the disappearance of this phenomenon at higher impact stresses. Further, as described in Chapter 3, shock compression and release experiments were performed on SLG to gain insights into the existence and properties of a phase transition in the material at impact stresses of 6-7.5 GPa. Results from the performed experiments were analyzed alongside results from similar previously published works. The estimates of shear modulus strongly indicate gradual permanent phase transition of SLG to a stiffer phase like stishovite. This noted phase transition in SLG is seen to start at around 5.8 GPa, close to the reported threshold stress for the onset of failure waves in SLG. The data from these experiments were used as a basis for modelling the shock compression and release behavior of SLG using finite element analysis. These simulations showed considerable success in reproducing the prominent features observed in the recorded particle velocity profiles.

There is, however, significant scope for further investigation of the properties of soda-lime and other silica glasses. The following sections discuss a list of suggested experiments to gain further insight into the behavior of silica glasses.

5.2 Sandwiched PSPI experiments on SLG at 4-6 GPa normal stresses

As discussed in Chapter 4, the sandwiched configuration PSPI technique offers a robust means of estimating the strength of a material subject to high compressive stresses. These experiments can be used to gauge the effect of failure waves on the shear strength of SLG. To this end, PSPI experiments at different pressures can be performed - one with normal impact stresses below the failure wave threshold for SLG (4.7 GPa [1]) and another with normal stresses higher than the failure-wave

threshold. Previous works [2] have attempted to use PSPI experiments to capture the effect of failure waves on the strength of SLG. However, it is suspected that the SLG wafers used were too thin ($5\ \mu\text{m}$), which in turn causes excessive shearing of the material (see Eq. 4.2). It is suggested that this high shear strain in the SLG, and not the failure wave phenomenon, is responsible for decrease in SLG's shear-strength observed in those experiments. This decrease in shear strength/onset of damage was observed at normal impact stresses of 3.5 GPa, which is significantly lesser than the threshold-stress for failure waves in SLG. It is thus recommended that future experiments to probe the shear strength of SLG at these pressures use wafers that are $100\ \mu\text{m}$ or thicker.

As discussed in section 3 of Chapter 4, alumina AD995 is a feasible anvil for these PSPI experiments involving normal stresses of 4-6 GPa, provided the shear stresses involved are less than 600 MPa.

5.3 Normal plate impact experiments on SLG and other silica glasses

As discussed in Chapter 2, normal plate impact experiments to investigate the existence of failure waves in anomalous [3] glasses like borosilicate and fused silica can provide insights into the role of network modifying ions in the failure wave phenomenon. Symmetric normal impact experiments involving SLG impactors and targets can be used to characterize the change in the refractive index of SLG, with respect to 1550 nm light, when subject to shock loading. This would enable use of SLG as a window in shock compression experiments involving use of 1550 nm light for velocimetry.

5.4 Imaging the SLG under impact at 3 GPa and 6 GPa

The ability to accurately image the evolution of failure waves in SLG can be decisive in identifying mechanisms underlying the failure wave phenomenon. As discussed in Chapter 2, previous works have attempted to image failure waves in SLG by either using streak-photography [4, 5] from a side-view of the target or imaging the failure waves at the impact surface from the rear-surface of the sample [5]. Photography of failure waves from the side of the SLG target is obstructed by 'surface failure-waves' which travel significantly faster than the internal failure waves. As shown in Fig. 5.1, these surface failure waves are postulated to arise due to prevalence of lower pressures at the edges. It is therefore suggested that experiments for imaging failure waves view the impact surface through the rear-surface of the target. These imaging experiments need to be conducted for impact stresses below and above the failure

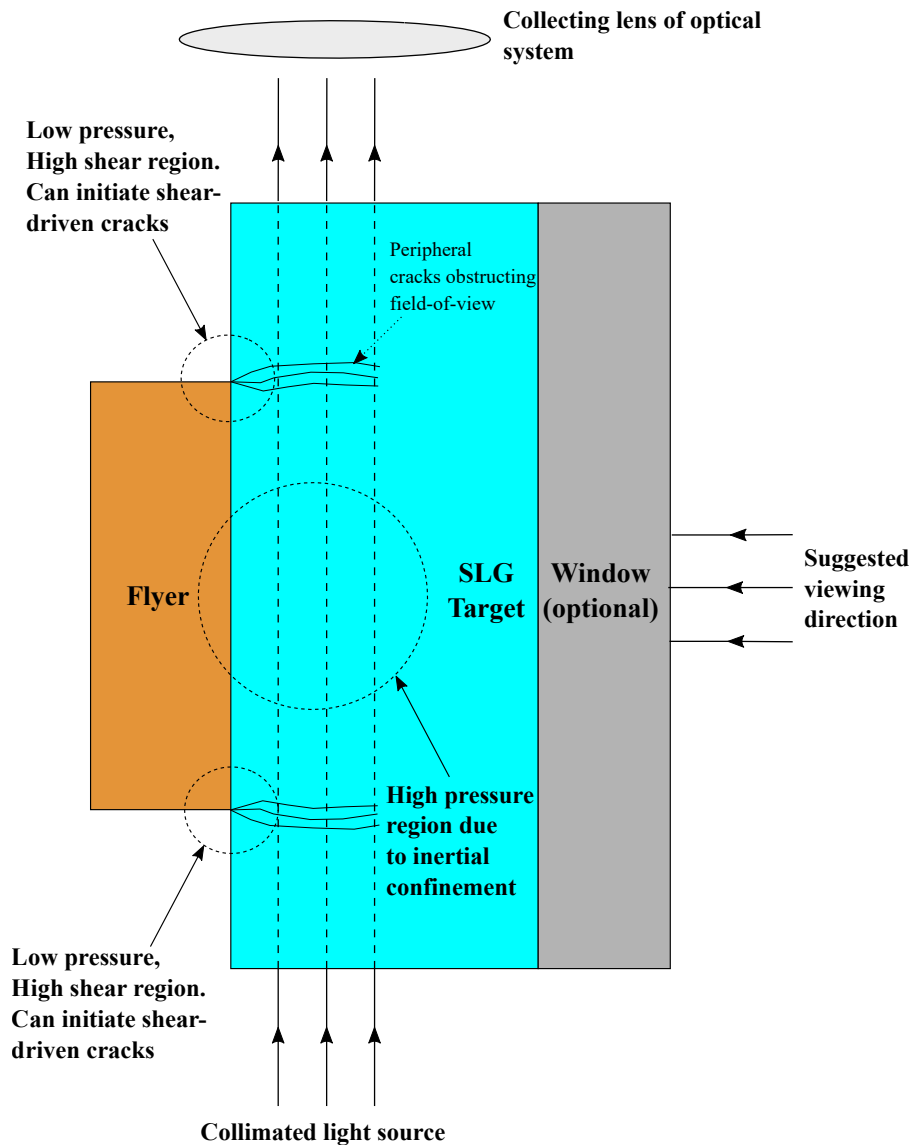


Figure 5.1: Schematic of a plate impact experiment involving imaging of failure waves in SLG.

wave threshold stress, at 3 GPa and 6 GPa, respectively, to obtain more insights into failure-wave formation and propagation.

5.5 Determining shear modulus of SLG as a function of impact stress using oblique impact experiments

The shear modulus of a material is directly related to the speed of elastic shear waves in the material. Using this principle, the shear modulus of SLG as function of pressure can be determined from the time taken by a small-amplitude shear wave to traverse through the SLG target in an oblique plate impact experiment.

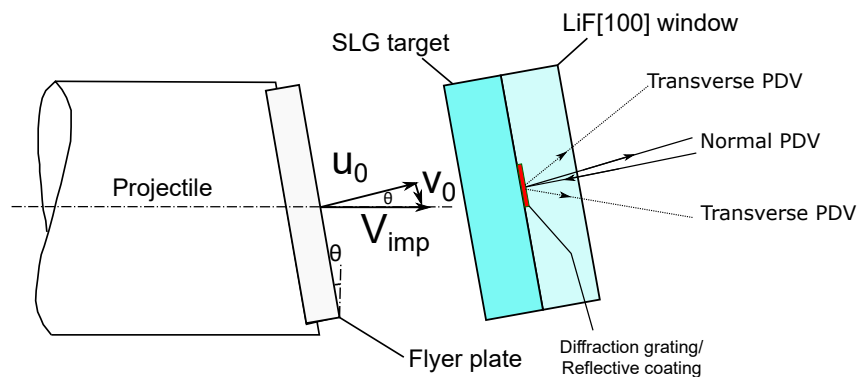


Figure 5.2: Schematic of a suggested experimental configuration to measure shear modulus of SLG as a function of pressure. The PDV arrangement can alternatively be replaced by a camera to detect the arrival of shear waves at the SLG rear surface.

The suggested experimental setup, shown in Fig. 5.2, is similar to a regular PSPI experiment with a low skew angle ($2\text{--}3^\circ$), to keep the shear wave amplitude small. The difference lies in the use of a window to retain the compressive stress at the rear surface of SLG. The arrival of a shear wave at the rear surface of the SLG disk can be detected using a high speed camera or with the use of a transverse PDV setup that accounts for the presence of the window material.

The experimentally obtained measurements of the shear modulus of SLG as a function of pressure can be compared with the theoretically predicted relation (Fig. 3.9b) which was discussed in Chapter 3. This can further serve to conclusively establish the presence/absence of a gradual phase-transition occurring in SLG under shock compression.

References

- ¹D. Dandekar and P. Beaulieu, “Failure wave under shock wave compression in soda-lime glass,” *Metallurgical and Material Applications of Shock-Wave and High-Strain-Rate Phenomena*, 211–218 (1995).
- ²S. Sundaram and R. J. Clifton, “Flow behavior of soda-lime glass at high pressures and high shear rates,” *AIP Conference Proceedings* **429**, Publisher: American Institute of Physics, 517–520 (1998).
- ³A. Arora, D. B. Marshall, B. R. Lawn, and M. V. Swain, “Indentation deformation/fracture of normal and anomalous glasses,” *Journal of Non-Crystalline Solids* **31**, 415–428 (1979).
- ⁴N. K. Bourne, Z. Rosenberg, and J. E. Field, “High-speed photography of compressive failure waves in glasses,” *Journal of Applied Physics* **78**, Publisher: American Institute of Physics, 3736–3739 (1995).

⁵S. Bauer, F. Bagusat, E. Strassburger, M. Sauer, and S. Hiermaier, “New insights into the failure front phenomenon and the equation of state of soda-lime glass under planar plate impact,” *Journal of Dynamic Behavior of Materials* **7**, 81–106 (2021).

Appendix A

EQUATION OF STATE FOR SODA-LIME GLASS

The procedure for constructing the Equation of State (EOS) for soda-lime glass (SLG) employed in the present simulations from data available in the literature is outlined in the following section.

Considering the stress-particle velocity ($\sigma_x - u_p$) Hugoniot diagram, the longitudinal stress in a wave as a function of the in-material particle velocity is given by [1, 2]:

$$\sigma_x(\tilde{u}_p) = \begin{cases} \int_{u_p=0}^{u_p=\tilde{u}_p} \rho_0 C_L(u_p) du_p & \text{for } \tilde{u}_p \leq u_{pHEL} \\ \sigma_{xHEL} + \rho_0 U_s(\tilde{u}_p - u_{pHEL}) & \text{for } \tilde{u}_p > u_{pHEL} \end{cases} \quad (\text{A.1})$$

where C_L is the Lagrangian wave speed corresponding to a particular particle velocity below the HEL, for $u_p \leq u_{pHEL}$. For $u_p \geq u_{pHEL}$, the waves coalesce to form a shock with shock speed U_s . The $U_s - u_p$ relationship is expressed in the conventional form: $U_s = C_0 + S[u_p]$, where C_0 is the bulk-wave speed of SLG at a strain of ϵ_{HEL} and $[u_p]$ is the jump in particle velocity across the second wave. Also, using continuity of σ_x in Eq. A.1, it can be inferred that $\sigma_{xHEL} = \sigma_x(u_{pHEL})$.

Using Eq. A.1, the data shown in Fig. A.1 is integrated to obtain a stress-particle velocity curve. Then, Eq. A.2 is used to convert particle velocities into volumetric strains. Thus, knowing particle velocities as a function of strains, the stress-strain plots shown in Fig. 2.5 can be constructed.

$$\epsilon_{vol}(\tilde{u}_p) = \begin{cases} \int_{u_p=0}^{u_p=\tilde{u}_p} \frac{du_p}{C_L(u_p)} & \text{for } \tilde{u}_p \leq u_{pHEL} \\ \epsilon_{HEL} + \frac{\tilde{u}_p - u_{pHEL}}{U_s(\tilde{u}_p)} & \text{for } \tilde{u}_p > u_{pHEL} \end{cases} \quad (\text{A.2})$$

Using Eq. 2.1, the pressure (p) is obtained by subtracting the appropriate deviatoric stresses from the longitudinal stress (σ_x). This EOS is then provided to LS-Dyna in a discretized and tabulated format.

The wave speed and particle velocity relationship [3] also consists of the initial elastic release wave speeds as a function of the particle velocity change in SLG. The initial elastic release wave speed (C_R) and the bulk-wave speed (C_0) at a particular strain are computed by the following equations:

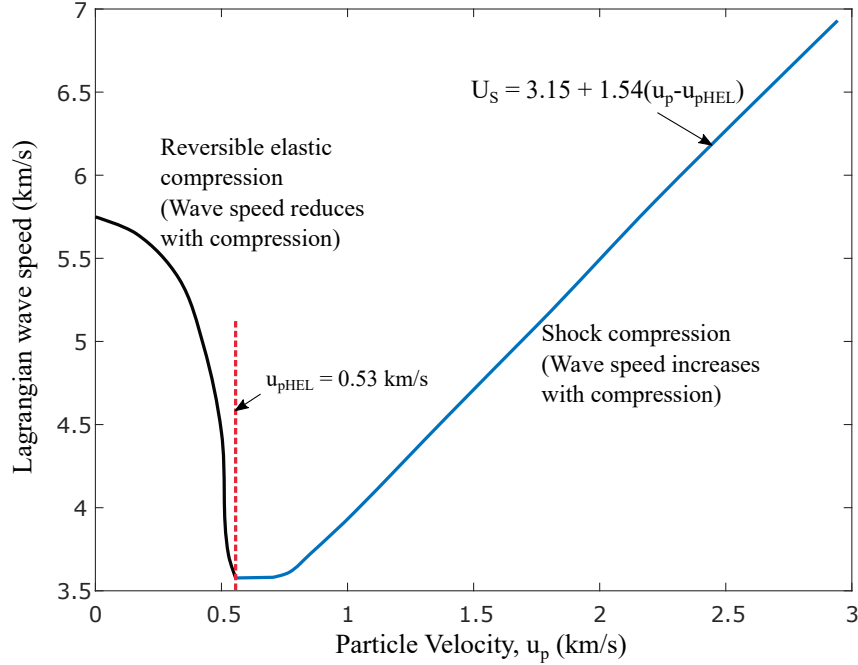


Figure A.1: Lagrangian wave speed vs. particle velocity diagram for soda-lime glass (SLG). Adapted from Alexander et al. [3]

$$C_0^2(\varepsilon_{vol}) = \frac{1}{\rho_0} \frac{dp(\varepsilon_{vol})}{d\varepsilon_{vol}} \quad (\text{A.3})$$

$$C_R^2(\varepsilon_{vol}) = C_0^2(\varepsilon_{vol}) + \frac{4G}{3\rho_0} \quad (\text{A.4})$$

The simulations used in the present work made use of the standard von Mises J_2 plasticity model in LS-Dyna which computes the release wave speed using Eq. A.4. It is seen from Fig. 2.5 that the initial elastic release wave speed increases with strain, i.e, the slope of the elastic release path increases. The available initial release wave speed vs. particle velocity data were incorporated into simulations in Chapter 3 to better reproduce the release behavior of SLG. Previous works dealing with the stress release behavior of SLG and other silica glasses [4–6] had not implemented the release wave data from Alexander’s work [3] in their simulations.

The stress-strain curve for EOS-2, shown in Fig. 2.5(b), consists of a densification section with a low-slope to account for the slower second wave observed in experiments with 4-6 GPa impact stresses [7–9]. The speed of the second wave is determined to be around 1.3 km/s from the experiments conducted in this work, and from past experiments as well [7–9]. In experiments with impact stresses of 6.4 GPa, the observed peak free surface velocity is close to 800 m/s. This information

from experiment #AJ-1 is used to construct the densification section of EOS-2 as seen in Fig. A.2.

The SLG is taken to be elastic for stresses below 7.5 GPa [3]. This would mean that the unloading curve would be a simple reflection of the loading curve about the ordinate-axis in the $\sigma_X - u_p$ plane as shown in Fig. A.2. Therefore, the observed free surface velocity of 800 m/s corresponds to an in-material particle velocity of 400 m/s and stress of 5.6 GPa – denoted by the point A in Fig. A.2. Using Eq. A.5, a line with slope corresponding to a second/densification wave speed (U_{SW}) of 1.3 km/s is constructed from A to intersect the Hugoniot of the WC impactor at B.

Using the laws of conservation of mass and momentum across a shock [1], the following equation can be used to express the densification wave-speed (U_{SW}) in terms of properties at points A and B:

$$U_{SW} = \frac{1}{\rho_0} \frac{(\sigma_X)_B - (\sigma_X)_A}{((u_p)_B - (u_p)_A)} \quad (\text{A.5})$$

Therefore, point B corresponds to the in-material particle velocity and stress of the second wave/recompression bump. This stress-wave releases at the free surface of the SLG to the velocity of the bump observed in experiment #AJ-1. The expression for the initial elastic release wave speed in EOS-2 is the same as EOS-1.

In EOS-1, the loading path and unloading path are the same for stresses below the HEL. They differ for higher stresses as shown in Fig. 2.5(a). In EOS-2 (Fig. 2.5(b)), the loading and unloading paths are the same for stresses below the densification section. The volume densification due to the failure wave is evaluated using Eq. A.6 to be 4.6 %.

$$\Delta \varepsilon_{vol} = \frac{((u_p)_B - (u_p)_A)}{U_{SW}} \quad (\text{A.6})$$

The Grüneisen Parameter (Γ_0) is computed from the shock-res shock data provided for SLG by Grady et al. [9]. Γ_0 is related to the mass-specific internal energy change across a shock (E) as follows [2]:

$$p_2 - p_1 = \Gamma_0 \rho_0 (E_2 - E_1) \quad (\text{A.7})$$

where the states 1 and 2 are different points on a p-V diagram with same specific volume ($1/\rho$), but different specific internal energies. The value of Γ_0 obtained by using Eq. A.7 on the data used in [9] is shown in Table 2.2.

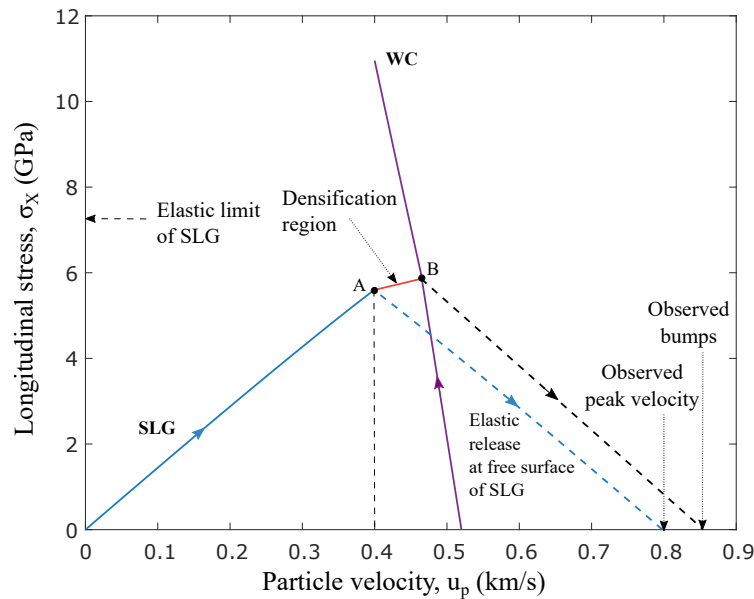


Figure A.2: The stress-particle velocity (σ - u_p) Hugoniot diagram used to construct the densification region A-B using results from experiments #AJ-1, #AJ-2, and #AJ-3.

It was observed that the value of Γ_0 did not significantly affect the outcome of the simulations. As stated earlier, a possible reason for this could be that the specific internal energies encountered in the simulations and the Hugoniot data provided by Alexander et al. [3] were very similar. This would mean that the right-hand side of Eq. A.7 would be negligible, making the two pressures approximately equal regardless of the value of Γ_0 .

References

- ¹L. Davison, *Fundamentals of Shock Wave Propagation in Solids*, Shock Wave and High Pressure Phenomena (Springer-Verlag, Berlin Heidelberg, 2008).
- ²M. A. Meyers, “Shock Waves: Equations of State,” in *Dynamic Behavior of Materials*, Section: 5 (John Wiley & Sons, Ltd, 2007), pp. 124–151.
- ³C. S. Alexander, L. C. Chhabildas, and D. W. Templeton, “The Hugoniot elastic limit of soda-lime glass,” *AIP Conference Proceedings* **955**, Publisher: American Institute of Physics, 733–738 (2007).
- ⁴J. E. Gorfain, C. T. Key, and C. S. Alexander, “Application of a computational glass model to the shock response of soda-lime glass,” *Journal of Dynamic Behavior of Materials* **2**, 283–305 (2016).
- ⁵C. S. Alexander, L. C. Chhabildas, W. D. Reinhart, and D. W. Templeton, “Changes to the shock response of fused quartz due to glass modification,” *International*

Journal of Impact Engineering, Hypervelocity Impact Proceedings of the 2007 Symposium **35**, 1376–1385 (2008).

⁶M. J. Davis, “Laser-shock-induced spall and the intrinsic strength of glass,” International Journal of Applied Glass Science **7**, 364–373 (2016).

⁷C. H. M. Simha and Y. M. Gupta, “Time-dependent inelastic deformation of shocked soda-lime glass,” Journal of Applied Physics **96**, Publisher: American Institute of Physics, 1880–1890 (2004).

⁸G. I. Kanel, A. A. Bogatch, S. V. Rasorenov, and Z. Chen, “Transformation of shock compression pulses in glass due to the failure wave phenomena,” Journal of Applied Physics **92**, 5045–5052 (2002).

⁹D. E. Grady and L. C. Chhabildas, “Shock-wave properties of soda-lime glass,” English, in Iyer K.R. and Chou S.C. (eds) Proceedings of the 14th U.S. Army Symposium on solid mechanics (Nov. 1996).

Appendix B

WINDOW CORRECTIONS: OPTICAL AND IMPEDANCE MISMATCH

The details of processing PDV data, obtained in experiments that use a window, to infer the stress-strain response of the material is provided in this Appendix. The two main corrections necessary are 1.) optical corrections and 2.) stress corrections

The necessity for optical correction arises mainly from a change in optical path length effected by the shock/release waves travelling in the window. Stress corrections are due to a mismatch in impedance between the LiF [100] window and the SLG target.

Optical correction for shock-wave in window

Figure B.1 shows a schematic involving optical path correction for shock-wave propagating in LiF window. The procedure for determining window correction is outlined next.

$$u_{actual} = -\frac{dL_{full}}{dt} = -\frac{dX_1}{dt} - \frac{dX_2}{dt} - \frac{dX_3}{dt}$$

$$u_{obs} = -\eta \frac{dX_1}{dt} - \eta_0 \frac{dX_2}{dt} - \frac{dX_3}{dt}$$

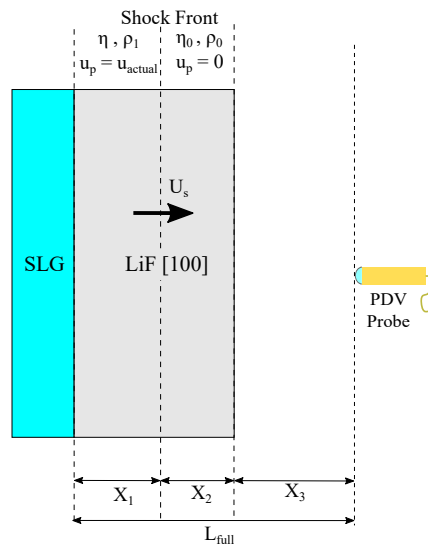


Figure B.1: Schematic of window-correction for shock-wave in window.

where

$$\begin{aligned}
 \frac{dX_1}{dt} &= U_s - u_{actual} \\
 \frac{dX_2}{dt} &= -U_s \\
 \frac{dX_3}{dt} &= 0 \\
 u_{obs} &= -\eta(U_s - u_{actual}) + \eta_0 U_s \\
 U_s &= C_0 + S u_{actual} \\
 \eta &= A + B \rho_1 \\
 \rho_1 &= \frac{\rho_0}{\left(1 - \frac{u_{actual}}{C_0 + S u_{actual}}\right)}
 \end{aligned}$$

In the above equations, X_1, X_2, X_3 are the distances shown in Fig. B.1. U_s is the shock-velocity in the window in material frame. Since the material ahead of the shock is considered to be under ambient conditions, the material frame and spatial frame shock-velocity are identical for this problem. u_{actual} is the actual target-window interface velocity, and u_{obs} is the measured target-window interface velocity. η_0 is the refractive index of window under ambient conditions, and η is the refractive index of the window material behind the shock-wave. Similarly, ρ_0 is the density of the window material under ambient conditions, and ρ_1 is the density of the window material behind the shock-wave. C_0 and S are material parameters used to relate the shock-wave speed in the window to the particle velocity difference across the shock-wave. Using the above equations, u_{obs} can be expressed as a function of u_{actual} [1] as:

$$u_{obs} = -(A + B \rho_1(u_{actual}))(U_s - u_{actual}) + \eta_0 U_s(u_{actual}).$$

Optical correction for release fan in window

Figure B.2 depicts the release-fan in the LiF window, which is formed when the shock wave is reflected off the free surface of the LiF window. The density, and hence the refractive index of LiF, varies continuously across the release fan. This variation in the refractive index will have to be accounted for in computing the optical path length for a light signal travelling to and from the PDV probe. The procedure adopted to obtain an optical correction for this problem is similar to that used in [2], where optical corrections were determined for a compression-fan in a window. Similar to the case of optical correction due to shock-wave in window, the

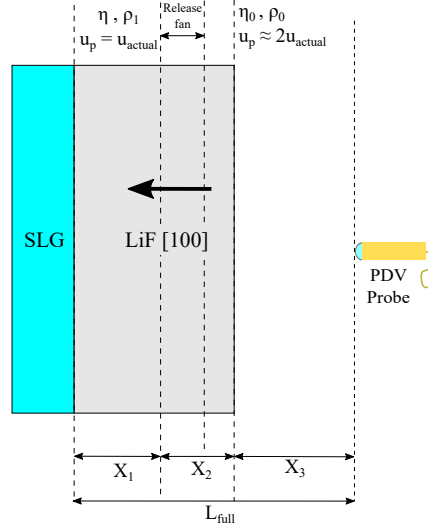


Figure B.2: Schematic of window-correction for release fan in window.

observed velocity at the interface is related to the actual velocity as:

$$u_{obs} = \eta u_{actual} - 2(\eta_0 - 1)u_{actual} - \int_{x_a(t)}^{x_b(t)} \frac{\partial \eta}{\partial t} dx \quad (\text{B.1})$$

It remains to evaluate: $\int_{x_a(t)}^{x_b(t)} \frac{\partial \eta}{\partial t} dx$.

Consider recasting this integral in material coordinate h , where $h = 0$ at LiF-SLG interface, $h = h_a(t)$ at $x = x_a(t)$, and $h = h_b(t)$ at $x = x_b(t)$. For $h \geq h_a(t)$, the transformation from h to x can be expressed as follows, for $x_i(t)$ denoting the spatial-coordinate of the SLG-LiF interface:

$$x(h, t) = x_i(t) + \frac{\rho_0 h_a(t)}{\rho_1} + \int_{h_a(t)}^h \frac{\rho_0}{\rho(h')} dh' \quad (\text{B.2})$$

For evaluating $\int_{x_a(t)}^{x_b(t)} \frac{\partial \eta}{\partial t} dx$, we need dx for a constant t . By evaluating this differential using Eq. B.2, we get : $dx = \partial x(h, t)|_t = \frac{\rho_0}{\rho(h)} dh$. This can be used to evaluate $\int_{x_a(t)}^{x_b(t)} \frac{\partial \eta}{\partial t} dx$ as follows:

$$\begin{aligned} \int_{x_a(t)}^{x_b(t)} \frac{\partial \eta}{\partial t} dx|_t &= \int_{h_a(t)}^{h_b(t)} \frac{\partial \eta}{\partial t} \Big|_x (h(x, t), t) \frac{\rho_0}{\rho(h)} dh \\ &= \int_{h_a(t)}^{h_b(t)} \frac{\partial \eta}{\partial \rho} \frac{\partial \rho}{\partial t} \Big|_x (h(x, t), t) \frac{\rho_0}{\rho(h)} dh \end{aligned} \quad (\text{B.3})$$

Further,

$$\left. \frac{\partial \rho}{\partial t} \right|_x (h(x, t), t) = \left. \frac{\partial \rho}{\partial h} \right|_t \left. \frac{\partial h}{\partial t} \right|_x + \left. \frac{\partial \rho}{\partial t} \right|_h \quad (\text{B.4})$$

The individual components of Eq. B.4 are evaluated next. To evaluate $\left. \frac{\partial h}{\partial t} \right|_x$, differentiate Eq. B.2 with respect to t keeping x constant.

$$\cancel{\left. \frac{\partial x(h, t)}{\partial t} \right|_x} \overset{0}{=} \frac{\partial x_i(t)}{\partial t} + \frac{\rho_0}{\rho_1} \frac{\partial h_a(t)}{\partial t} + \frac{\rho_0}{\rho(h)} \left. \frac{\partial h}{\partial t} \right|_x - \frac{\rho_0}{\rho(h_a)} \frac{\partial h_a(t)}{\partial t} \quad (\text{B.5})$$

Using continuity in the release – fan,

$$\begin{aligned} \rho(h_a) &= \rho_1 \\ 0 &= \cancel{\left. \frac{\partial x_i(t)}{\partial t} \right|_x} \overset{u_{actual}}{=} + \frac{\rho_0}{\rho(h)} \left. \frac{\partial h}{\partial t} \right|_x \\ \implies \left. \frac{\partial h}{\partial t} \right|_x &= -u_{actual} \frac{\rho(h)}{\rho_0} \end{aligned} \quad (\text{B.6})$$

To evaluate $\left. \frac{\partial \rho}{\partial h} \right|_t$, consider $\rho = \rho(u_{actual}, u)$, where u is particle velocity:

$$\left. \frac{\partial \rho}{\partial h} \right|_t = \left. \frac{\partial \rho}{\partial u} \frac{\partial u}{\partial h} \right|_t \quad (\text{B.7})$$

Consider Fig. B.3 to evaluate Eq. B.7. Note that although material properties like C_h and $\frac{\partial C_h}{\partial u}$ are expressed as functions of particle velocity (u), they are actually functions of both u and actual-velocity u_{actual} , i.e., $C_h = C_h(u_{actual}, u)$ and $\frac{\partial C_h}{\partial u} = \frac{\partial C_h(u_{actual}, u)}{\partial u}$. The dependence on both variables ensures the material-frame indifference of these material properties. For sake of brevity, henceforth C_h and its derivative will be expressed only as functions of u , although where required, its dependence on u_{actual} will be utilized.

$$\begin{aligned} (L - h) &= C_h(u)(t - t_0) \\ \implies C_h(u) &= \frac{(L - h)}{t - t_0} \\ \implies \left. \frac{\partial C_h(u)}{\partial u} \frac{\partial u}{\partial h} \right|_t &= \frac{-1}{t - t_0} \\ \left. \frac{\partial u}{\partial h} \right|_t &= \frac{-1}{\frac{\partial C_h(u)}{\partial u}(t - t_0)} \end{aligned} \quad (\text{B.8})$$

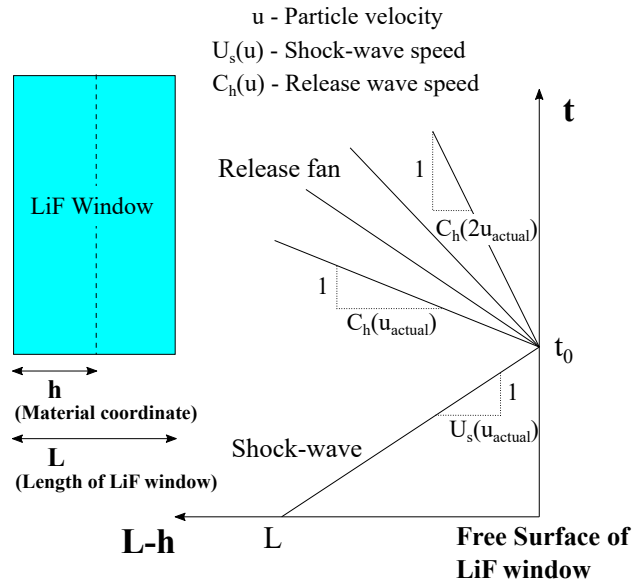


Figure B.3: t-X diagram for release fan.

For conditions of uniaxial strain prevalent in plate-impact experiments, the volumetric strain, $\varepsilon = 1 - \frac{\rho_0}{\rho}$. Further,

$$\begin{aligned}
 d\varepsilon &= \frac{-du}{C_h(u)} \\
 \Rightarrow \frac{\rho_0}{\rho^2} d\rho &= \frac{-du}{C_h(u)} \\
 \Rightarrow \frac{d\rho}{du} &= \frac{-\rho^2}{\rho_0 C_h(u)} \tag{B.9}
 \end{aligned}$$

Thus, Eq. B.7 becomes:

$$\left. \frac{\partial \rho}{\partial h} \right|_t = \frac{\rho^2}{\rho_0 C_h(u) \frac{\partial C_h(u)}{\partial u} (t - t_0)} \tag{B.10}$$

Finally, to evaluate B.4, it remains to evaluate $\left. \frac{\partial \rho}{\partial t} \right|_h = \frac{\partial \rho}{\partial u} \frac{\partial u}{\partial t} \Big|_h$. Next, differentiate the

following equation with respect to t

$$\begin{aligned}
L - h &= C_h(u)(t - t_0) \\
\implies 0 &= \frac{\partial C_h}{\partial u} \frac{\partial u}{\partial t} \Big|_h (t - t_0) + C_h(u) \\
\implies \frac{\partial u}{\partial t} \Big|_h &= \frac{-C_h(u)}{\frac{\partial C_h}{\partial u}(t - t_0)}
\end{aligned} \tag{B.11}$$

Using equations B.9 and B.11,

$$\implies \frac{\partial \rho}{\partial t} \Big|_h = \frac{\rho^2}{\rho_0 \frac{\partial C_h}{\partial u}(t - t_0)} \tag{B.12}$$

Thus using Eqs. B.10, B.6, and B.12, Eq. B.4 can now be written as:

$$\frac{\partial \rho}{\partial t} \Big|_x (h(x, t), t) = \frac{\rho^2}{\rho_0 C_h(u) \frac{\partial C_h(u)}{\partial u}(t - t_0)} \left(-u_{actual} \frac{\rho(h)}{\rho_0} \right) + \frac{\rho^2}{\rho_0 \frac{\partial C_h}{\partial u}(t - t_0)}$$

The integral (I) given in Eq. B.3 becomes

$$\mathbf{I} = \int_{h_a(t)}^{h_b(t)} \frac{\partial \eta}{\partial \rho} \frac{\rho}{\frac{\partial C_h(u)}{\partial u}(t - t_0)} \left(1 - \frac{u_{actual} \rho}{C_h(u) \rho_0} \right) dh$$

Thus, the apparent particle velocity (u_{obs}) given in Eq. B.1 becomes

$$u_{obs} = u_{actual}(\eta - 2\eta_0 + 2) - \mathbf{I}$$

Further, differentiating both sides with u_{actual} and using Leibniz rule for differentiating integrals, we get:

$$\begin{aligned}
\frac{du_{obs}}{du_{actual}} &= (\eta - 2\eta_0 + 2) + \frac{d\eta}{du_{actual}} u_{actual} + \\
&\frac{\partial \eta(h_a(t))}{\partial \rho} \frac{\rho(h_a(t))}{\frac{\partial C_h(u_{actual})}{\partial u}(t - t_0)} \left(1 - \frac{u_{actual} \rho(h_a(t))}{C_h(u_{actual}) \rho_0} \right) \frac{dh_a(t)}{du_{actual}} - \\
&\frac{\partial \eta(h_b(t))}{\partial \rho} \frac{\rho(h_b(t))}{\frac{\partial C_h(2u_{actual})}{\partial u}(t - t_0)} \left(1 - \frac{u_{actual} \rho(h_b(t))}{C_h(2u_{actual}) \rho_0} \right) \frac{dh_b(t)}{du_{actual}}
\end{aligned} \tag{B.13}$$

It can be noted that, similarly to what was stated before Eq. B.8, here $C_h(u_{actual}) = C_h(u_{actual}, u_{actual})$ and $C_h(2u_{actual}) = C_h(u_{actual}, 2u_{actual})$ which, is obtained by setting $u = u_{actual}$ and $u = 2u_{actual}$, respectively.

Equation B.13 can be simplified as described next. The refractive index (η) is given by the linear relation $\eta = A + B\rho$ [2, 3]. For LiF[100] windows used with

1550 nm wavelength light, the material properties $A = 1.2669$ and $B = 0.037$ are taken from [3]. Further, by continuity at start and end of the release fan, $\rho(h_a(t)) = \rho_1$ and $\rho(h_b(t)) = \rho_0$. $\frac{dh_a}{du_{actual}}$ can be evaluated by differentiating $L - h_a(t) = C_h(u_{actual})(t - t_0)$ on both sides w.r.t u_{actual} .

$$\Rightarrow \frac{dh_a}{du_{actual}} = \frac{\partial C_h(u_{actual})}{\partial u} (t - t_0)$$

Similarly,

$$\Rightarrow \frac{dh_b}{du_{actual}} = 2 \frac{\partial C_h(2u_{actual})}{\partial u} (t - t_0)$$

The derivative of refractive index can be expressed as:

$$\frac{d\eta}{du_{actual}} = \frac{d\eta}{d\rho_1} \frac{d\rho_1}{du_{actual}}$$

The density ρ_1 is evaluated using the shock jump conditions and $U_s - u_p$ relation for LiF, $U_s = C_0 + Su_p$, as:

$$\rho_1 = \frac{\rho_0}{\left(1 - \frac{u_{actual}}{C_0 + Su_{actual}}\right)}$$

The material wave speeds $C_h(u_{actual})$ (at peak-strain) and $C_h(2u_{actual})$ (at zero-strain) for LiF are evaluated as follows:

$$\sigma = \rho_0 \left(\frac{C_0}{1 - S\varepsilon} \right)^2 \varepsilon$$

$$C_h(u) = \sqrt{\frac{1}{\rho_0} \frac{d\sigma}{d\varepsilon}}$$

$$\Rightarrow C_h(u_{actual}) = (C_0 + Su_{actual}) \sqrt{1 + \frac{2Su_{actual}}{C_0}}$$

$$\Rightarrow C_h(2u_{actual}) = C_0$$

Thus, Eq. B.13 can now be simplified to :

$$\begin{aligned} \frac{du_{obs}}{du_{actual}} = & (A - 2\eta_0 + 2) + B \left(\frac{\rho_1^2}{\rho_0} u_{actual} \left\{ \frac{C_0}{(C_0 + Su_{actual})^2} + \frac{1}{(C_0 + Su_{actual}) \sqrt{1 + \frac{2Su_{actual}}{C_0}}} \right\} \right. \\ & \left. + 2 \left\{ \rho_0 - \frac{u_{actual} \rho_0}{C_0} \right\} \right) \end{aligned} \quad (\text{B.14})$$

Thus Eq. B.14 can be used to plot u_{obs} as a function of u_{actual} by integration.

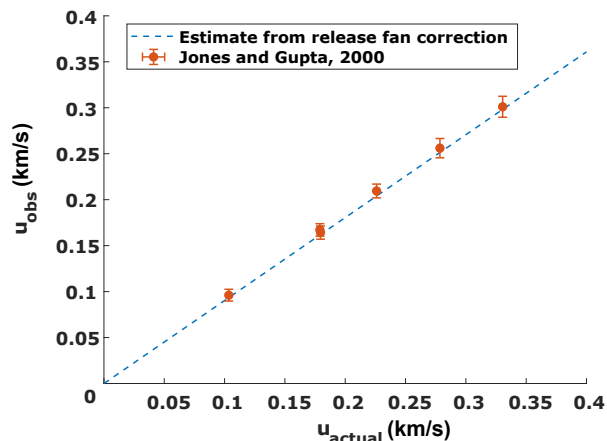


Figure B.4: Comparison of z-cut quartz data from [4] and release fan correction (Eq. B.14) for 532 nm wavelength light.

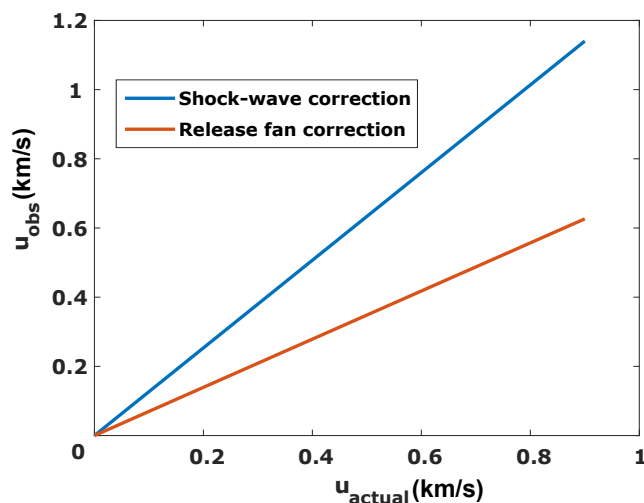


Figure B.5: Observed particle velocity vs. actual particle velocity for shock-waves and release fan in LiF[100] for 1550 nm light.

An experimental validation of Eq. B.14 is performed for z-cut quartz release data provided in [4]. This comparison is provided in Fig. B.4. The parameters for z-cut quartz needed in Eq. B.14 was taken from [3].

The optical corrections due to shock-wave and release fan in LiF[100] window is thus plotted in Fig. B.5.

Corrections due to impedance mismatch between LiF and SLG

As seen in Figure B.6, the particle velocity observed at the SLG-LiF interface, after optical corrections ($u_{\text{interface}}$), is lesser than the particle velocity prevalent in the SLG material ($u_{\text{in-material}}$) before the shock-wave reaches the interface. In order to

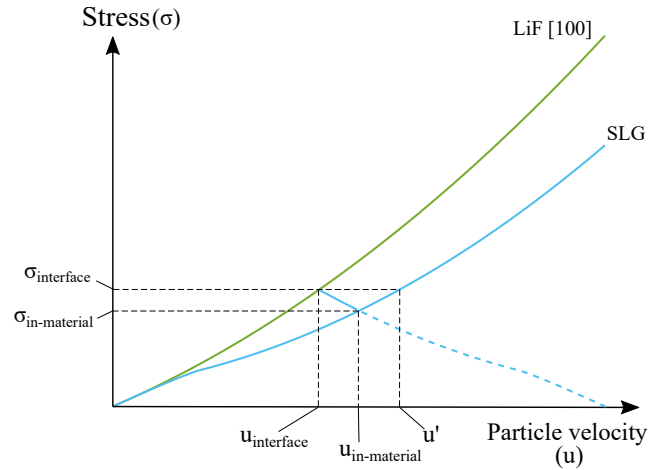


Figure B.6: Stress-particle velocity of LiF and SLG used to obtain the in-material particle velocity in SLG.

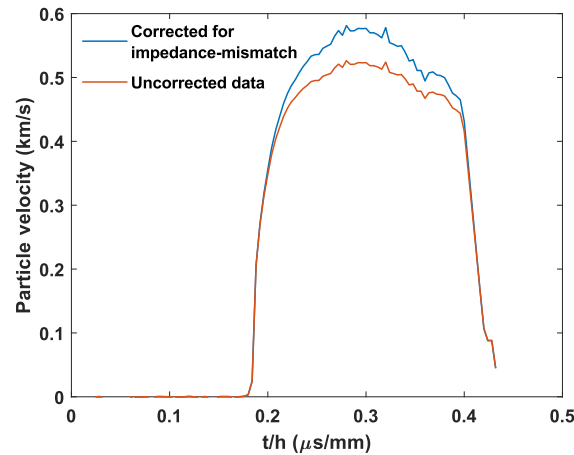


Figure B.7: Impedance mismatch correction for optically corrected data from Expt. SSL-2 of this work.

construct a stress-strain loading history of the SLG material, the observed velocity profile ($u_{interface}(t)$) is converted to in-material velocities ($u_{in-material}(t)$) using the following formula:

$$u_{in-material}(t) = \frac{u_{interface}(t) + u'}{2} \quad (\text{B.15})$$

where u' is shown in Fig. B.6. The $U_s - u_p$ parameters taken from [5] were used to construct LiF [100] stress Hugoniot. The SLG hugoniot was constructed using parameters taken from [6]. An example of impedance mismatch correction is provided in Fig. B.7, for data from Experiment 2 in the main work. The blue curve shown in Fig. B.7, is the in-material particle velocity of SLG.

References

- ¹D. R. Hardesty, “On the index of refraction of shock-compressed liquid nitromethane”, *Journal of Applied Physics* **47**, Publisher: American Institute of Physics, 1994–1998 (1976).
- ²D. Hayes, “Unsteady compression waves in interferometer windows,” *Journal of Applied Physics* **89**, Publisher: American Institute of Physics, 6484–6486 (2001).
- ³B. J. Jensen, D. B. Holtkamp, P. A. Rigg, and D. H. Dolan, “Accuracy limits and window corrections for photon Doppler velocimetry,” *Journal of Applied Physics* **101**, Publisher: American Institute of Physics, 013523 (2007).
- ⁴S. C. Jones and Y. M. Gupta, “Refractive index and elastic properties of z-cut quartz shocked to 60 kbar,” *Journal of Applied Physics* **88**, Publisher: American Institute of Physics AIP, 5671 (2000).
- ⁵T. Oniyama, “Shock Compression of Molybdenum Single Crystals to High Stresses,” Ph.D. thesis (California Institute of Technology, 2020).
- ⁶C. S. Alexander, L. C. Chhabildas, and D. W. Templeton, “The Hugoniot elastic limit of soda-lime glass,” *AIP Conference Proceedings* **955**, Publisher: American Institute of Physics, 733–738 (2007).